**Université de Caen Basse-Normandie**

*École* doctorale SIMEM

**Thése de doctorat**

Présentée et soutenue le : 26/11/2014

par

***Pravarthana Dhanapal***

pour obtenir le

**Doctorat de l'Université de Caen Basse-Normandie**

**Spécialité : Chimie des Matériaux**

---

# High-Throughput Synthesis of Functional Oxide Films

---

Directeur de thése : Wilfrid Prellier

**Composition du jury :**

| | |
|---|---|
| R.Desfeux | Professeur, Université d' Artois, Lens(**Rapporteur**) |
| Ph.Lecoeur | Professeur, Université d' Orsay, Paris(**Rapporteur**) |
| R.Cloots | Professeur, Université de Liége, Sart-Tilman, Belgique (**Examinateur**) |
| B.Vertryen | Professeur, Université de Liége, Sart-Tilman, Belgique (**Examinateur**) |
| D.Chateigner | Professeur, CRISMAT, CNRS, Caen (**Examinateur**) |
| W.Prellier | Directeur de Recherches, CRISMAT, CNRS, Caen(**Directeur de thése**) |

*Dedicated to my parents,*
*teachers and friends.*

# Acknowledgements

Firstly, I thank Antoine Maignan, Research Director at CNRS and Director of the CRISMAT Laboratory for hosting me. I would like to express thanks to the IDS-FUNMAT network for their continuous financial support through Erasmus Mundus scholarship. I would like to express my special appreciation and deep sense of gratitude to my supervisor Dr Wilfrid Prellier, you have been a incredible mentor to me. I am always indebted for your scientific advice, trust, continuous support, and co-operation during the course of this work. I would also like to thank my co-supervisors Dr.Rudi Cloots and Dr.Bénédicte Vertruyen ULG, Belgium for their valuable suggestions for my thesis and arranging good facilities in University de Liege. I acknowledge Dr. Oleg Lebedev, Dr Daniel Chateigner, Dr.Sylvie Hebert and Dr Eric Hug for some of the experimental measurements. I also thank Prof R. Ramesh, M. Trassin University of Berkeley, USA and P.A. Salvador Carnegie Mellon University, Pittsburg, USA for the collaborative works. I also thank Dr. R. de Kloe EDAX, Netherland for his help in indexing EBSD patterns.

I grateful to all the technicians and engineers in CRISMAT and CNRT laboratory for their help and support during the experiments. Especially, I would like to thank Mr.Jerome Lecourt, Mr. Francois-Xavier Lefevre and Mr. F.Veillon for their immense help. I also extend my thanks to some of the present and past colleagues in the lab, Dr A. David, Dr. B. Mercey, Dr. U. Luders, Dr, Dr H. Rotella., Dr. K. Kolincio, Dr.Q. Li, Dr. P. Walke, Dr. K. Singh, Dr. S. Bhame Dr. Motin S., Dr. Nunna R., Dr. G. Venkatesh, Dr. Gnanavel M., Dr. Pratibhanalini S., Mr. Myana S.M., Mrs M. Lacotte and Mrs A. Dellicour, who have been wonderfully supportive through their individual help and pleasant company. I also thank colleagues from GREENMAT, ULG, Dr. C. Henrist, Dr. P. Colson, Mr. Giles P. and Mr F. Stevens.

My special thanks to Dr. Suresh Perumal for his constructive criticism and valuable suggestions during my thesis writing.

I wish to acknowledge all my teachers from primary schools to master's level who educated and nurtured me academically to reach at this destiny. Especially, I thank my master thesis supervisors Prof Satish Ogale, NCL Pune, and Dr Seema Verma, IISER Pune for their indebted scientific advice.

I would like to thank my friends in India and Europe who have been very supportive

and encouraging.

I take this opportunity to thank my beloved family members for their support, dedication and love. It gives me a great pleasure to acknowledge all those people whose help, wishes, encouragement and support have brought this task to its completion.

# Contents

# General Introduction

Materials have played a vital role in shaping the human civilization and their evolution. Archaeologists have proved that our ancestors used materials from stone age to bronze age and subsequently iron age to meet their basic needs such as shelter, food, navigation and weapons etc [1]. In the current 21st century, the advancement in materials science was driven by cutting-edge research made by scientists across the globe, shaping the relevant technology for human welfare. In this regard, smarter materials with multifunctional properties at the nanoscale are required for novel electronic technology. Such smart materials should address the need for device miniaturization, lower power consumption, cheaper price and long device life etc. In this endeavour for smart electronic technology, metal oxides with varied physical and chemical properties can be a rich field of research.

Indeed, metal oxides, particularly when containing transition and/or lanthanide metal ions-, exhibit exciting physical phenomena such as ferroelectricity, high-$T_C$ superconductivity or multifunctional properties such as multiferroicity [2, 3]. These physical phenomena arise due to unique arrangements of spins, orbitals and charges in the structural lattice. Moreover, while fine tuning the structural arrangements in metal oxides by means of quantum confinement, defect and strain engineering, they could effectively be used for technological applications [4]. In order to achieve such control, it is usually necessary to obtain the material in the form of an epitaxial film, where the properties can be tuned by adjusting the interactions between substrate and film.

In this regard, fabricating epitaxial films could help to develop new functionalities for advanced technologies. such as :

(a) Ultra-high density information storage [5].

(b) Low-power memory devices based on the magnetoelectric effect to switch magnetization by electric field [6].

(c) Oxide based field-effect transistors with gate-voltage-modulated transition at room temperature [7].

Moreover, epitaxial metal oxides can merge directly into devices without any further integration or modification. Therefore, the research on epitaxy of metal oxides is of great interest, as the epitaxy provides a robust way to obtain desired and novel properties for applications, and can further be used to control the structure using strain-engineering [8].

Strain engineering leads in fact to changes in bond-lengths and bond-angles of the film material with respect to the bulk material, due to the difference in lattice parameters between the film and the substrate. Also, these strain-related structural changes alter the band structure, and can often lead to novel properties. Moreover, at the interface or in an heterostructure, novel properties can emerge such as ferroelectricity, magnetism, superconductivity, magneto-electric coupling, 2-Dimensional Electron Gas(2DEG) and Quantum Hall effect etc [9]. One of such example is the interface made of an insulating $LaAlO_3$ film and the Ti-terminated surface of $SrTiO_3$ substrate [10–13]. There are also other examples of exotic strain engineered interfaces such as :

(a) The interface between $La_{0.6}Sr_{0.4}MnO_3$ with nonmagnetic insulating layers to obtain robust ferromagnetism for spin-tunnel junctions [14].

(b) The interface control of bulk polarization of $BiFeO_3$ [15].

(c) The high-temperature interface superconductivity between metallic $La_{1.55}Sr_{0.45}CuO_4$ and insulating $La_2CuO_4$ [16].

Regarding superlattice structures, one can cite :

(a) The unconventional band engineering in superlattices of $LaMnO_3/SrMnO_3$ [17].

(b) The metal-insulator transition in superlattices of $LaAlO_3/LaNiO_3$ [18, 19].

(c) The giant themoelectric Seebeck coefficient of 2DEG in superlattices of $SrTiO_3/SrTi_{0.8}Nb_{0.2}O_3$ [20].

Other examples showing novel properties in thin films through strain engineering [21] are :

(a) Enhanced ferroelectricity in $BaTiO_3$ thin films [22].

(b) The room-temperature ferroelectricity in $SrTiO_3$ thin films [23].

(c) The induced-ferromagnetic in antiferromagnetic $LuMnO_3$ epitaxial films [24].

In addition, the strain engineering opens the possibility of creating metastable phases

in thin film form, whose properties are different from the bulk phase [8].

From a practical point of view, epitaxial layers are usually grown on single-crystals with a similar structure and a small mismatch. $SrTiO_3$ (cubic $a$=3.905 Å ) is probably one of the most frequently used substrate materials for the perovskite films, but to achieve a compressively strained film, other substrate like $LaAlO_3$ (pseudocubic, $a$=3.78 Å ) can also be used. However, earlier research's have been restricted because of the limited range of compositions and low-index of commercially available single crystal substrates [25]. Also, unusual composition and/or high-index ($hkl$) single crystal substrates are either very costly or unavailable. Thus, novel epitaxy synthetic methods need to be developed in order to go beyond this limitation on availability of single crystal substrates in terms of phase, composition, size, orientation and symmetry.

Such approach is a high-throughput synthesis process called combinatorial substrate epitaxy(CSE), as proposed by the group of G.S. Rohrer and Paul salvador(Carnegie Mellon University,USA), where a metal oxide film is grown epitaxially on a polycrystalline substrate [26–30]. CSE relies on polycrystalline substrates in which each grain can be viewed as a single crystal substrate with a specific crystallographic orientation. A multitude of different orientations of the metal oxide film can be obtained in a single deposition over the polycrystalline substrate. Thanks to the integration of high-resolution structural analysis at the grain scale, this approach generates a whole library of film data as a function of the orientation of substrate grain in a single experiment. Furthermore, the dependence on commercial availability of substrates is no longer an issue since -the synthesis of polycrystalline substrates with some tunability of the grain size becomes possible.

The motivation of the present thesis is precisely to apply and develop this combinatorial substrate epitaxy approach in several areas, as reported in the next five chapters. The present thesis is divided as follows :

Chapter 1- describes the experimental techniques used for the synthesis of the polycrystalline substrates, the growth of epitaxial films, the structural and physical characterization. More specifically, it provides an overview of the principles of conventional and spark plasma sintering (used for the densification of the polycrystalline substrate), pulsed laser deposition technique (used for epitaxial thin film growth), electron backscattering diffraction (used for the local structural characterization of the substrate surface and film),

X-ray diffraction, transmission electron microscopy and a few physical properties.

In Chapter 2, the combinatorial substrate epitaxy approach is applied to the case of $Ca_3Co_4O_9$ films grown on polycrystalline textured alumina. This chapter reports about the Spark Plasma Sintering(SPS) and polishing of the alumina substrates, their characterization by a combination of Electron Back Scattering Diffraction (EBSD) and X-ray diffraction (XRD). The growth of nanostructured epitaxial $Ca_3Co_4O_9$ thermoelectric films by Pulsed Laser Deposition (PLD) technique is then described and the results of Transmission Electron Microscopy (TEM) and EBSD are presented. The investigation of the epitaxial relationship between the substrate grains and the film is also presented. The chapter ends with the characterization of the thermoelectric power factor obtained by the measurement of electrical resistivity and Seebeck coefficient.

Chapter 3- demonstrates that combinatorial substrate epitaxy can be applied to heterostructures. The growth of multiferroic $BiFeO_3/La_{0.7}Sr_{0.3}MnO_3$ heterostructured thin films on $LaAlO_3$ polycrystalline substrates is indeed presented. Also, an EBSD study of both the polycrystalline LAO substrate and the BFO top layer is described. The last part of the chapter reports the local characterization of the ferroelectric BFO layer by piezoforce microscopy.

In Chapter 4, the combinatorial substrate epitaxy approach is finally applied to the synthesis of metastable monoclinic $Dy_2Ti_2O_7$ thin films grown on $La_2Ti_2O_7$ substrate. After a description of the preparation of the polycrystalline substrate and the growth of the film, the second part of the chapter is devoted to the analysis of the structural and EBSD data that demonstrates. The monoclinic form of $Dy_2Ti_2O_7$ is obtained instead of the cubic structure usually observed in the bulk material.

Chapter 5 presents the conclusions of the thesis and discusses opportunities for further work in the promising area of this combinatorial substrate epitaxy.

# Chapter 1

# Synthesis and Characterization techniques of epitaxial films

## 1.1 Introduction

In this chapter, we briefly describe the synthesis and characterization techniques used in the current thesis work. The objective of this work is to obtain functional films by combinatorial substrate epitaxy (CSE) and the epitaxial relationship of the film with respect to the polycrystalline substrate. The first two sections of this chapter provide an overview of the Spark Plasma Sintering (SPS) used to prepare polycrystalline substrates and the Pulsed Laser Deposition (PLD) utilized to grow the thin films. Electron Backscatter Diffraction (EBSD) is then described in some detail since it is a crucial tool for the characterization of the local crystallographic orientation of the substrates and films. The structural characterization also relies on X-ray Diffraction (XRD) and High Resolution Transmission Microscopy (HRTEM) is presented. The last sections describe briefly the techniques used to characterize the specific physical properties of the films, i.e. thermoelectricity (by measurement of electrical resistance and Seebeck coeficient) and ferroelectricity (by Piezoelectric Force Microscopy).

## 1.2 Synthesis of dense polycrystalline substrates

In the case of multicationic oxides, the fabrication of substrates first requires the preparation of a pure phase powder either by solution-based methods or through standard solid state route. The present work requires large quantities of powder and large grain sizes. Solid state route appears thusly the appropriate choice. In this method, stoichiometric of individual metal oxides are ball-milled and calcined at high temperature to obtain the required phase (see Figure 1.1).

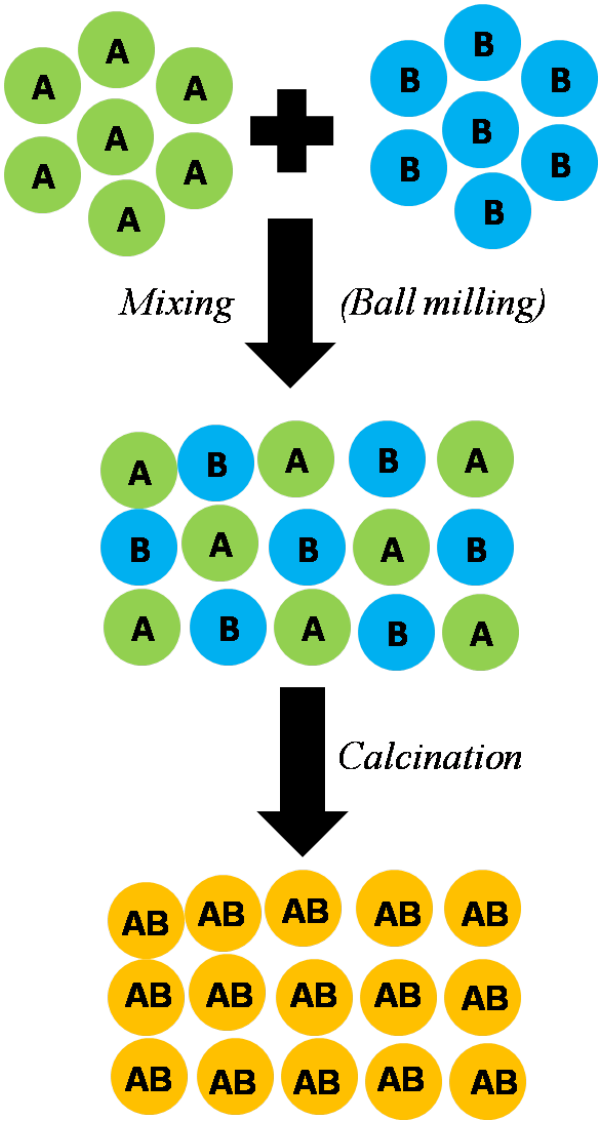


Figure 1.1: Schematic diagram for solid state route used to obtain pure phase (AB) from the mixed powders A and B precursors

Then, the powder needs to be sintered into a dense polycrystalline pellet. The ceramic

pellets used for CSE should be highly dense to be easily handled during polishing. To obtain dense ceramics for the current work the available options are conventional sintering and Spark Plasma Sintering. In conventional sintering, the powder is mixed with a binder uniaxially pressed into a pellet to further increase the density of the unfired pellet. It can be pressed a second time using cold isotactic pressing (see Figure 1.2).

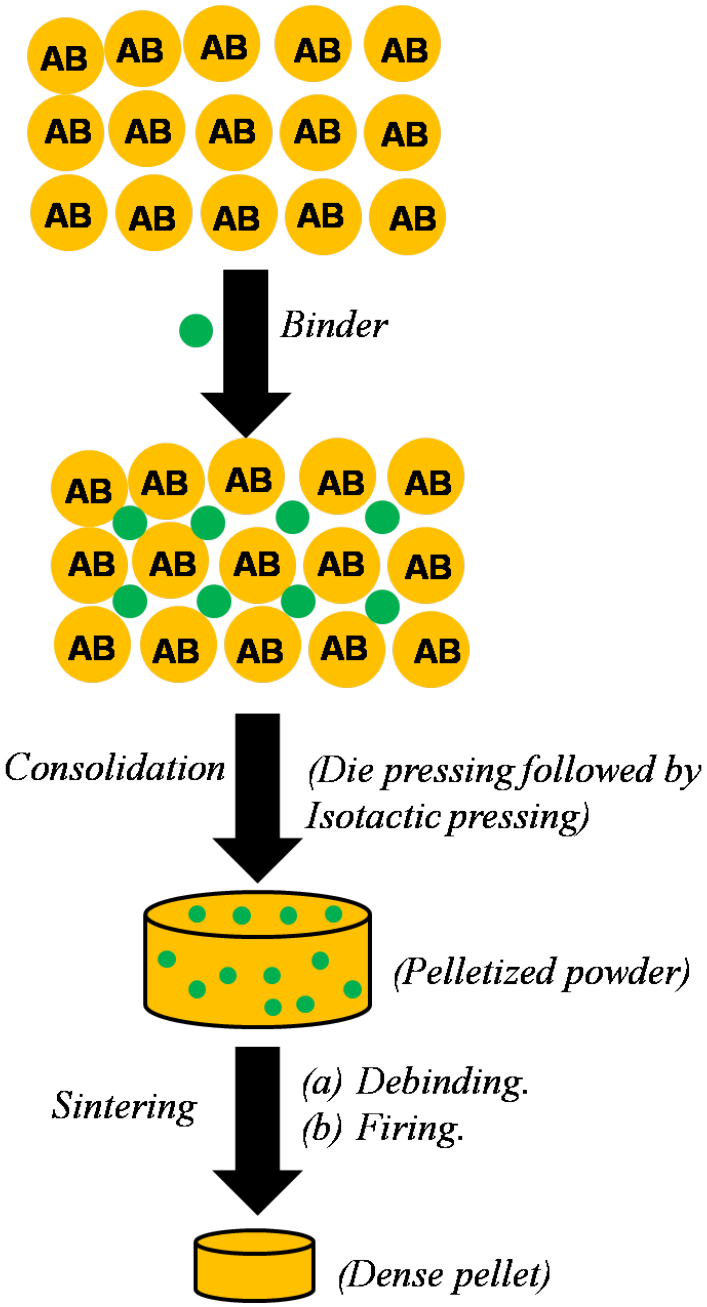


Figure 1.2: Schematic of conventional sintering used to obtain a dense pellet from pure phase(AB) powder.

This pellet is finally fired at optimal conditions (see Figure 1.3). Unfortunately, the ceramic obtained by this method might be unsuitable if the density of the sintered pellet is not high enough for handling, cutting and polishing. In that case, an alternative technique is Spark plasma sintering(SPS). Literature indeed demonstrates that SPS can be used to densify most of the materials. SPS is a pressure-assisted pulsed current sintering, in which densification is favoured over coarsening (see Figure 1.4) and occurs at lower temperatures than in the conventional process.

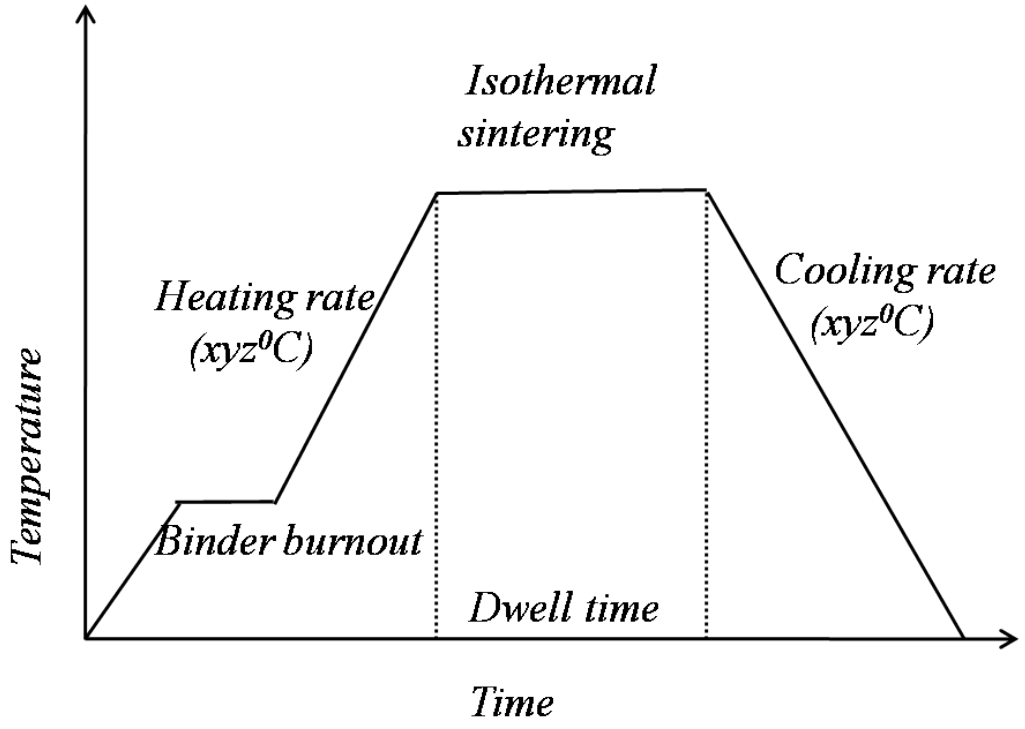


Figure 1.3: Schematic of a general heating schedule for conventional sintering.

The SPS process usually combines very efficient densification with a fine control of grain structure. The applied pressure may induce texture in the case of anisotropic grain shape in to-be-densified powder [31, 32]. In the SPS experiments (see Figure 1.5), the metal oxide powders are loaded into a graphite die lined with graphite paper to prevent contamination of the die.

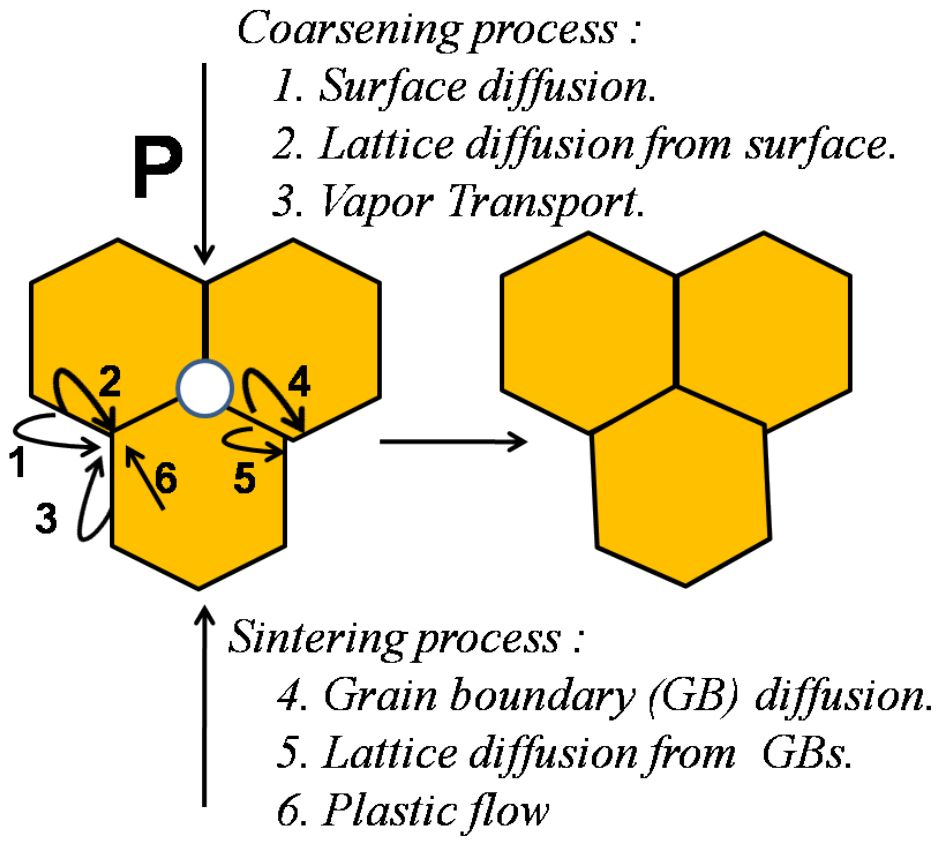


Figure 1.4: Six distinct mechanisms can contribute to the sintering of a consolidated mass of crystalline particles : (1) surface diffusion, (2) lattice diffusion from the surface,(3) vapor transport, (4) grain boundary diffusion, (5) lattice diffusion from the grain boundary, and (6) plastic flow. Only mechanisms 4 to 6 lead to densification [33]. Application of pressure in SPS lowers the porosity and enhance the densification rate.

The loaded die is inserted into the SPS apparatus (Struers Tegra Force-5). The required sintering cycle is software-controlled. A high current with a low voltage passes through the sample, causing the heating. This heating arises due to dielectric loss, eddy current heating and Joule heating in the sample. The current density tends to pass through the sample and graphite die for conducting and non-conducting samples, respectively. Pyrometric temperature sensors are connected to an electric controller to adjust the current by feedback signal. The temperature control is ensured by the top pyrometer for conducting samples and by the front pyrometer for non-conducting samples. The apparatus can be kept in vacuum or in particular gas environment.

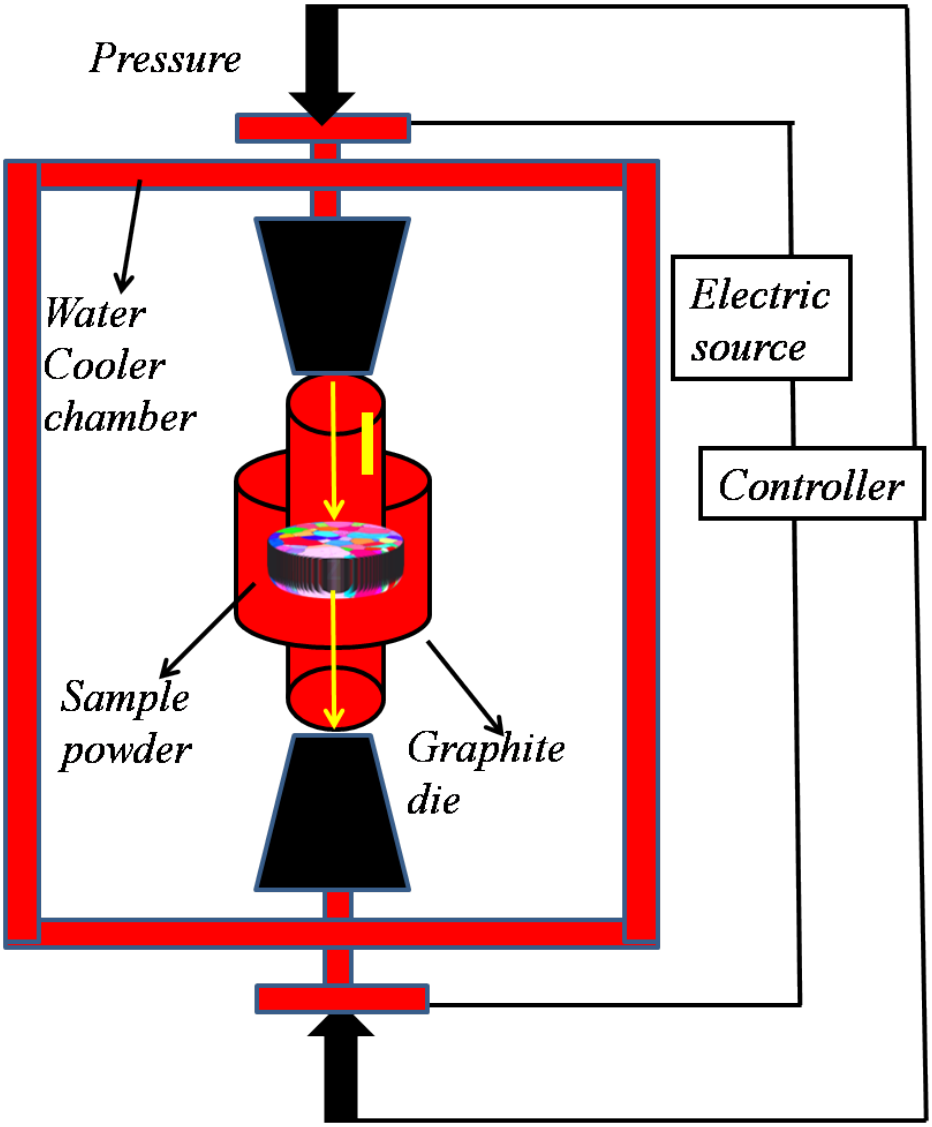


Figure 1.5: Schematic diagram of a Spark Plasma Sintering equipment.

### 1.2.1 From sintered pellet to polished substrate

The dense pellets cannot be used as substrates for thin film grow without polishing in order to obtain a surface with low roughness. The procedure is depicted Figure 1.6. After standard polishing with silicon carbide papers, and diamond liquid pastes, the mechanically stressed surface layer is removed by polishing with a solution of colloidal silica followed by etching or thermal quenching [34].

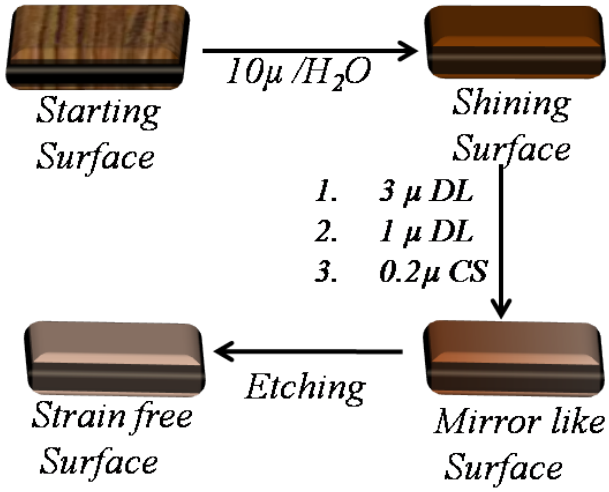


Figure 1.6: Illustration of the polishing procedure (DL = diamond liquid paste ; CS = colloidal silica)

## 1.3 Pulsed Laser Deposition

In the current work, Pulsed Laser Deposition (PLD) is used to grow films on the polished and etched surface of polycrystalline pellets. PLD is a versatile technique to obtain high quality epitaxy of complex oxides, with a good control of the stoichiometry, in for example both heterostructures and super-lattices. Figure 1.7 shows a schematic of typical PLD system. A vacuum pump connected to the chamber is used to pump the chamber down to a base pressure of $10^{-8}$ mbar. The working gas (e.g., oxygen) is then inserted through the gas inlet and the pressure of the chamber is adjusted to the desired value for deposition(typically $10^{-2}$ mbar). A laser beam is focused on a ceramic target to create a plasma that will condense on a substrate that can be heated to a maximum temperature of about 750 °C . The target-to-substrate distance can be adjusted in order to control the incidence of the plasma on the substrate. The mechanism in PLD involves several stages. The absorption of the incident laser by the target material creates electronic excitation which subsequently dissociates and evaporates the target material from the surface. The evaporated material comprise atoms, molecules, electrons, ions and clusters, leading to the formation of the so-called "plasma plume" [35].

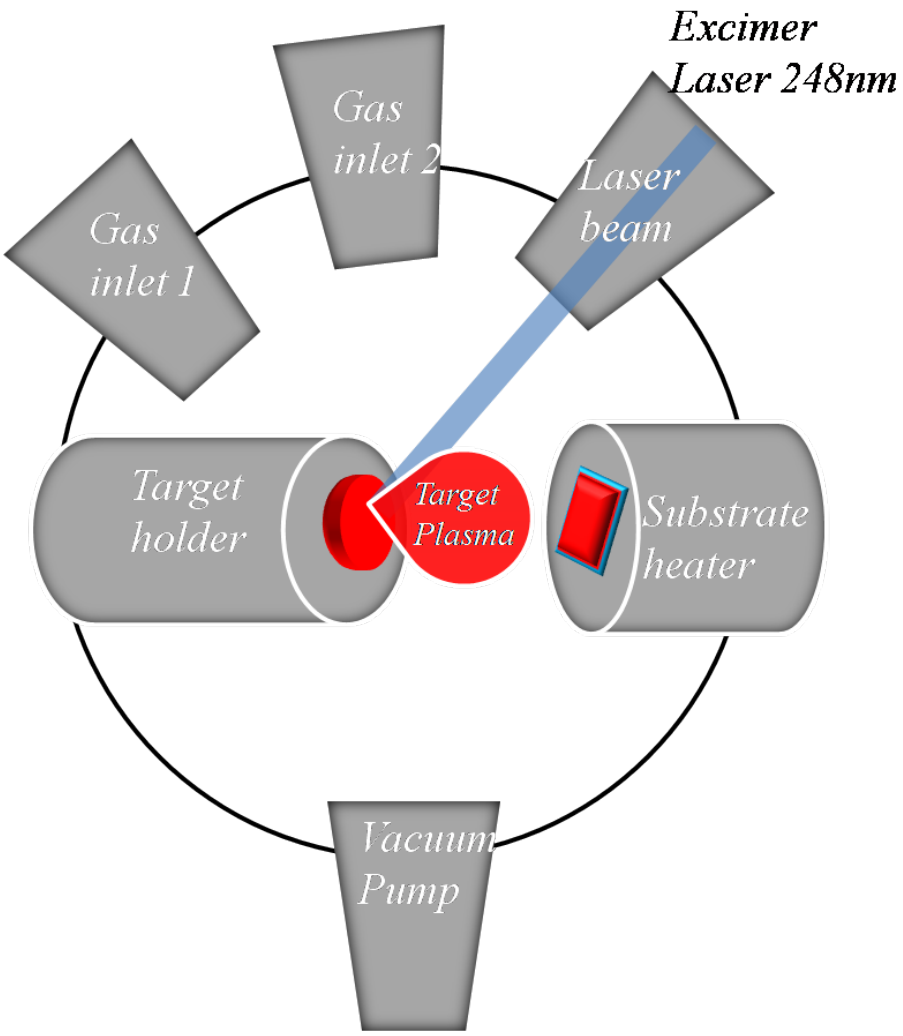


Figure 1.7: Typical schematic diagram of PLD.

The plume is oriented perpendicular to the target surface as a result of recoil by coloumbic repulsion. Condensation of the plume species over the substrate positioned opposite to the target leads to film nucleation and growth. Experimental parameters such as ambient gas pressure, laser energy and frequency influence the plasma plume and the deposition rate. The substrate temperature influences the film nucleation and growth mode. More generally, the experimental parameters control the stoichiometry of the metal oxide, the crystallinity and the uniformity of the resulting epitaxial film.

## 1.4 Scanning Electron Microscopy

Scanning Electron Microscopy (FEG-SEM Carl ZEISS SUPRA 55) is used to characterize the morphology of powders and polycrystalline samples. The incident electron beam obtained from FEG undergoes elastic and inelastic scattering in the sample. This produces secondary electrons, backscattering electrons, Auger electrons, X-rays, and cathodoluminescence [36]. To capture the SEM image, the secondary electrons and backscattering electrons can be detected for topography and phase informations, respectively. The accelerating beam voltage (1 to 30 kV), aperture size (60-120 $\mu$m), working distance (5 to 20 mm), and magnification were chosen in order to properly focus the beam and minimize charging effects in the sample. This ensures clear and resolved images. Moreover, X-ray signals can be detected using Energy Dispersive X-ray analysis to determine composition of the samples.

## 1.5 Electron Back Scatter Diffraction

The combinatorial substrate epitaxy approach requires the characterization of the crystallographic orientation of the individual crystallites in the substrates and in the films grown upon these substrates. This is achieved by Electron Back Scatter Diffraction(EBSD), a technique that relies on the collection of the signal diffracted by thick specimens in a SEM(FEG-SEM Carl ZEISS SUPRA 55). EBSD allows the investigation of the surface before and after the epitaxial growth, in order to understand the epitaxial relationships. Generation of EBSD patterns can be viewed as two stage process. In the first stage, the incident electrons are scattered elastically or inelastically while entering into the sample. This scattering process determines the interaction volume [37]. Secondly, electrons with the appropriate incidence angles interact elastically with the crystal lattice planes of the crystallites. This produces two widely opened kossel diffraction cones from the top and bottom of the lattice planes. The intersection of these diffracting cones with the phosphor screen is detected as a pair of lines in the gnomonic projection (display all great circles as straight lines). The observed bands of diffraction lines are called Kikuchi patterns.

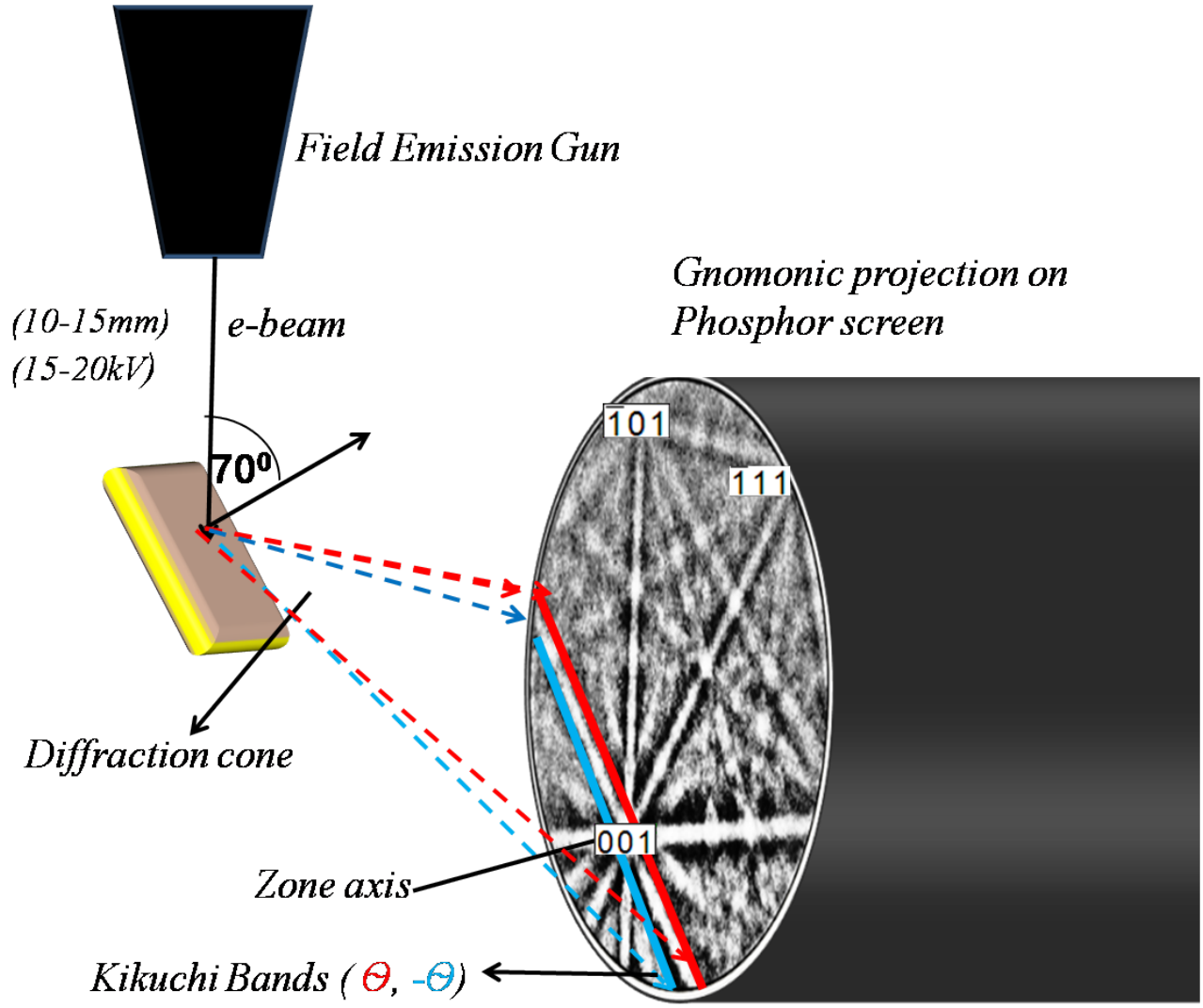


Figure 1.8: Schematic representation of the EBSD experimental set-up. The sample is mounted on a support tilted at 70° with respect to the primary beam, to ensure a maximal emission of backscattered electrons [38].

In EBSD experiments (see Figure 1.8), the aim is to capture sharp kikuchi patterns. For this, several parameters need to be adjusted such as the sample working distance, the background subtraction and the camera settings. In automated EBSD, the kikuchi bands in the collected patterns are then detected by an automatic procedure based on the Hough transform algorithm in order to locate the band positions and band widths (see Figure 1.9). Then, the interplanar spacing, interplanar and interzonal angles based on geometrical analysis of kikuchi patterns are computed (see Figure 1.10) [40].

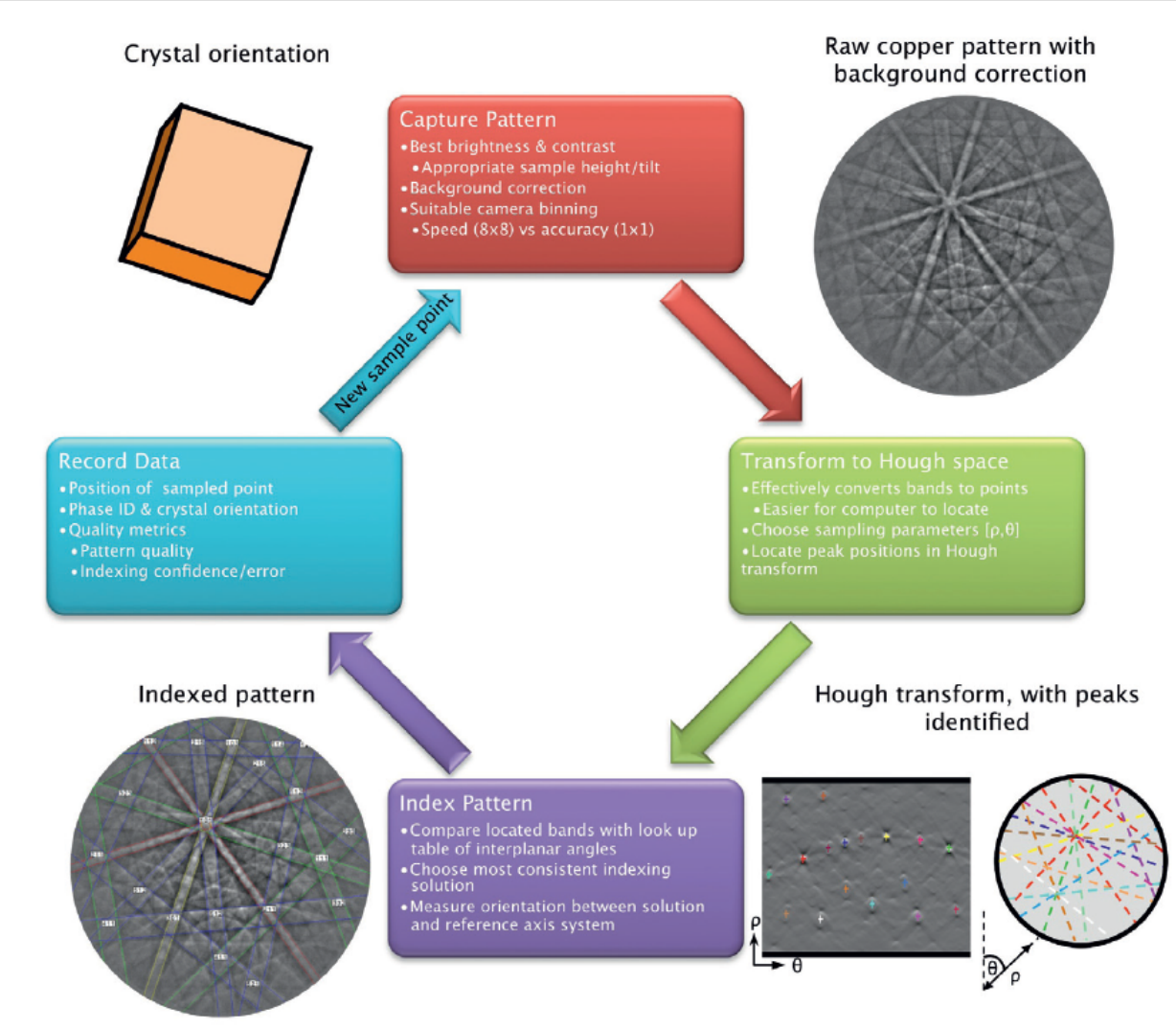


Figure 1.9: Schematic model of EBSD indexing procedure starting from capturing pattern to determination of crystal orientation [39].

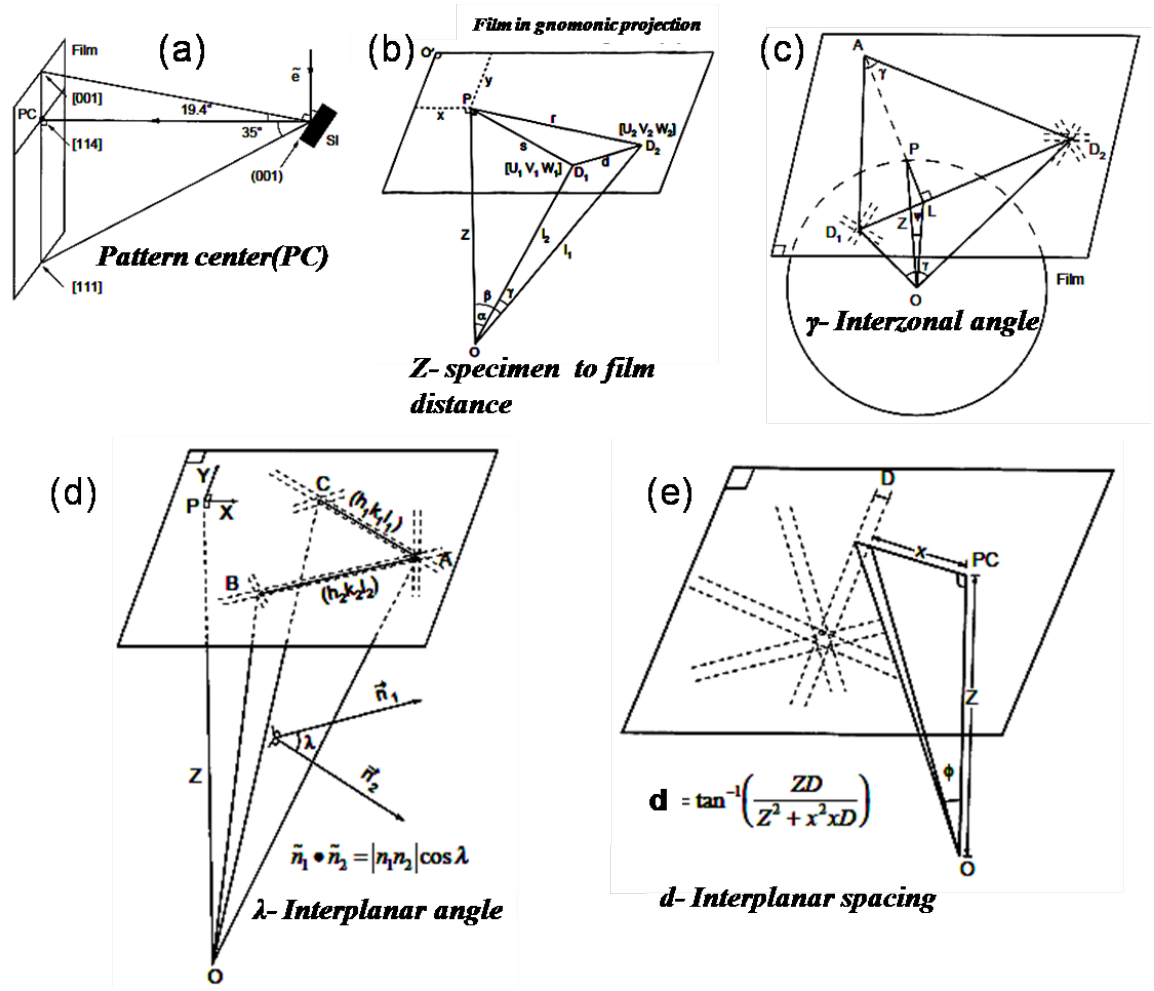


Figure 1.10: Typical geometrical analysis of kikuchi pattern that requires to measure the lattice parameters are (a) pattern Center ( the point of intersection in phosphor film detector that is normal to the electron source point), (b) specimen to film distance, (c) interzonal angle, (d) interplanar angle and (e) interplanar spacing [40].

This experimentally computed values are compared with values simulated from known structural data ( i.e. the optimized (hkl) reflector list based on the lattice parameters and the (hkl) indices of the strongest diffracting planes). The indexing software then determines the possible crystal orientations for each possible combination of three bands (triplet). The solutions are then ranked according to a voting table in order to select the solution(s) that allow(s) to index a maximum number of triplets. The Confidence Index (CI) is based on the difference between the best and the second best indexing solution in the voting algorithm. The voting algorithm is given as $V_1$-$V_2/V_{ideal}$, where $V_1$ and $V_2$ are the number of votes for first and second solutions, and $V_{ideal}$ is the total possible number

of votes from the detected bands. The value of CI=0 means that there are two or more equivalent solutions that the software cannot distinguish, while a CI of 1 indicates that there is no other solution found [41]. The quality of indexing can be further characterized by the fit parameters that describes the misfit between the calculated solution and the bands detected in the Hough transform ; it typically varies from 0.2° to 0.8° for good patterns and can reach up to 2° for poor patterns even though they can be correctly indexed (see Figure 1.11).

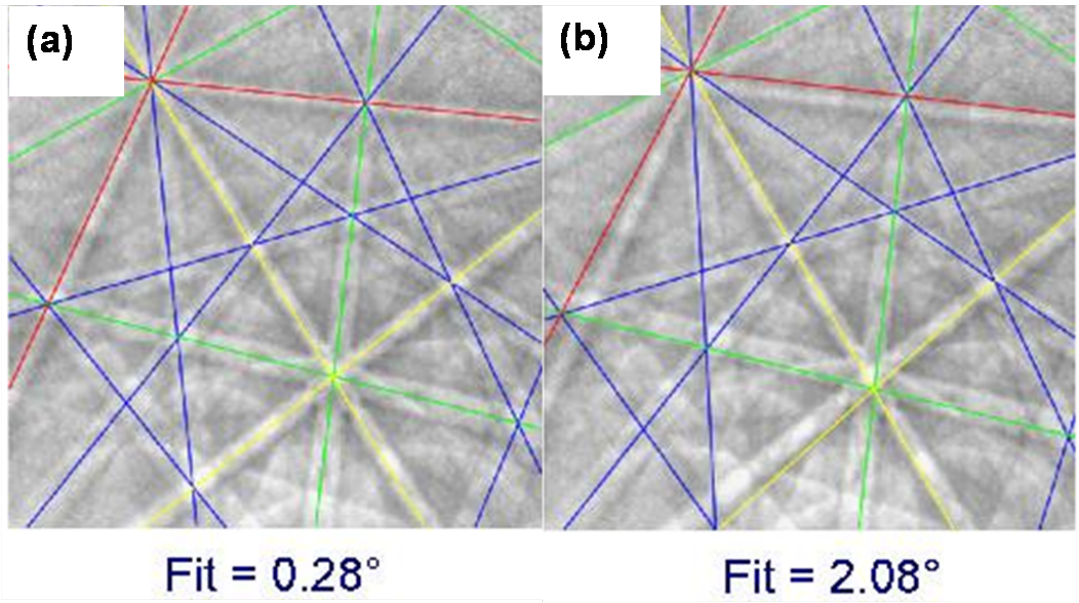


Figure 1.11: Shows a typical kikuchi patterns indexed with (a) good and (b) poor fit values [41].

The indexation of the EBSD pattern of a crystallite enables the calculation of the orientation of the a,b,c crystallite directions with respect to three reference axes fixed to the sample.

The qualitative picture for visualizing the microstructure can be obtained using EBSD. Also, the quantitative distribution of grain size, misorientation angle and orientation can be given. EBSD measurements on a regular array of points at the surface of the sample can be visualized as a color-coded map, where the color code is based on an inverse pole figure (IPF) (see Figure 1.12(a)). The color coded IPF map illustrates the crystallite directions that are parallel to a given viewing direction. It is not really an orientation map since the crystallite axes perpendicular to the displayed directions may freely rotate without

giving change in the IPF map. Real color-coded orientation map in Euler representation is obtained (see Figure 1.13).

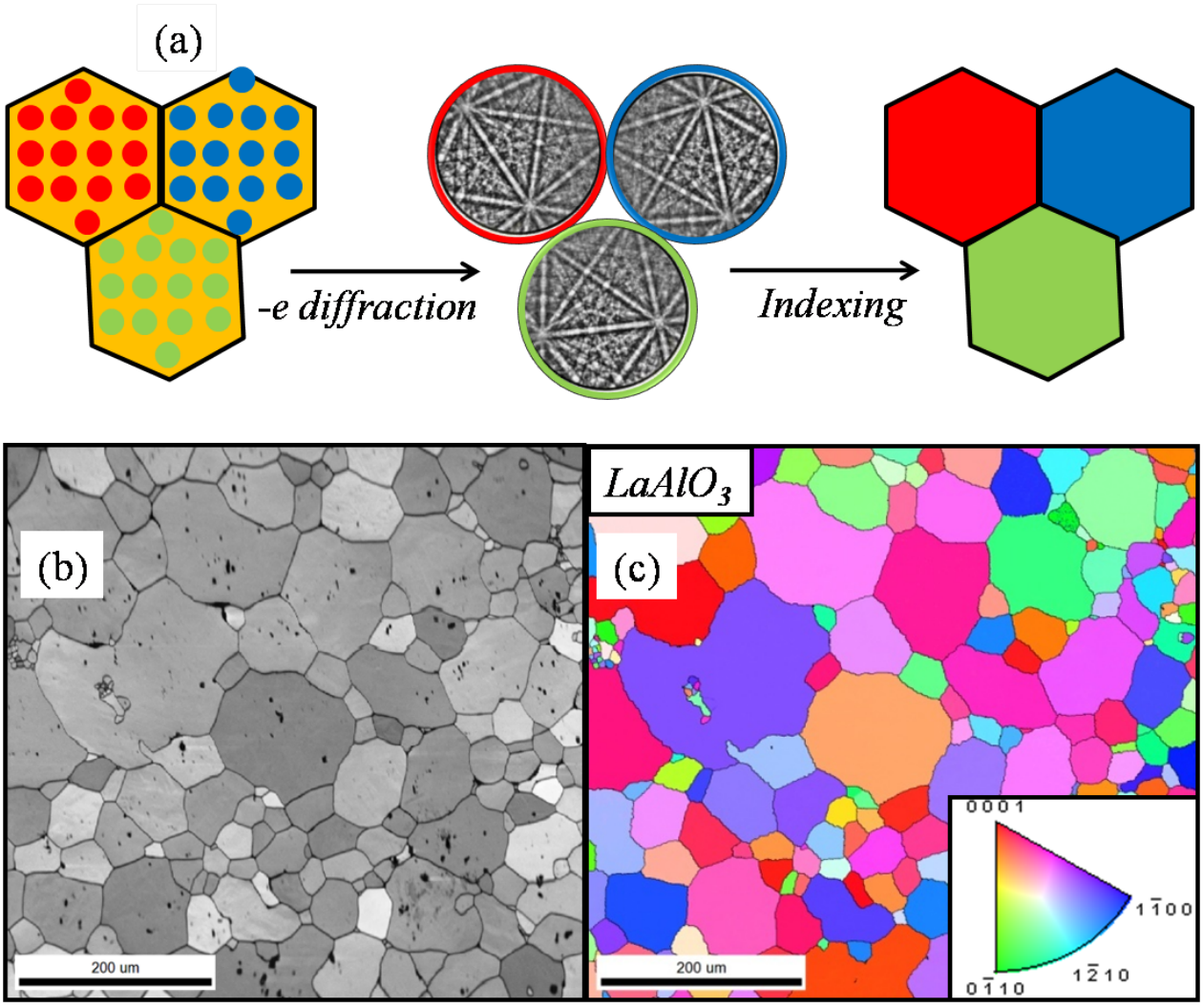


Figure 1.12: (a) Illustrating the visualization aspect of orientations in automated EBSD scan is shown, (b) Image quality map coded in gray scale and (c) Color-coded Inverse pole figure map.

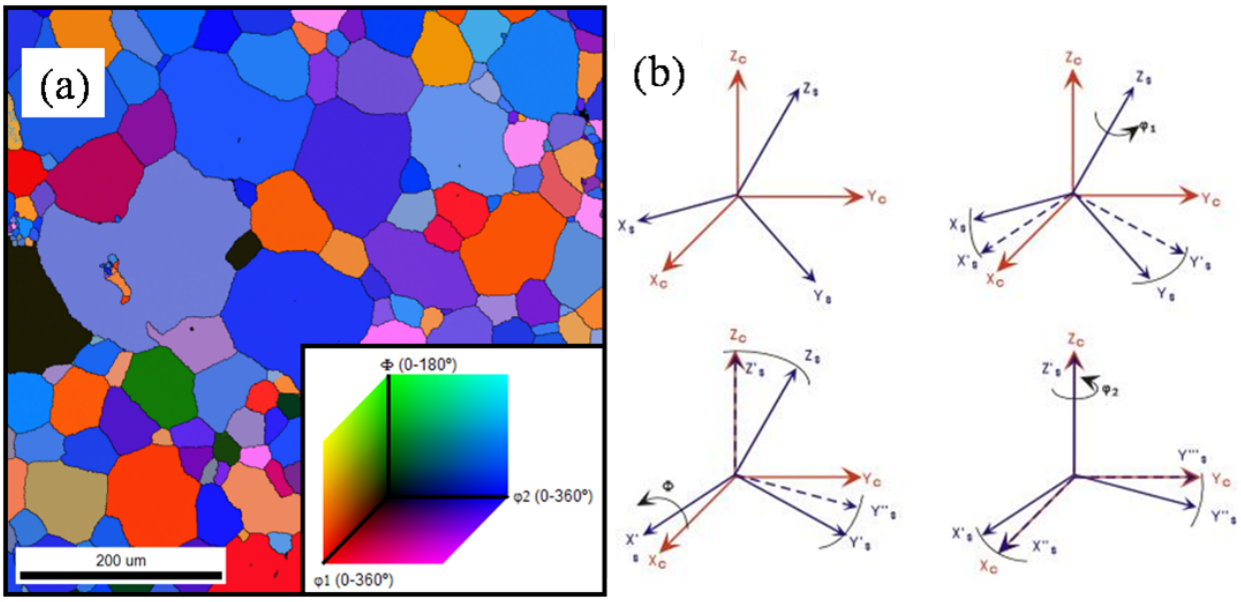


Figure 1.13: (a) color coded orientation representation in standard Euler angles $(\varphi_1, \phi, \varphi_2)$ in Bunge's form. and (b) Schematic representation of Euler angles $(\varphi_1, \phi, \varphi_2)$ in Bunge's form. They are the three rotations about the principle axes of the sample to bring the sample axes into coincidence with the principle axes of the crystal : first the rotation $(\varphi_1)$ about the Zs axis followed by a rotation $(\phi)$ about the Xs axis followed by a third rotation $(\varphi_2)$ about the Ys axis again.

In addition to these maps, which show the differences in orientation between neighbouring grains, the texture of the sample can also be plotted as pole figures or inverse pole figures. This implementation is based on a discretization of Euler orientation space into discrete bins. As an example, Figure 1.14 shows data collected on a surface perpendicular to the pressing direction of a pellet. The orientation distribution of the crystallite directions perpendicular to the sample surface is represented in the IPF. The orientation densities are color-coded from minimum to maximum values expressed in multiples of a random distribution (m.r.d) unit. In this example, the (0001) pole shows the maximum orientation density of 2.77 m.r.d, indicating that there is a texture, since the orientation densities are 0 m.r.d for a randomly oriented sample and infinity in a few directions for a single crystal [42]. A pole figure shows the position of a pole in the sample reference frame. In the same example, the (0001) pole figure shows the maximum orientation density (2.44 m.r.d) at the centre of the pole figure: both the IPF and pole figure indicate that the (0001) crystallographic poles are parallel to the pressing direction.

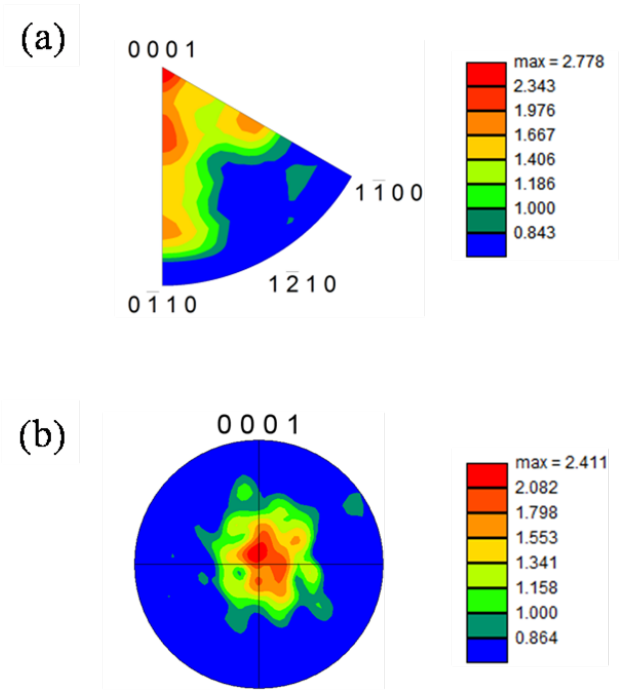


Figure 1.14: Representation of texture with color code legend of orientation densities in (a) Inverse pole figure and (b) Pole figure form.

Besides orientation data, another parameter called "Image Quality" (IQ) can be used to obtain the strain distribution in a microstructure [43]. The IQ value measures the average brightness of the peaks that are detected by the Hough transform, and is related to the pattern quality (see Figure 1.15).

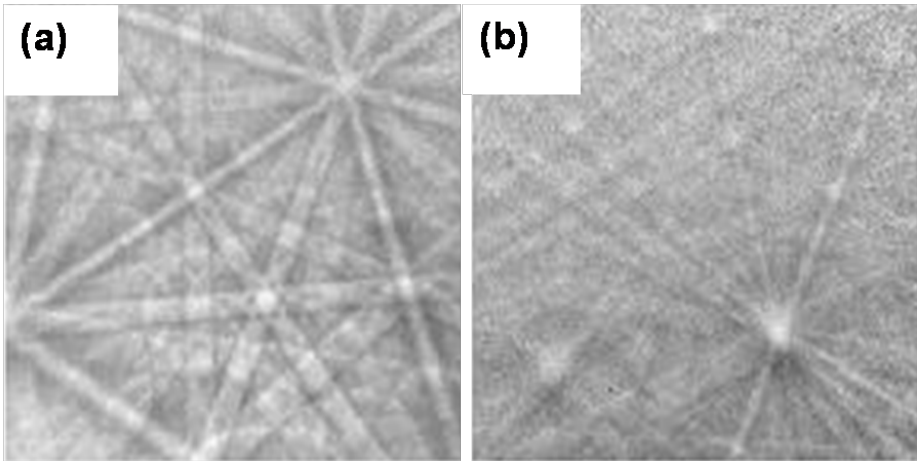


Figure 1.15: Shows a typical kikuchi pattern with (a) sharp and (b) diffused image quality [41].

The IQ map is obtained by mapping the IQ value at each point in an EBSD scan in gray

scale (see Figure 1.12(b)). Darker gray shades in the image denote lower IQ values, while lighter shades denote higher IQ values. It must be stressed that the IQ is not an absolute value but a function of material, technique and parameters used to index the patterns. The IQ value is calculated from the quality of observed Kikuchi bands. The quality of the band also depends on intensity, sharpness, contrast and noise. Moreover, these qualities are influenced by topography, grain boundaries, phases and residual strain present in the material [43]. Thus, any distortions in the crystal lattice within the diffracting volume will produce lower quality and more diffuse diffraction patterns. As will be described in the next section, this means that EBSD can be used to monitor the polishing of high quality surfaces to be used as substrates for combinatorial substrate epitaxy.

### 1.5.1 The EBSD for analysis of the epitaxial relationships

Historically, the EBSD technique was mainly used for studying rocks and minerals [34]. However, epitaxy studies by EBSD have provided valuable information such as the determination of elastic strain field across the interface of epitaxy, the study of dislocations in thin films or the- computation of texture and orientation relationships in CSE [45–48]. The high spatial resolution and depth resolution of EBSD enables the characterization of thin films at the microscopic scale. The typical spatial resolution for copper is 20 nm at 20 kV and the depth resolution for Au is 10 nm at 40 kV [37]. For metal oxides, the depth resolution is expected to be less than 10 nm because the electron density is smaller than in a metal. The depth resolution is good enough to capture the EBSD pattern explicitly from [5 nm-thick] metal oxide film [with no or little] interference from the substrate. Moreover, recent advances of spatial resolution in transmission EBSD seem promising to resolve the strain distribution across the interfaces [49].

In the context of Combinatorial Substrate Epitaxy, EBSD is also a useful tool to monitor the polishing and etching process of the polycrystalline substrate prior to the PLD thin film growth. As discussed in the previous section, the "Image quality" parameter can be used as a marker of the roughness and crystallinity of the surface. Any absence of crystallinity or presence of roughness over the substrate can fail in capturing EBSD patterns because only the first few nanometers of the surface are involved in the diffraction process. The polished surface having roughness of 10-100 nm failed to produce any pattern

because of roughness, deformation and/or impurities. The surfaces are therefore subjected to either chemical or thermal treatment untill the sharp EBSD patterns could be seen. Such substrates with good crystalline order could then be used for thin film growth. EBSD analysis was performed over the same area before and after epitaxial growth in order to investigate the epitaxial relationships between the film and the substrate.

## 1.6 X-Ray Scattering technique.

X-ray diffraction (XRD) is typically used to characterize the crystallographic structure of a sample. The incidence of an X-ray beam over a periodic array of atoms in a crystal leads to coherent elastic scattering if the incidence angle is equal to a deduced from the Bragg's law. The Bragg's condition for constructive interference is given by the equation ($n\lambda=2dSin\theta$), where n is an integer, $\lambda$ is the wavelength of incident X-rays, d is an inter-planar spacing in the lattice and $\theta$ is the angle between the incident X-rays and the diffracting planes.

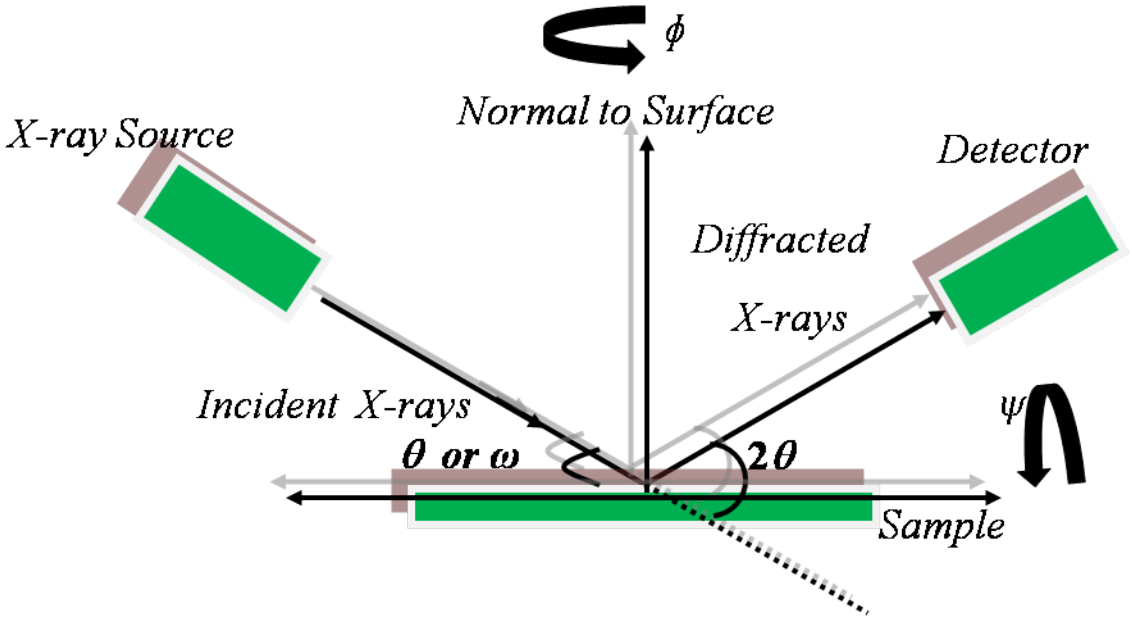


Figure 1.16: Typical schematic diagram of XRD.

In this work, XRD was used to identify the phase and its lattice parameters of the obtained polycrystalline substrates. This type of experiment is usually carried out in a powder diffractometer with Bragg-Brentano geometry (Figure 1.16). The X-ray source

generates X-rays by photoelectric effect. The generated X-ray beam from a Cu anode is divergent and contains a range of wavelengths. But, the technique requires parallel beam of X-ray with monochromatic in nature [50, 51]. Consequently, the divergent slit and optics in the instrumentation are used to make the divergent beam into a parallel beam. The X-ray beam may be filtered to obtain a monochromatic wavelength, and directed towards the sample. The diffracted intensities are detected and transferred to the digital interface. The position of the peaks determines the lattice spacings by Bragg's law. The width of the peak gives information about crystallite size and strain. The peak intensities depend on the nature and positions of the atoms in the crystal cell and other experimental parameters (Lorentz factor, temperature factor, absorption factor, geometry factor). The relative intensities are affected if the sample is textured, i.e., if the crystallites are not randomly oriented. Texture effects may be expected in samples submitted to uniaxial pressing; this is particularly the case of the SPS-sintered substrates prepared in this work. In order to characterize crystallographic texture, specific experiments are carried out in a dedicated diffractometer

## 1.7 Transmission Electron Microscopy

Transmission Electron Microscopy (TEM) is used to image the thin section of sample from the transmitted electrons. This technique is complementary to XRD. The interactions of electron beam with the specimen produce modulations in intensity of transmitted electrons. This transmitted electron beam is detected to derive the structure, phase and orientation. For higher resolution, HRTEM can be used to obtain the crystallographic structure of a sample at an atomic scale. In this regard, it is an invaluable tool to study the epitaxy at nanoscale because of its high resolution. Film thickness, interface and structure can be further resolved on a cross-sectioned prepared film (see Figure 1.17).

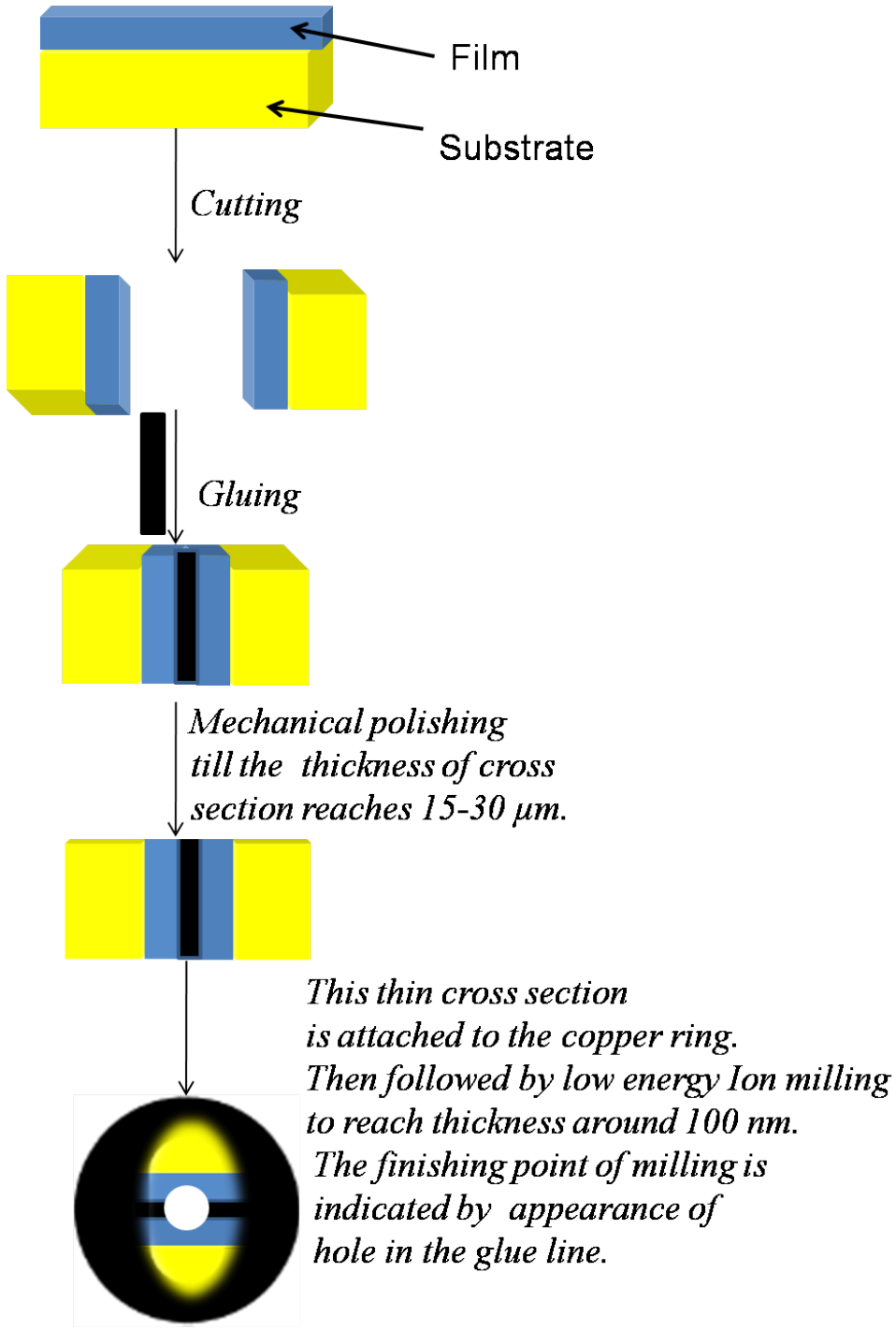


Figure 1.17: Illustration of cross-section preparation of thin film for TEM.

In experimental setup (see Figure 1.18), a field-emission gun produces energetic electrons by accelerating electrons by high voltage of 300 kV. Next, the energetic electrons condensed by lenses passed through the thin section of sample of 100 nm.

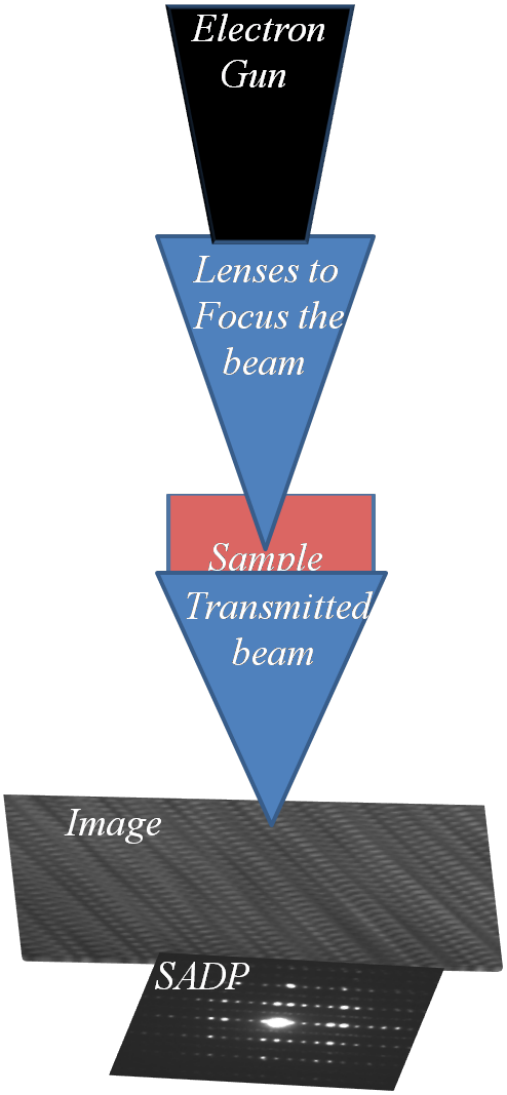


Figure 1.18: Typical schematic diagram of HRTEM.

The transmitted electrons undergo elastic scattering [52]. From this, high resolution image as well as diffraction pattern are obtained. Moreover, from inelastically scattered electrons using electron energy-loss spectroscopy(EELS) elemental composition information can be estimated. In addition, images were simulated by CrystalKit and MacTempas softwares. The experiments were performed by Dr O.Lebedev from CRISMAT,UCBN.

## 1.8 Thermoelectric measurements

The resistivity and Seebeck coefficient of the films can be measured using a standard four probe techniques and a steady state technique, respectively. In the standard four probe

technique used for resistivity measurement (see Figure 1.19(a)), the current is passed between terminal 1 and 4.

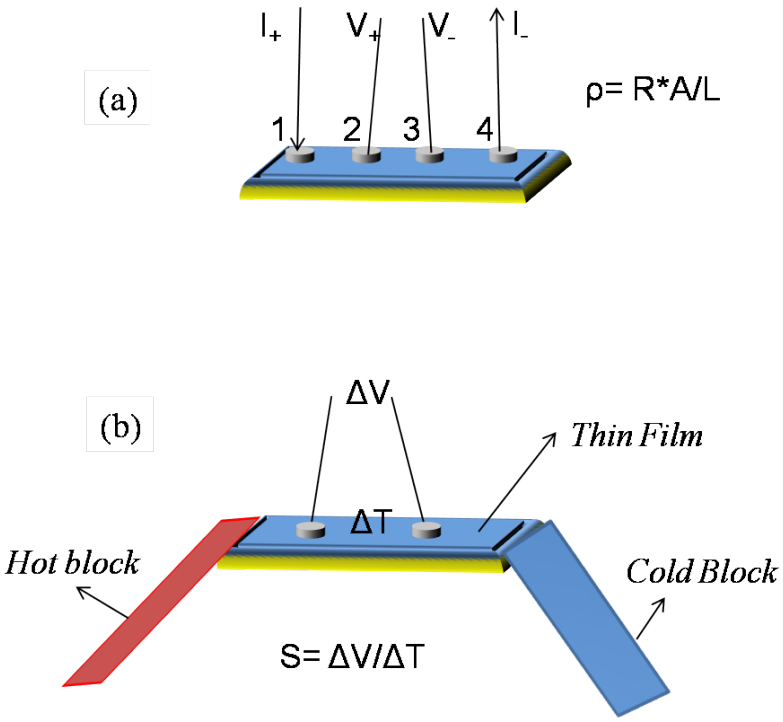


Figure 1.19: (a) Illustration of the four-probe method used to determine the resistivity ($\rho$) and (b) Steady-state method for measurement of the Seebeck coefficient ($S$).

The resistance to the current flow causes a voltage drop across the terminal 2 and 4, which is measured by a voltmeter. This voltage and the known current value are used to calculate the resistance of the sample by Ohm's Law at a given temperature. Then, this resistance value and the known length(L) and cross-sectional area(A) of the film are used to extract the resistivity ($\rho$).

The Seebeck coefficient is measured by creating a small temperature difference between the two ends of the sample ( see Figure 19(b)). For that, one end of the sample is glued to the cold end of the sample holder, while the opposite end is glued to the heater. The resulting temperature gradient between the two ends of the sample induces a voltage across the two ends due to the Seebeck effect. The temperature gradient and voltage are measured across the two terminals using a thermocouple and a voltmeter, respectively.

## 1.9 Atomic Force Microscopy

Atomic Force Microscopy (AFM) Bruker MultiMode 8 scan is used to characterize the roughness of a surface from a topography profile obtained in contact mode [53]. In the present work it was used to check the quality of the polished and etched surface of polycrystalline substrates. In AFM experiment, the scanning probe tip is moved over an area of the sample surface. During the scan, z moves and is adjusted to the surface morphology to generate a topography image. Piezoelectric Force Microscopy (PFM) is a technique derived from AFM that can be used to characterize the polarization of ferroelectric films. The typical schematic diagram of a PFM setup is shown in Figure 1.20).

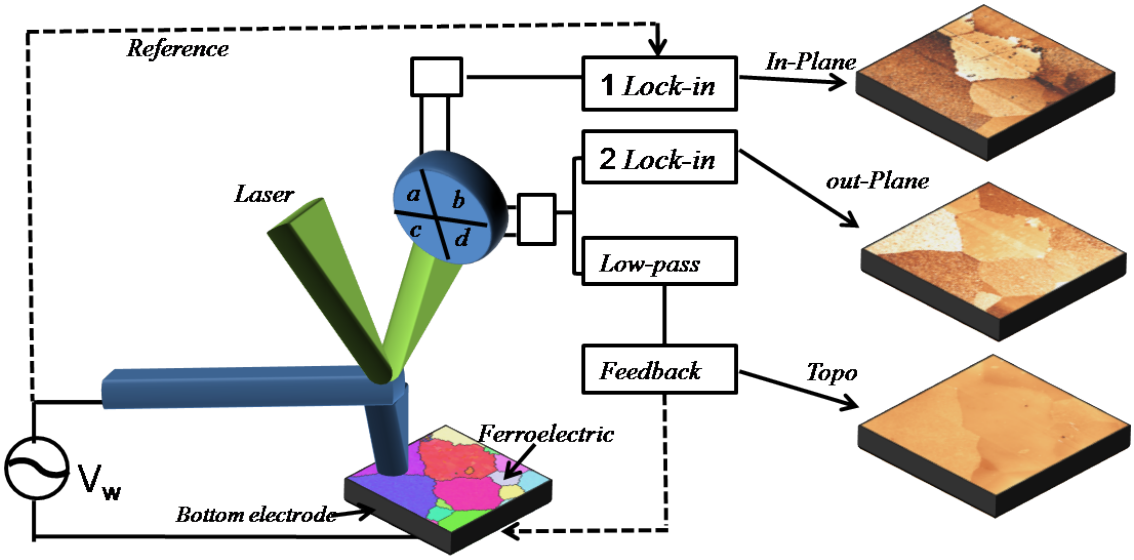


Figure 1.20: PFM experimental setup for simultaneous acquisition of topography and vertical and lateral polarization components. A function generator is used to apply an ac voltage Vw between the tip and the bottom electrode. The voltage-induced cantilever deflection is detected by a reflected laser beam on a four quadrant photodiode. The two signals: (a + c)-(b + d) and (a + b)-(c + d) are demodulated with two lock-in's representing the in-plane and out-of-plane signals, respectively. The average force on the cantilever during the scanning process is kept constant by a feedback loop, figure similar to reference [54].

The conductive tip in PFM applies a bias voltage to the ferroelectric material via the bottom electrode underneath. This causes the deformation of the material by converse

piezoelectric effect. The material deformation causes a displacement of the tip. The movement of the tip results in the deflection of the cantilever, which is detected by the reflected laser beam on a four quadrant photodiode. This enables to record simultaneously the topography and lateral and vertical piezoresponse of the sample. Moreover, the dynamic of the cantilever depends on the indentation force, the voltage bias, the local electrostatic force acting on the tip and the nature of material. PFM permits local polarization reversal that can be switched to confirm locally the ferroelectric nature of the material. PFM chracterization is also used to image ferroelectric structure domains at nanoscale and to obtain spectroscopy data of P-E characteristics.

# Chapter 2

# High-throughput synthesis of thermoelectric $Ca_3Co_4O_9$ films

This chapter deals with the synthesis of thermoelectric $Ca_3Co_4O_9$ epitaxial films using Combinatorial Substrate Epitaxy (CSE). We have synthesized textured alumina ceramic obtained by SPS of undoped commercial $Al_2O_3$ powders. Quantitative texture and structural analysis were carried out using a combination of Electron Back Scattering Diffraction (EBSD) and X-ray diffraction (XRD). These alumina ceramic polished, chemically etched and are used for growing nanostructured epitaxial $Ca_3Co_4O_9$ thermoelectric films using PLD with controlled microstructural defects. The structural quality of the thin film was investigated by Transmission Electron Microscopy, while the crystallographic orientation of the grains and the epitaxial relationships were determined by EBSD. The use of the polycrystalline ceramic template leads to nanostructured films that are in good local epitaxial registry, and results in the enhancement of the Seebeck coefficient to 170 $\mu$V/K at 300 K.

## 2.1 Introduction

Layered cobalt oxide $Ca_3Co_4O_9$(CCO) can be denoted as $[Ca_2CoO_3]^{RS}[CoO_2]_{1.62}$ to highlight the two layers that constitute the misfit structure and the ratio of the differing $b$-axis parameters [55]. The two layers are $Ca_2CoO_3$, a rock salt-layer (RS) and $CoO_2$, a cadmium iodide-like layer, respectively. These two layers have similar $a$ and $c$ lattice parameters with different $b$ lattice parameters, where the ratio of the b parameters for the $Ca_2CoO_3$ layer to $CoO_2$ layer is 1.62 (see Figure 2.1).

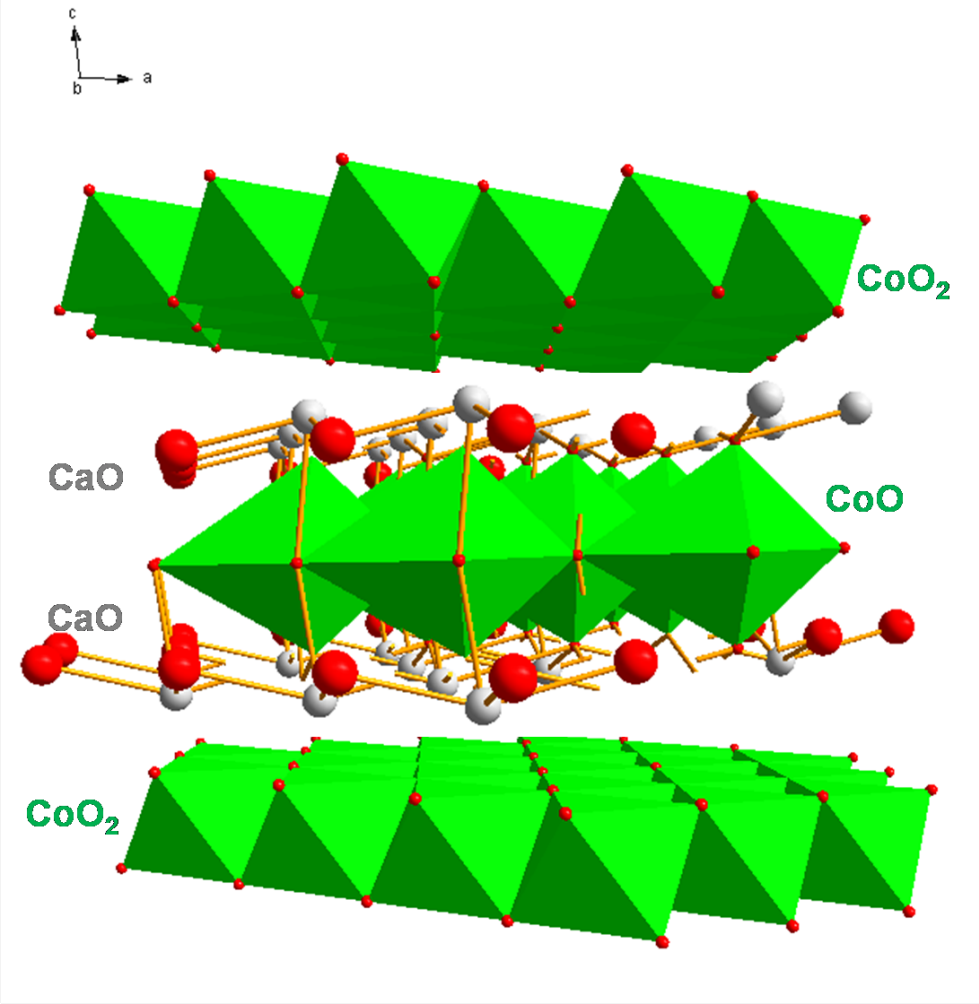


Figure 2.1: Crystal structural model of $Ca_3Co_4O_9$

The $Ca_2CoO_3$ layer is a distorted rock salt structure with in-plane Co-O distances of 2.28 Å and out-of-plane Co-O distances of 1.82 and 1.89 Å . The $CoO_2$ layer has edge-sharing $CoO_6$ octahedra with Co-O distances of 1.86 and 1.96 Å [55]. CCO is particularly interesting material because of its thermoelectric property. Thermoelectricity is indeed the

property of a material that converts heat into electricity and vice versa through Seebeck and Peltier effects, respectively. Thus, it is useful for the practical applications, such as refrigeration, cooling microelectronic devices, and can provide an energy source from waste heat [56].

The quality of thermoelectric materials is determined by the unit less constant called figure of merit zT, which is estimated via Eq. 2.1, where T, S, $\rho$, and $\kappa$ are absolute temperature, Seebeck coefficient, electrical resistivity, and thermal conductivity, respectively.

$$zT = \frac{S^2 T}{\rho\kappa} \tag{2.1}$$

Therefore for thermoelectric applications, it is required to prepare materials exhibiting low electric resistivity as well as thermal conductivity, and high Seebeck coefficient. The electron contribution to the thermal conductivity is usually proportional to electrical conductivity. Consequently, in most of the materials, a high thermal conductivity is associated with a high electrical conductivity. Thermoelectric figure of merit can be enhanced by the band engineering and nanostructuring. Seebeck coefficient is a function of energy from the Mott's relation, which suggests a steep increase of density of states in the proximity of Fermi level that enhances the Seebeck coefficient [57]. The band engineering can be achieved by reducing the dimension of the materials into thin film(2D), nano wire (2D) and superlattice of film or wire accompanied with defects to achieve the desired band structuring [58]. Moreover, the phonon contribution to the thermal conductivity can be reduced by increasing the phonon scattering at grain boundaries or internal interfaces and mutiscale hierarchical architectures [59]. For these reasons, several nanostructured thermoelectric materials have been developed, such as nanowires, superlattices, and nanocomposites [60–64].

In this perspective, we believe CSE can be useful to engineer the particular composition, grain size, texture and nano/micro-structural features. Such a substrate can provide a versatile route to control the Seebeck coefficient and lattice thermal conductivity in order to maximize the figure of merit in the thin films. Thus, high-throughput synthesis of CCO films were fabricated by CSE. The deposition of CCO film can also represent a proof-of-concept by measuring a macroscopic parameter, and compare it with bulk and thin films. Also it appears that the epitaxial growth of CCO films can be controlled by

using the oriented $Al_2O_3$ substrates [65, 66]. However, the precise control of the grain size is much more difficult when depositing on single crystals. Polycrystalline $Al_2O_3$ substrates have thus been used to obtain the nanostructured CCO with *c*-axis alignment [67]. While the deposited films are more strongly bound to the (00*l*) plane, the grains of the $Al_2O_3$ substrates still contain various crystal directions, and for example the (00l)-oriented planes exist randomly among the grains [68].

In this aspect, we have prepared an $Al_2O_3$ polycrystalline substrates textured using SPS, on which a thin film is deposited by the PLD technique. The polycrystalline $Al_2O_3$ with controlled grain size acts as seeds for localised epitaxial growth. With the presence of grain boundaries, the coalescence of the films is expected to be different on polycrystalline ceramics than on single crystal substrates. In addition, this high-throughput synthesis approach allows a control the grain size and enables to study the influence of the misorientation at grain boundaries in CCO growth. The structural quality of the thin film was investigated by HRTEM, and the crystallographic orientation of the grains and the epitaxial relationships were determined by EBSD. The use of the chemically etched CCO substrate leads to nanostructured films that are in good local epitaxial registry, and results in the enhancement of the Seebeck coefficient to 170 $\mu$V/K at 300 K.

## 2.2 Experimental

Commercially available undoped $\alpha$-$Al_2O_3$ (Chempur GmbH, Germany, purity of 99.97%) powders were densified using conventional sintering and SPS. We used powders of $Al_2O_3$ and sintered them at two temperatures 1400°C and 1700°C, respectively. The heating rate was kept at 90°C/min until reaching 450°C under the uni-axial pressure of 16 MPa. Then, it was increased up to 100°C/min with a simultaneous increase of the uniaxial pressure of 100 MPa to reach the final sintering temperature of 1400°C, and 1700°C for the two samples, for the duration of 20 and 10 min, respectively. Finally, the samples were cooled down to room temperature in the rate of 90°C/min. The samples were annealed at 1200 °C for 12 hour to remove the carbon contamination from graphite over the surface.

The $Al_2O_3$ polycrystalline pellets were cut into typical dimensions of 5x5x0.5mm$^3$. The samples were first subjected to mechanical polishing to remove the scratches made

by silicon carbide papers with roughness down to 10 $\mu$m for 1 hour. Then, the pellets were polished by an automatic machine using diamond liquid (DL) pastes with the grain size of 3 $\mu$m and 1 $\mu$m grain sizes, respectively, for about 2 min, in order to attain a mirror-like surface. Then, a solution of colloidal silica (CS) was used for 1 min as a final polishing step.

Atomic Force Microscopy (AFM) Bruker MultiMode 8 scan was performed for verification of quality of polished and etched surface of polycrystalline substrate.

The deposition of the CCO films was performed at 650 °C under 0.2 mbar of oxygen pressure using the pulsed laser deposition technique ($\lambda = 248nm$). A laser energy of 2 J/cm$^2$ and repetition rate of 3 Hz were typically used. The target-to-substrate distance is adjusted to 5 cm. The composition of the films was checked by Energy Dispersive Analysis and found to be close to the target within the experimental error.

Structural and microstructural characterization of the ceramics and films were carried out using electron backscatter diffraction (EBSD). The samples were mounted at a 70°-tilt angle from horizontal in a scanning electron microscope (FEG-SEM Carl ZEISS SUPRA 55)) operated at 20 kV. Gold was added along the edges of the samples to avoid charging effect on the surface during the experiments. Kikuchi patterns were recorded with a working distance of 10-15 mm and an aperture size of 60-120 $\mu$m, and indexed automatically by the EDAX orientation imaging microscopy (OIM$^{TM}$) software (v.6). Automated EBSD scan was performed by scanning the surface of the sample with a beam step size of 0.2 $\mu$m. EBSD map was generated after several clean up methods, which attempts to clean-up the erroneous data (due to a pore, a grain boundary, an impurity at the surface that make a wrong indexation). To clean a map, several parameters must indeed be considered. Here, (i) the minimum grain size is set to 5 pixels, (ii) the minimum Confident Index to 0.1 and (iii) two neighboring points with a misorientation greater than 2° are considered to be the trace of a grain boundary. The average Confidence Index after this procedure of cleaning is larger than 0.1 for all the samples.

TEM investigation were carried out using a FEI Tecnai G2 30 UT microscope operated at 300 kV (point resolution 1.7 Å ). Image simulations were made with CrystalKit and MacTempas software. Cross-section samples were cut parallel to $Ca_3Co_4O_9/Al_2O_3$ interface plane, mechanically polished to a thickness of about 15 $\mu$m followed by Ar+

ion beam milling under grazing incidence with respect to the surface. A soft regime of ion milling has been used to prevent any possible artefacts during TEM specimen preparation. The structure and epitaxial relationship with the influence of grain orientation, boundary and misorientation angle between the grains have been investigated in details. The composition of the films was checked by Energy Dispersive Analysis and found to be close to the target within the experimental error.

Seebeck coefficient ($S$) and the resistivity ($\rho$) of the films were measured as a function of temperature ($T$) in Physical Properties Measurements System (PPMS, Quantum Design), using a standard four probe techniques ($\rho$) and a steady state technique ($S$).

Texture and structural variations of the ALO substrate were investigated at a large macroscopic using a 4-circle X-ray diffractometer setup equipped with a Curved Position Sensitive detector (CPS120 from INEL SA) and with monochromatized Cu K$\alpha$ radiation. The overall texture strength is expressed in multiples of a random distribution (m.r.d.) square units and varies from 1 (random powder) to infinity (perfect texture or single crystal), and this is used to compare the texture strength of various samples exhibiting similar Orientation Distrubutions (ODs) [69]. The hardness and Young's modulus of ALO samples were calculated from the nanoindentation experiments. Superficial hardness profiles were obtained with a MTS XP TM nanoindentation device using the continuous stiffness measurement mode. Nanohardness was measured using the Oliver and Pharr methodology. Two indents were performed on each sample (25 indents - 5x5; X-Y-space: 90-160 $\mu m$; indentation depth: 120 $\mu m$). The loading path contains five force increments with holding time of 30s, and unloading to 90% of the applied force. The loading time was 15s and the maximal applied force kept to be 5 mN. Young modulus values were measured during the 5 unloading with the slope at maximum loading and then averaged. The extracted parameters are the mean values of 25 measurements. The density of the samples was measured from Micrometrics AccuPyc 1330 Gas Pycnometer.

## 2.3 Results and Discussion

### 2.3.1 Preparation of dense substrate

#### Conventional Sintering

To stabilize the epitaxial growth of CCO films and thermoelectric measurements, dense polycrystalline substrate has to be obtained. In this regard, we have utilized the conventional sintering of commercial $Al_2O_3$ powder (see Figure 2.2(a)) at 1500°C for 10h and obtained density of 85%.

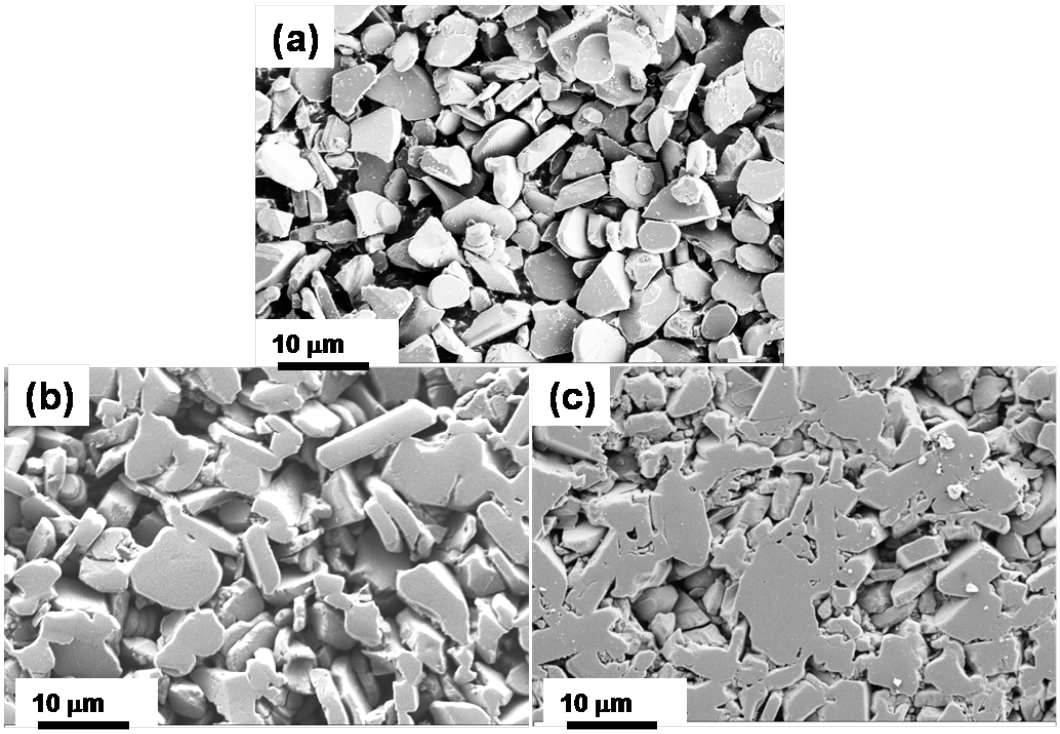


Figure 2.2: SEM image of $Al_2O_3$ (a) commericial powder and polished ceramic from conventionally sintered at 1500°C for (b) 10hr and (c) 24hr dwell time.

The microstructure of such surface is highly porous due to the incomplete densification (see Figure 2.2(b)). Even if, the dwell time is raised upto 24hr, we observed a slight increase in density of 88%, but the material still remains porous (see Figure 2.2(b)). The grain growth is increased in both the conventionally sintered samples in comparison to grain size of starting powder. However, it was difficult to obtain high density with low porosity by this conventional sintering.

### Spark Plasma Sintering

Thus, we have investigated an another alternative method namely SPS technique for sintering to improve the densification of $Al_2O_3$ substrate. In order to optimize the experimental conditions to obtain high density, we have carried out SPS simultaneously at 1700 °C and 1400 °C under a uni-axial pressure of 100 Mpa. Indeed, the experience from conventional sintering of $Al_2O_3$ powder suggested that the optimizing temperature is to be 1500°C. As a result two sintering temperatures of 1700 °C and 1400 °C were chosen. Further, to reach a better densification, an uni-axial pressure of 100 Mpa was used to minimize the coarsening and to initiate the sintering process. As a result, the relative density was calculated equal to 96% and 99.9% for 1400 °C and 1700 °C, respectively. For further understanding of the densification process in SPS, density profile during sintering is done. This Figure 2.3 displays the typical evolution of the relative density as a function of dwell time.

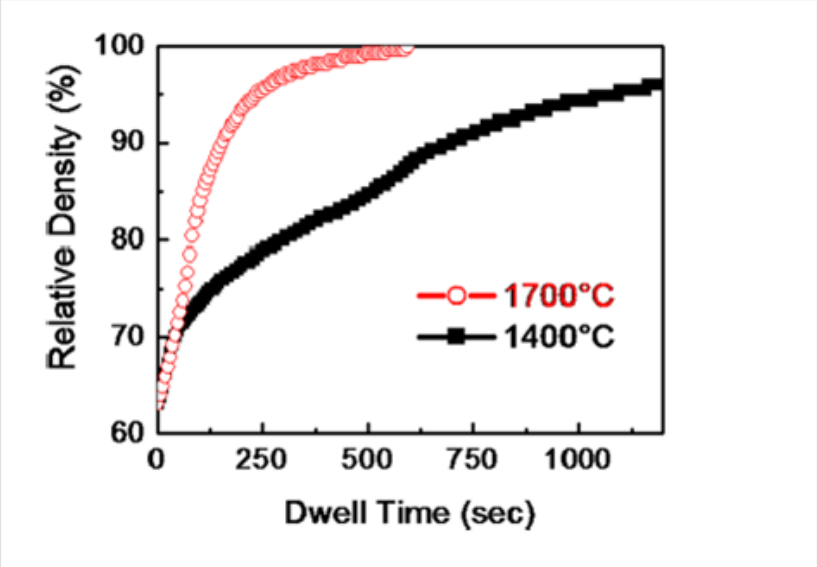


Figure 2.3: Relative density for samples sintered at 1700 °C and 1400 °C under a uniaxial pressure of 100Mpa, plotted as a function of dwell time. The plot was derived from the SPS data of piston displacement versus time [70].

It further indicates that the densification increases linearly with dwell time and increase much faster at elevated temperatures. At saturation, within the spanned dwell times, the process leads to a relative density of 96% at 1400 °C, whereas at 1700 °C, the final relative density reaches the maximum value of 99.99%. The increase in density at higher

temperatures is due to fast atomic diffusion at grain boundaries during sintering process [70].

### 2.3.2 Characterization of $Al_2O_3$ substrate

Then, a systematic evaluation of SPS sintered $Al_2O_3$ samples were done to examine the mechanical property, surface roughness, texture and microstructure. This study can enable to choose the appropriate substrate for growing the CCO. Substrate needs to be mechanically stable in order to withstand the pressure during cutting, polishing and handling. Further, the polished surface has to be highly smooth, and free from impurities to provide a good epitaxial growth. Moreover, the microstructural study of the substrate can provide an understanding the physical property of the grown film.

#### Mechanical Property

Young's modulus and hardness are measured from nanoindentation experiments along parallel and perpendicular directions of $P_{SPS}$ (see Figure 2.4).

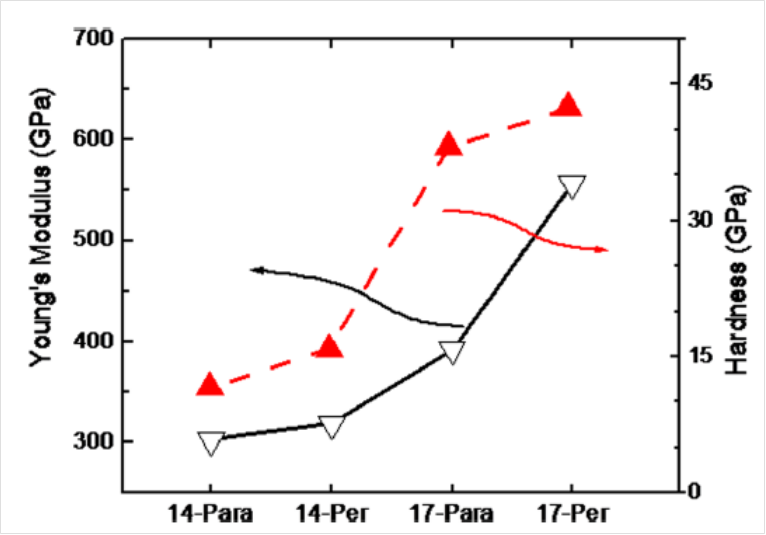


Figure 2.4: Hardness and Young's modulus measurement for sample sintered at 1400 °C and 1700 °C for indentation parallel and perpendicular to the direction of $P_{SPS}$. (Note: per and para stand for indentation perpendicular and parallel to the direction of uniaxial pressure, respectively.

As sintering temperature increases, Young's modulus and hardness increase from 318

to 556 GPa and 15 to 42 GPa, respectively, which is mainly due to an increase in density and grain size [71,72]. In fact, mechanical property substantially increases due to the presence of preferred orientations in the polycrystalline material. The increase in anisotropy of mechanical properties is also a common consequence of preferred orientations present in polycrystalline materials. Grain boundaries can indeed strongly affect nano-indentation measurements and give locally higher values than those obtained in the middle of the grains. As a consequence, a large variation in hardness and Young modulus are observed. Also, higher mean values are obtained on perpendicular samples, which are attributed to a higher grain boundary density as compared to the one observed for parallel samples. Furthermore, the disordered structure of the grain boundaries can prevent the moving of dislocations in a continuous slip plane, leading to an increase in stress (depending on the diameter of the grains) [73].

In summary, our studies showed that the sample sintered at 1700 °C presents a better mechanical strength than sample prepared at 1400 °C. The preferred orientations along $P_{SPS}$ lead to anisotropic in the mechanical property. Moreover, higher mechanical strength is obtained for the ceramics along the direction of $P_{SPS}$.

**Substrate Etching**

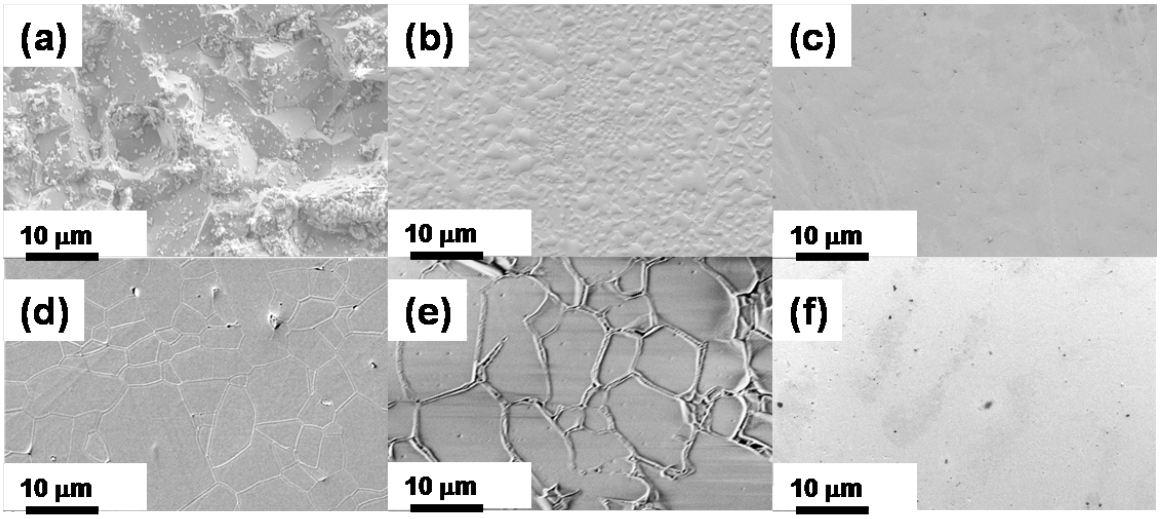


Figure 2.5: SEM microstructure of (a) as prepared alumina ceramic surface, (b) mechanically polished surface and thermally etched surface for (c) 12 min, (d) 2hr and (e) 24hr (f) chemically etched surface.

In order to have a highly dense and mechanically stable surface for epitaxial film growth, the obtained ceramic surface has to be fine polished and cleaned (see Figure 2.5(a)). The well polished surface is shown in Figure 2.5(b). The surface exhibits clusters of protruded hemispherical grains and scratches that spread out uniformly. Such grains are the contaminants attached to the surface from diamond polishing liquid, and scratches come from polishing disk. In order to remove the surface contaminants and release the strain generated during polishing. The polished surface was thermally quenched at 1200 °C with different time intervals of 12 min, 2h and 24h, as shown in Figure 5(c),(d) and (e), respectively [74]. In thermal quenching, the substrate was placed inside a furnace kept at 1200°C for the duration, and quenched to room temperature. The surface quenched for 12 min is flat, and reveals the partial grain boundary, while, the grain boundaries are completely revealed for quenching time of 2h. However, the grain boundary highly protrudes due to increase in grain boundary diffusion for longer quenching time of 24h. Sometimes in the polished surface was etched in 5 % HF:$HNO_3$ solution for 9s to remove the surface contaminants and release the strain that generated during polishing (see Figure 5(f)). The chemically etched surface displays no trace of such protruded hemispherical grains that were observed over the polished surface.

### Substrate roughness

Further, surfaces were investigated by AFM (see Figure 2.6).

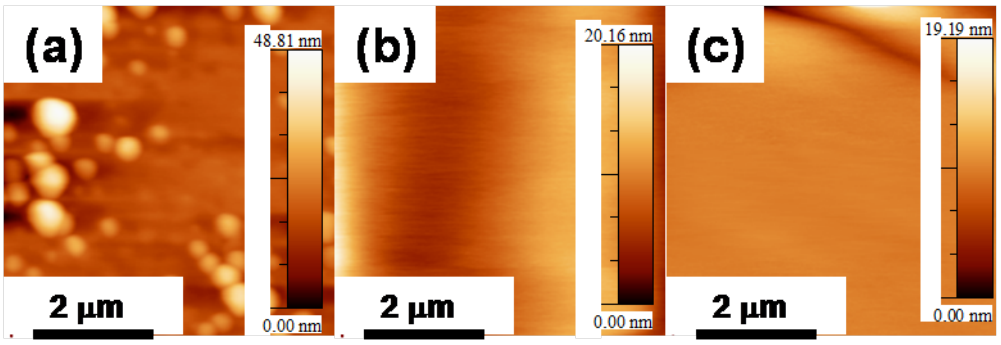


Figure 2.6: AFM topography images of surface that were (a) mechanically polished with RMS roughness 15.4 nm, (b) thermally etched for 12 min with RMS roughness 1.1 nm and (c) chemical etched with RMS roughness 4.8 nm.

In this regard, AFM topography image obtained on the mechanically polished surface shows protruded hemispherical grains (see Figure 2.6(a)) and also such protruding hemispherical grains are previously seen in the microstructure (see Figure 2.5(b)). The protruded hemispherical grains diameter are relatively small as previously seen in the microstructure, because the scan was performed on small region and moreover the limitation in the AFM instrument has a limitations of scanning large area. As a result, a low RMS roughness of 15.4 nm is obtained. The thermally quenched surface shows low RMS roughness of 1.1 nm in comparison with the chemically etched surface of 4.8 nm (see Figure 2.6(b) and 2.6(c)). Thus, the thermal etching causes melting of the surface, which leads to a less roughness. The higher roughness observed in the chemical etching process suggests that there are still some of the scratches caused by polishing. Thus, the thermally etched surface is a better option in terms of low surface roughness.

### 2.3.3 Microstructure and texture characterization

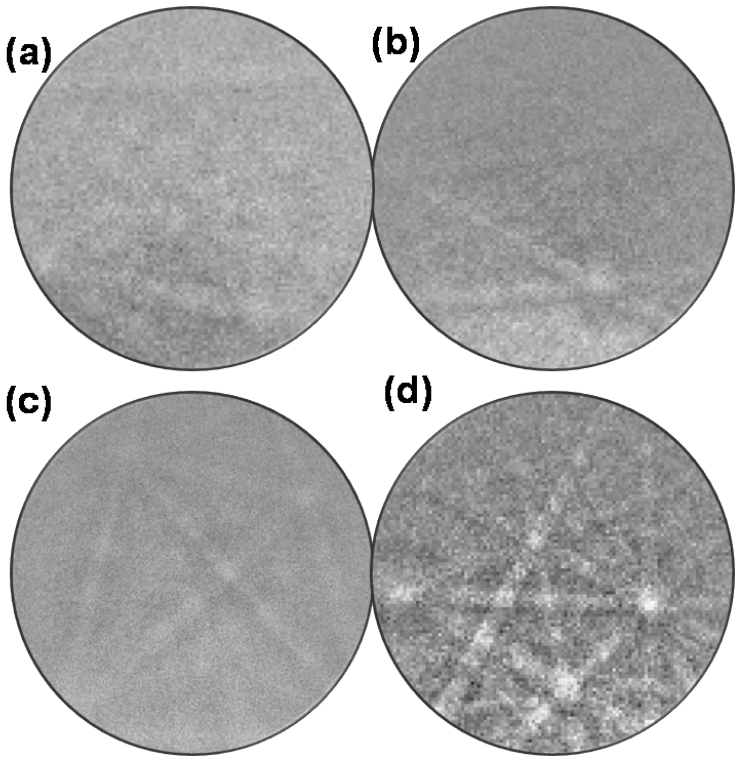


Figure 2.7: EBSD pattern obtained on the surface that were (a) mechanically polished, thermally quenched for (b) 1 minute and (c) 5 minutes and (d) 12 minutes.

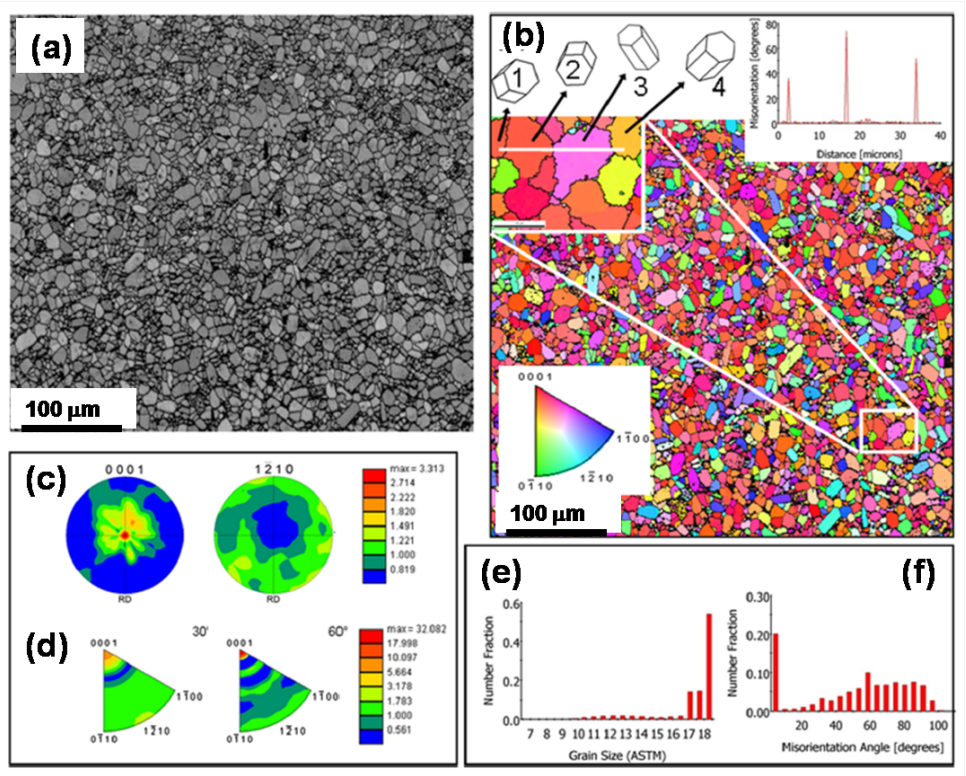


Figure 2.8: (a) Image Quality map (b): Color coded IPF map showing the grain size for the sample sintered at 1400 °C recorded along the surface perpendicular to uniaxial pressure. The color code corresponding to the crystallographic orientation is given in the stereographic triangle with a small region magnified with the lattice marked with their misorientation angle shown in the top. Wire frames visualize the orientation of the selected crystals. (c) Calculated texture index, (d) MDF, (e) Grain size, and (f) misorientation angle distribution.

The qualitative and quantitative microstructural analysis by EBSD were performed on the samples prepared at 1400 °C and 1700 °C. The surface needs to be crystalline and free from impurities in order to observe the EBSD patterns. In this context, the exposure time of thermal quenching has to be optimized. For example, the EBSD pattern bands seen on the mechanically polished surface are extremely blurred, diffused and has a weak signal (see Figure 2.7(a)). This could be attributed to strain in the surface crystal planes that leads to diffused bands due to polishing [75]. Further, the polished surface was thermally quenched at different times, and then optimized until an indexable EBSD pattern is obtained. Substrate that are thermally quenched for 1 min showed few bands of EBSD pattern that are diffused (see Figure 2.7(b)). For a quenching time of 5 min (see Figure 2.7(c)), most

bands are less intense and diffused, indicating that the surface is still strained. Visible indexable bands are seen for substrates that are quenched for 12 min, and are used for automated EBSD scan (see Figure 2.7(d)).

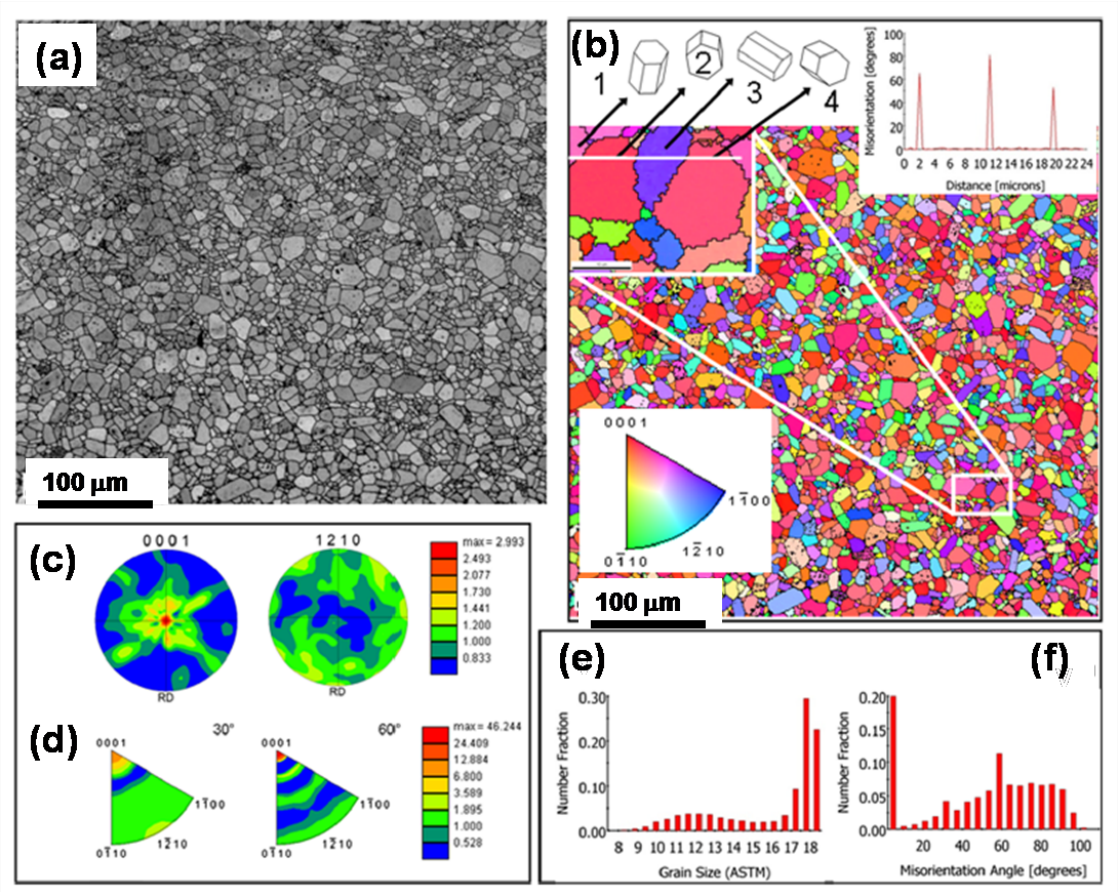


Figure 2.9: (a): Image Quality map (b): Color coded IPF map showing the grain for the sample sintered at 1700 °C recorded along the surface perpendicular to uniaxial pressure. The color code corresponding to the crystallographic orientation is given in the stereographic triangle with a small region magnified with the lattice marked with their misorientation angle shown in the top. Wire frames visualize the orientation of the selected crystals. (c) Calculated texture index (d): MDF, (e) Grain size, and (f) misorientation angle distribution.

The EBSD data describe the overall good Image Quality (IQ) maps (see Figures 2.8(a) and 2.9(a)). Such IQ images are formed by mapping the IQ index obtained for each point in an EBSD scan onto a gray scale in which the darker gray shades denote lower IQ values in the image. The average image quality for the scan is 961 and 914 for Figures. 2.8(a)

and 2.9(a), respectively. The overall IQ maps exhibit high amounts of gray over the grains confirming homogeneity and crystallinity. However, in the IQ map, the presence of grain boundaries with some areas appearing dark points over the whole grain is due to rough surfaces or residual porosities [76]. There are, however, less dark areas in the IQ image for the sample sintered at 1700 °C sample, and grain boundaries appear weaker, indicating that crystal state is less perturbed at high temperatures.

EBSD orientation maps of the sample surface recorded perpendicular to $P_{SPS}$ illustrate the crystalline direction of each grain aligned with the pressing axis as seen in color coded Inverse Pole Figure (IPF) definition (see Figures 2.8(b) and 2.9(b)). A significantly larger fraction of grain shows that most of the <0001> crystal directions are aligned with $P_{SPS}$. In order to quantitatively estimate the orientation distribution, the principle planes of (0001) and $(1\bar{2}10)$ pole figures were computed from the OD ( see Figures 2.8(c) and 2.9(c)). The (0001) pole figure shows the maximum orientation density around 3 m.r.d. at the centre of the pole and implies that the <0001> parallel to the $P_{SPS}$. While the $(1\bar{2}10)$ pole figure shows isotropic distribution where $a$- and $b$-axes are randomly oriented around $c$-axis indicates a cyclic-fiber texture.

In order to obtain a larger macroscopic view of orientation distributions in the samples, we coupled with X-ray diffraction analysis for an overall texture determination, probing around $10^{8}$ crystals. Strong variations in the intensities of X-ray diffraction diagrams are measured for various sample orientations , which indicates the presence of a relatively pronounced texture. The calculated pole figures of the main crystallographic directions of $Al_2O_3$ (see Figure 2.10) show a relatively strong <001> cyclicfiber-texture for the samples sintered at 1400 °C and 1700 °C. The <001> fiber character of the texture is confirmed by the axially symmetric distribution of the (300) pole figure (see Figure 2.10), and is consistent with the EBSD analysis. In addition, the overall texture strength, maxima of OD, pole figures, and inverse pole figures do not show any significant variation with the sintering temperature from both EBSD and X-ray texture analysis. However, subtle differences are still observed between the X-rays and EBSD pole figures in density levels.

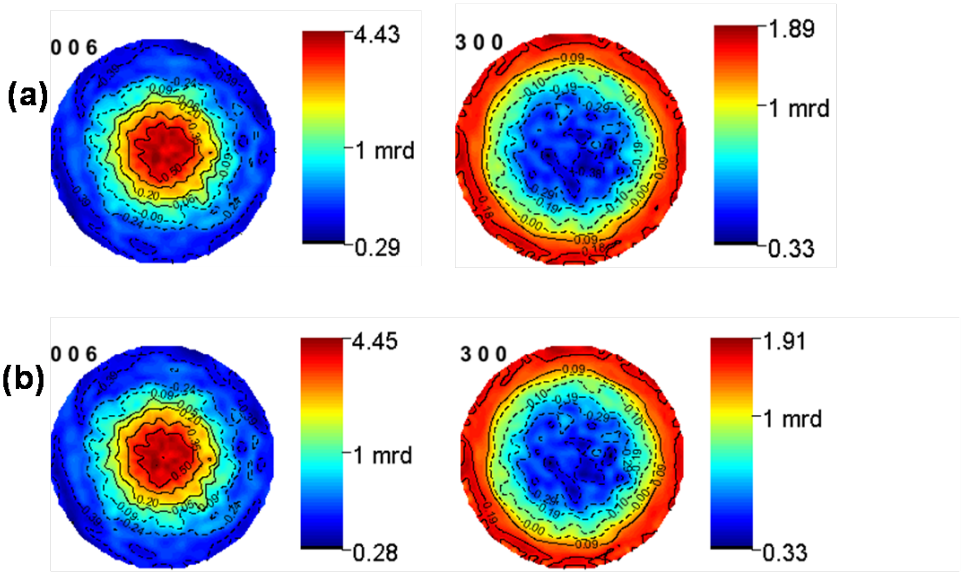


Figure 2.10: Shows the 006 and 300 normalized pole figures reconstructed from the Oriented Distribution Function for the (a) 1400 °C and (b)1700 °C sintered samples. The scale used is logarithmic density scale, equal-area density projections.

The non-axial symmetry is seen in EBSD pole figures (which is inconsistent with the axially symmetric applied load in the SPS) due to the probing of an insufficient number of crystallites in the measurements. Although data binning and FWHM of the Gaussian component used during the OD calculation are enabled to meet OD resolution. As a result, these extra orientations introduced in EBSD data decrease pole density levels of the (0001) pole figure, compared to X-ray refinements. The applied uniaxial pressure during SPS process results to deformation at high temperature and leads to crystallographic slip of individual grains. Slip should occur on specific crystallographic planes along specific crystallographic directions, and the slip planes are the planes that have a high atomic packing density [77]. This indeed could be the possible mechanism for $Al_2O_3$ texture development along <0001>. Moreover, to accommodate a significant axial strain in the hot pressing conditions of SPS process, a possible rotation of the grain having the (0001) planes oriented perpendicular to $P_{SPS}$ may occur. This interpretation is supported by the relatively large degree of grain orientations observed. Thus, we have successfully achieved the (0001) fiber textures with maximum densities of 5 times greater than the previously observed ones [78]. Moreover, our quantitative texture analysis are clearly consistent with the thermodynamically favored (0001) slips to withstand the applied uniaxial pres-

sure [79–81]. Misorientation Distribution Functions (MDF), calculated using EBSD data (see Figures 2.8(d) and 2.9(d)), reach a maximum for (0001) along the sample's normal direction and further increase with temperature, which is attributed to the grain boundary energy minimization under thermal stress during the SPS process. The inset of Figure 2.8(b) (top one) shows the arrangement of grains with a peculiar misorientation angle. The surrounding grains are probably formed due to the simultaneous uniaxial load and the electric field. The absence of orientation correlation at the grain boundaries with the crystal lattice can be understood by the point to point misorientation profile, as it shows three peaks at the grain boundaries (See Inset Fig. 2.8(b)). This particular values of 30°, 60° , and 90° high-angle misorientation angle could be attributed to mass transport between the planes of grain boundaries dictated by surface energy, boundary shape, and grain size during the SPS consolidation [70]. Moreover, the atoms move smoothly from the convex surface on one side of the grain boundary to the concave surface of the other side, rather than the reverse direction. The reason is that the chemical potential of the atoms under the convex surface is slightly higher than that of the atoms under the concave surface (for a section across two grains) [70]. Also, the driving force for the grain growth is mainly the decrease in free energy that accompanies the reduction in the total grain boundary area. Thus, the bimodal grain size distribution increases the intensity of small grains as seen from EBSD data and enhances the packing density to almost full density for the samples sintered at 1700 °C. On the contrary, the average grain size increases, and the grain size and shape remain within a fairly narrow range of normal grain growth. As a result, there is normal unimodal grain size distribution for the samples sintered at 1400 °C, indicating the normal grain growth (see Figure 2.8(e)).

In summary, this analysis reveals that the alumina sintered at 1400°C is porous with an isotropic grain growth, whereas the 1700°C sintered sample shows less porosity with fine grains, but exhibits anisotropy in the grain growth. Moreover, the topological connectivity of (0001) grains are distributed maximum above 60° misorientation angle. Further, the texture computed by combined analysis of XRD and EBSD give more intuitive picture on global texture and local texture of (0001) along $P_{SPS}$, respectively. This explains the anisotropy in mechanical property due to texture along the (0001) (see Figure 2.4).

**As a conclusion, we highlight the important observations from the substrate characterization that can be relevant for CCO epitaxial growth :**

1. The surface roughness can be reduced after etching process to ensure a good epitaxial growth.

2. The (0001) textured surface can promote textured growth of (0001) CCO film. Moreover, the grain boundary, grain size and misorientation angle can engineer the film structure.

### 2.3.4 CCO films grown on thermally etched alumina substrates

#### Microstructure

CCO films were grown on the substrates that were sintered at 1400 and 1700 °C. These substrates were thermally etched for 12 min before the deposition by PLD. The films grown on the substrates sintered at 1400 °C show elongated grains and exhibit porous microstructure for the thicknesss of 50 nm (see Figure 2.11(a)).

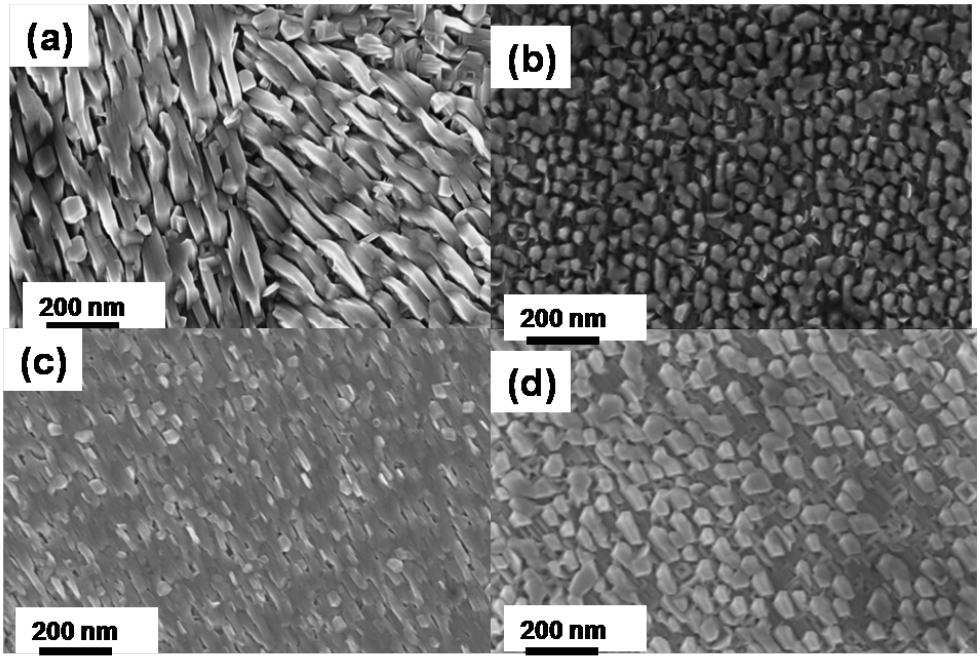


Figure 2.11: Shows the micro-structure of film deposited over thermally etched alumina substrate sintered at 1400 °C of thickness of (a) 50 nm and (b) 100 nm. Corresponds to film thickness of (c) 50 nm and (d) 100 nm for 1700 °C sintered substrate

The film grown on 1700 °C sintered substrate, elongated grains are dense and highly coalesced together (see Figure 2.11(c)). As the thickness of film increases, it tends to form smaller grains with high porosity for samples sintered at 1400 and 1700 °C, respectively (see Figure 2.11(b) and 2.11(d)). Therefore, the film grown on both the substrates are not coherent, as the surface morphology changes uniformly over the surface. Also, the surface morphology relaxes by formation of randomly oriented grains when increase in the film thickness.

### Structural resolution by TEM

In order to resolve the structure, low magnification TEM micrographs were performed for the $Ca_3Co_4O_9$ film grown on 1700 °C sintered substrate with thickness of 50 nm. The surface of the substrate is extremely flat as expected from the thermal etching process that leads to the surface relaxation (see Figure 2.12(a)).

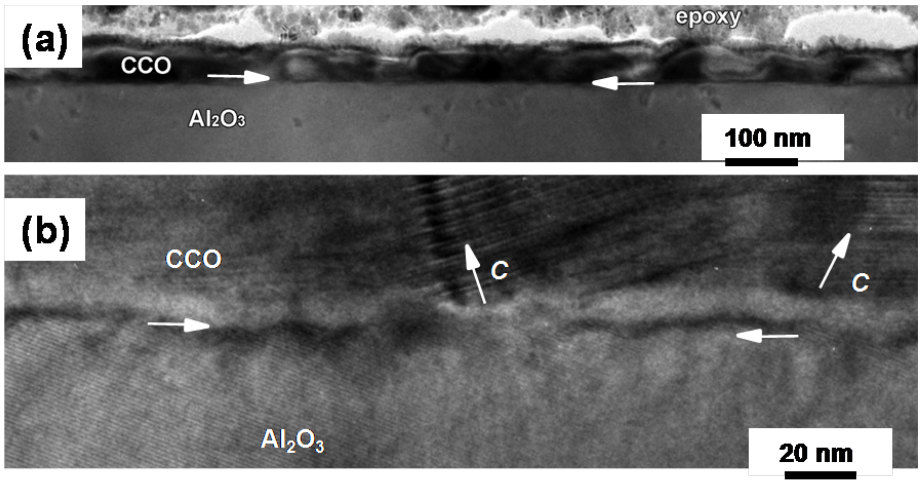


Figure 2.12: (a) Low magnification cross-section bright-field TEM micrograph of CCO film grown on thermally etched 1700 °C sintered substrate. (b) The magnified HRTEM micrograph of region in (a) is shown. The horizontal white arrows indicate the interface. While the tilted arrows indicate the c-axis of the film.

However, the surface of film is irregular and shows different contrast across the substrate grain. The atomic resolved structure of interface is better seen in magnified HRTEM micrograph (see Figure 2.12(b)). The film appears bright, and no crystallinity can be seen just above the interface. This is the region of amorphous CCO film with thickness of 2

nm. However, film grows with random *c*-axis above the uniform amorphous film, and the structure is highly disordered. This could explain the surface morphology as seen in Figure 2.11(c), which is due to a mixture of amorphous, porous and randomly oriented nano grains. Also, such morphology can originate from the roughness of the substrate surface. The randomly oriented nano-grains, and amorphous structure enhance the interfacial electron scattering, and lead to increase in resistivity. Consequently, the obtained samples are very resistive because of insulating behaviour, and could not be measured. In addition, the acquisition of EBSD pattern was not possible over the film due to disorderness of the film structure. The formation of such an amorphous region on alumina substrates was attributed to the thermal quenching/rapid or fast cooling process. Thus, from the results, we conclude that the film grown over the thermally quenched surface is not of sufficient quality to investigate the thermoelectric measurements. Therefore, we have focused the other alternative method, namely chemical etching for crystalline surface, as it removes impurity and disordered structure over the polished surface.

### 2.3.5 CCO films grown on chemically etched alumina substrates

#### Microstructure

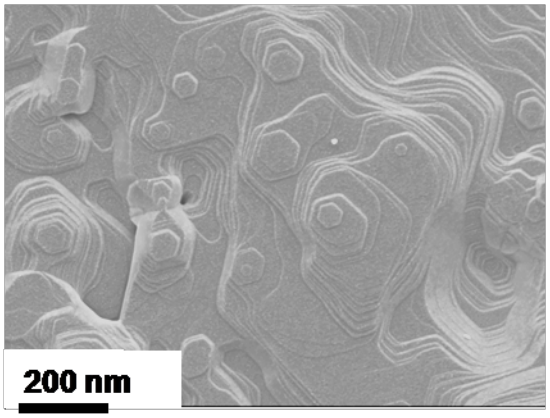


Figure 2.13: Micro-structure of film deposited over chemically etched alumina substrate sintered at 1700 °C.

The chemically etched surface described before, was used to deposit CCO films with thickness of 50 nm by PLD. The microstructure of the film shows less porosity and grows coherently over the surface suggesting a good epitaxial growth (see Figure 2.13).

**Epitaxial relationships by EBSD**

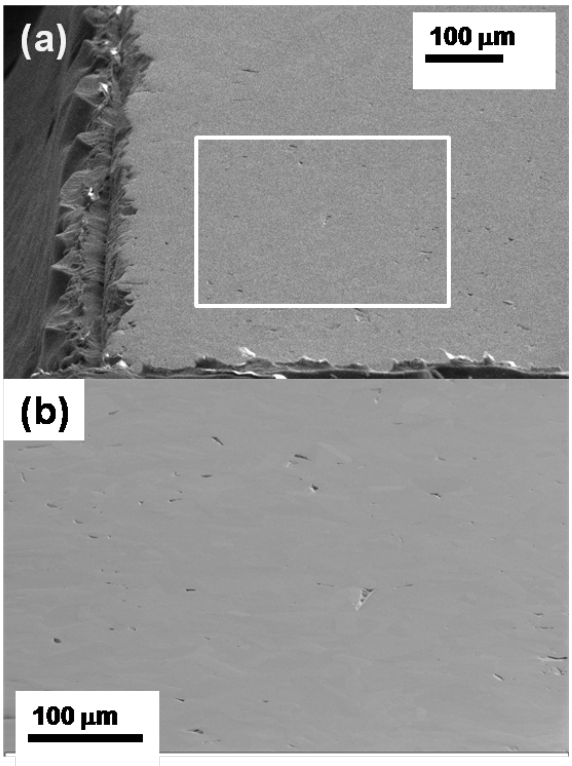


Figure 2.14: SEM image of (a): the region at the corner of $Al_2O_3$ substrate. White insert rectangle in (a) is magnified in (b).

EBSD was performed on both the surface of the CCO films, as well as the polycrystalline $Al_2O_3$ sintered at 1700 °C substrate in order to understand the nature of the surrounding grains, and its influence on the epitaxial relationships. The same region of $Al_2O_3$ surface was identified before and after the film growth to characterize the orientations of the grains by EBSD. The area near the corner was recorded using SEM under different magnifications to locate the scanned area of EBSD before growth (see Figure 2.14). The SEM micrographs were recorded with noting this magnification, working distance and aperture size. Then, EBSD scan was performed over the same area of after the film growth.

The grain orientation map of the $Al_2O_3$ ceramic substrate is shown in Figure 2.15(a) as an inverse pole figure (IPF), along with the appropriate color-coded stereographic triangle for a trigonal system (see Figure 2.15(b)).

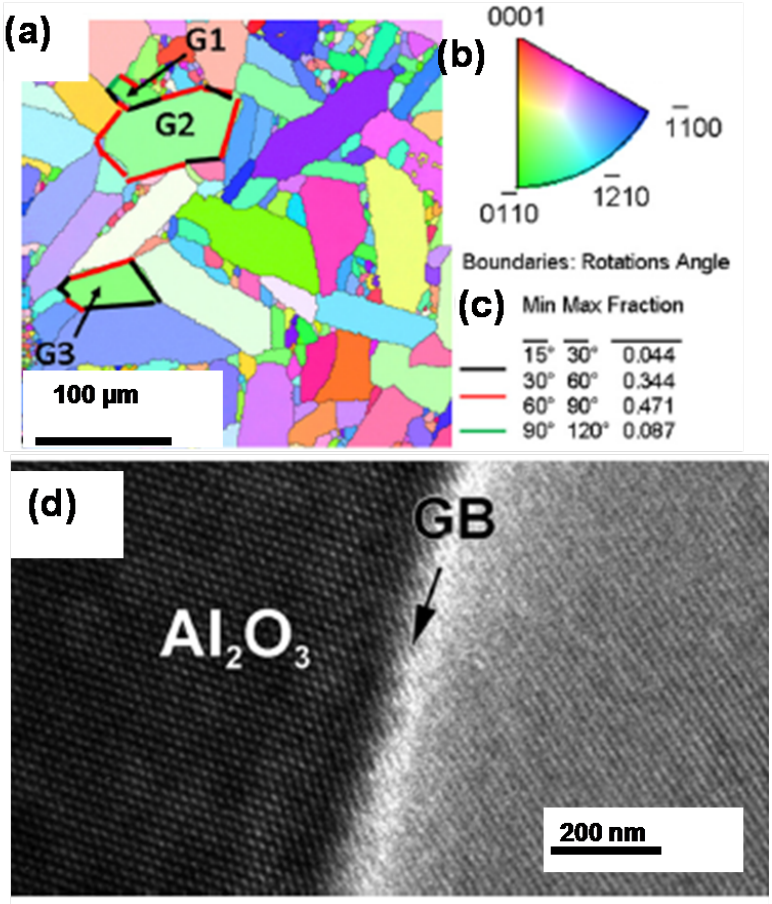


Figure 2.15: (a) 300x300 $\mu m^2$ Inverse Pole Figure (IPF) of $Al_2O_3$ substrate which gives the crystallographic orientations orthogonal to sample surface. Regions with low confidence in the indexing (<0.1) have been removed. The orientation map included some boundaries that have been highlighted. White lines: subgrain boundaries with the very small misorientation angles (15-30°); black lines: subgrain boundaries with the small misorientation angles (30-60°); red lines: grain boundaries with the large misorientation angles (60-90°); green lines: grain boundaries with the large misorientation angles (90-120°). The representation of the colour code (b) used to identify the crystallographic orientations on standard stereographic projection is also indicated (red: [0001]; blue: $[1\bar{1}00]$; green: $[0\bar{1}10]$). The number of fractions of boundaries with different misorientation angles is reported in the table (c). (d) HRTEM bright field micrograph of $Al_2O_3$ GB as marked by arrow.

The patterns of $Al_2O_3$ substrate were indexed as a trigonal system with the lattice parameters of ($a$=4.785 Å and $c$=12.991 Å , (ICSD file No.169720). In this plot, grains

with low confidence index (below 0.1) were not considered. The average image quality was IQ=1224, which confirms high crystallinity of the grains and the near surface regions. The misorientation distribution values across the grain boundaries ranged from 15° to 120°, and the relative fraction of the boundaries in the different ranges of misorientation angle are given in Figure 2.15(c). The majority of the grain boundaries are high angle boundaries, in the range of 30° to 60°. The crystalline quality of $Al_2O_3$ grains and grain boundaries were investigated by TEM. A typical high-resolution TEM image of a grain boundary is shown in Figure 2.15(d). The two grains are highly crystalline and the boundary is sharp and well-distinguished.

EBSD patterns of the marked grains as G1, G2, and G3 (see Figure 15(a)) are shown in Figure 16, both for the substrate before deposition (Figures 2.16(a), 2.16(c), and 2.16(e)) and for the film after deposition (Figures 2.16(b), 2.16(d), and 2.16(f)). Clear contrasts were seen in the EBSD patterns for all the cases, though the patterns are more diffuse for the film (as reported previously), [82] resulting from the internal strains of the film introduced by the epitaxial growth on the underlying grain [83].

Using the automated procedure, the grain orientations of 1, 2, and 3 of $Al_2O_3$ can be assigned from the detected zone axis of $[01\bar{1}\bar{1}]$, $[\bar{2}021]$, and $[\bar{1}\bar{1}20]$ respectively [84]. The three-fold symmetry axis confirms the trigonal crystal lattice [37]. Indexing of CCO films is more complicated, since it belongs to the category of misfit-layered oxide materials and it consists of two monoclinic subsystems with an similar $a$, $c$ parameters and different $b$ parameters [55]. Thus, the backscatter diffraction pattern of the CCO is expected to be superposition of those two subsystems and it is difficult to be interpreted [85]. So, we considered a simple monoclinic system with the lattice parameters ($a$=4.834 Å , $b$=4.558 Å and $c$=10.844 Å and $\alpha, \beta, \gamma = 90, 98.141, 90°$) for the analysis. It has to be noted that the $b_2$ parameter of the rock salt-type sub-system was used as a $b$ axis, as suggested in the previous report [85]. The CCO grains of, G1, G2, and G3, are indexed with the [407], [42 15], and [11 $\bar{3}$4], respectively [75].

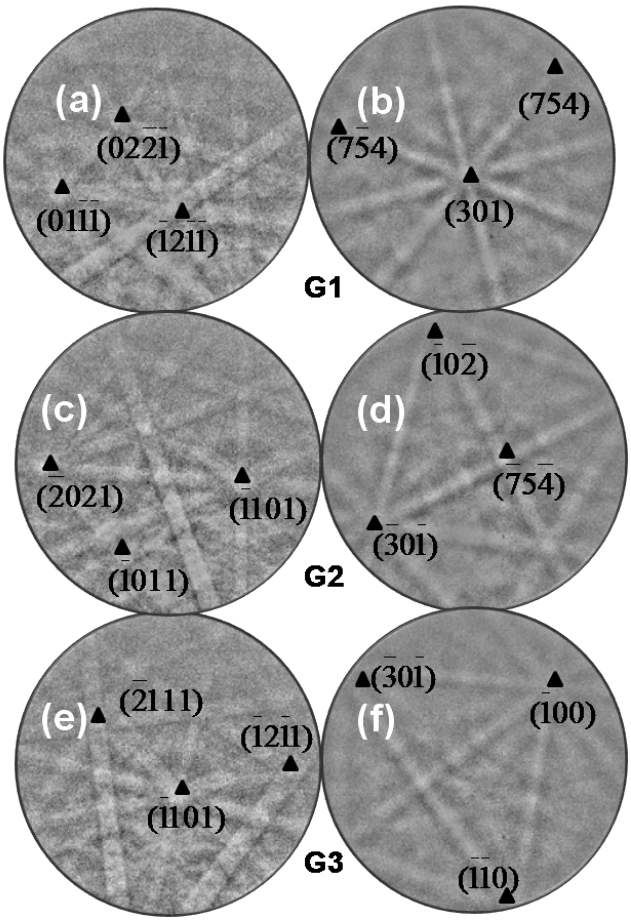


Figure 2.16: EBSD patterns for the $Al_2O_3$ substrate and CCO films for several grains (G1, G2, and G3, see Fig. 1). (a), (c), and (d) refer to the $Al_2O_3$ substrate. (b), (d), and (f) refer to CCO films. Substrate (film) Euler angles are: G1-235.6 (296.1), 105.9 (19.8), 9.9 (77.3); G2-101.3 (99.9), 70.2 (170.8), 283.2 (296.9); G3-86 (178.1), 72.7 (104.8), 285.9 (286.9).

The relative orientation to the crystal, obtained from EBSD patterns, can also be represented with three Euler angles (these are given for each image in the caption of Figure 2.16).

We quantitatively investigated the crystallographic orientation of the films relative to the $Al_2O_3$ substrate by comparing the location of the (001) pole for both film and $Al_2O_3$ substrate. These pole figures are given in Fig. 2.17((a) for the substrate grains and (b)

for the film grains).

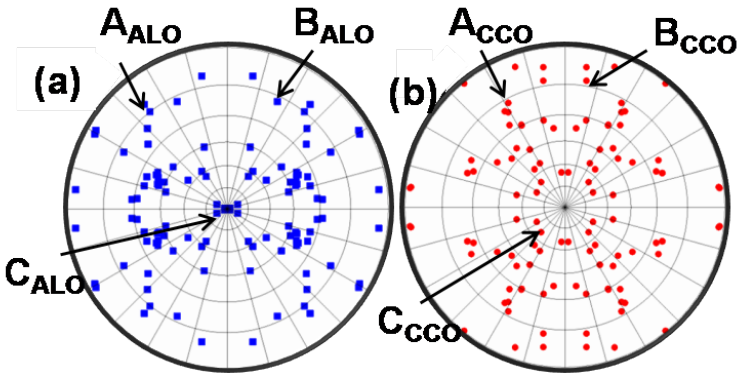


Figure 2.17: Grain texture of film and polycrystalline ceramic represents in <001> pole figure. (a) $Al_2O_3$ polycrystalline substrate before deposition, (b) CCO film. The angle of grains labelled A, B and C with respect to the center of the pole is 79.21, 29.82 and 9.2°, for $Al_2O_3$ and 73.12, 77.57 and 22.94° for CCO. The center of the figure is the normal direction. Concentric circles are scaled every 15°.

The orientation recorded from 56 randomly selected grains are shown. One observes that the poles are well-distributed in angular space for both the film and the substrate. When comparing the relative location of the (001) pole for a given film grains on a specific substrate grains, we determine an average of 5° between the *c*-axis of $Al_2O_3$ and the *c*-axis of CCO. This overlap between the pole points confirms that the [0001] and [001] directions of $Al_2O_3$ and CCO, respectively, are essentially parallel. The rotation of 5° between the film and the substrate results from a combination of experimental errors in the orientation measurements, and a misalignment of the sample during the two measurements, as observed previously [82]. Essentially, this argues that local texture does not develop in the samples along the *c*-axis to orient itself normal to the growth direction, as observed previously, but owing to a preference of the epitaxial arrangement of the two crystal lattices upon one another, during growth-regardless of the absolute orientation of the grain. This is similar to what has been observed for $TiO_2$ growth on perovskite $BiFeO_3$ [26, 82].

**Structural resolution by TEM.**

In order to get more information about crystal defect structure and texture of the CCO film, TEM was also performed. The information on quality of the grain boundaries (GB), film/substrate interface, and its epitaxial relationships are also extremely important. Figure 2.18(a) shows the cross-section of low-magnification TEM micrograph of *c*-axis oriented CCO film grown on top of GB of $Al_2O_3$ substrate, and its corresponding Electron Diffraction (ED) pattern.

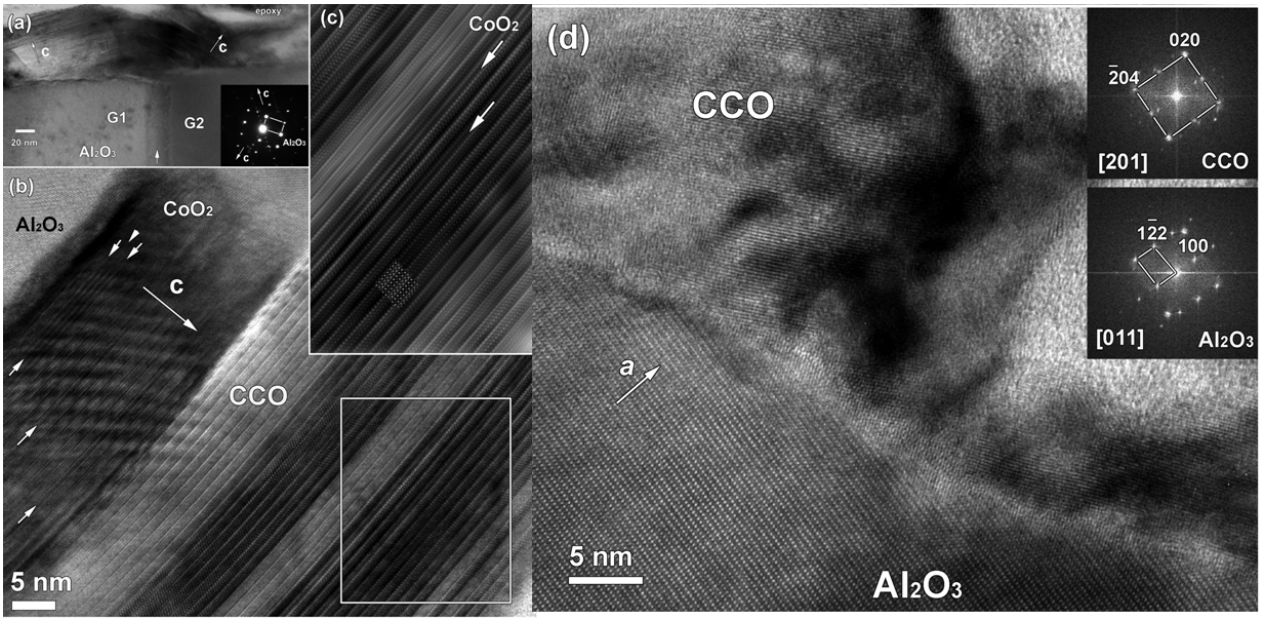


Figure 2.18: (a) Low magnification cross-section bright-field TEM micrograph of CCO film grown on $Al_2O_3$ polycrystalline substrate showing the interface region between the first and second c-axis orientation of CCO film across the grain boundary. The corresponding ED pattern is given as insert. The GB between two grains of $Al_2O_3$ is marked with white arrow. (b) HRTEM micrograph of c-axis oriented CCO film along [110] zone axis and (c) enlargement of selected in (b) with white box area together with simulated image ($\Delta f = -70nm, t = 6nm$) given as insert. The $CoO_2$ stacking faults are indicated by white arrows. (d) HRTEM micrograph of $Al_2O_3$/CCO interface and corresponding FT patterns taken from interface (bottom) and CCO grain only (top one). Note the absence of amorphous layer at the interface or the absence of secondary phase.

The surface of the CCO film is not flat enough. The "wave-like" surface originates from the tilt of c-axis with respect to the substrate when film grows across the GB of

$Al_2O_3$ substrate. ED pattern shows the superposition of the electron diffraction pattern of substrate (white rectangle) and of the film, and shows two rotated c-axis corresponding to the tilted c-oriented grains. The presence of internal references in the ED pattern as $Al_2O_3$ substrate, allows to measure lattice parameters of $c$-axis of CCO with high accuracy of $c$=10.78 Å , and is in a reasonable agreement with reported in the single crystal 10.83 Å and for the thin films [55,68,86,87].

The HRTEM study of the film further confirms the CCO structure as shown in Figure 2.18(b). Bright contrast bands are clearly visible along $c$-axis which are certainly due to small tilting of the [110] zone axis. The micrograph contains few $CoO_2$ stacking faults which are generally observed in CCO films. Image simulation of CCO structure ( inset of Figure 2.18(c)), based on the monoclinic CCO (space group of C2/m with $a$=4.8376 Å , $b$=4.5565 Å , $c$=10.833 Å , and $\beta = 98.06°$) shows a good agreement with the experimentally observed micrograph [55]. The epitaxial growth of CCO on $Al_2O_3$ substrate is clearly seen using the cross-section HRTEM micrograph (Figure 2.18(d)) of film/ceramic interface taken along the $Al_2O_3$ zone axis of [011]. The Fourier transform (FT) pattern (inset in Figure 2.18(d)) shows the spots of $Al_2O_3$ along [011] and the spots of the CCO grains. The obtained FT pattern (upper corner inset in Figure 2.18(d)) is indexed based on CCO structure being grain oriented along $[201])_{CCO}$. Thus, the epitaxial relationships can be expressed as $[011]_{ALO}//[201]_{CCO}$; $[100]_{ALO}//[11\bar{2}]_{CCO}$; $[1\bar{2}2]_{ALO}//[\bar{1}12]_{CCO}$.

Further, HRTEM micrograph of the CCO film grown over the $Al_2O_3$ polycrystalline substrate were recorded (see Figure 2.19(a)) and shows that the films are grown epitaxially, and uniformly along the $c$-axis over the entire substrate. The as-grown film seems to be tilted along the step terrace as highlighted in white box (see Figure 2.19(b)). This tilt occurs probably due to the stress in post-coalescence of the film [88,89]. Such an influence can lead to $CoO_2$ stacking faults (see enlarged image across surface given as right insert). Moreover, the effect of grain size, grain boundary and misorientation between the grain can also influence the structure of the film.

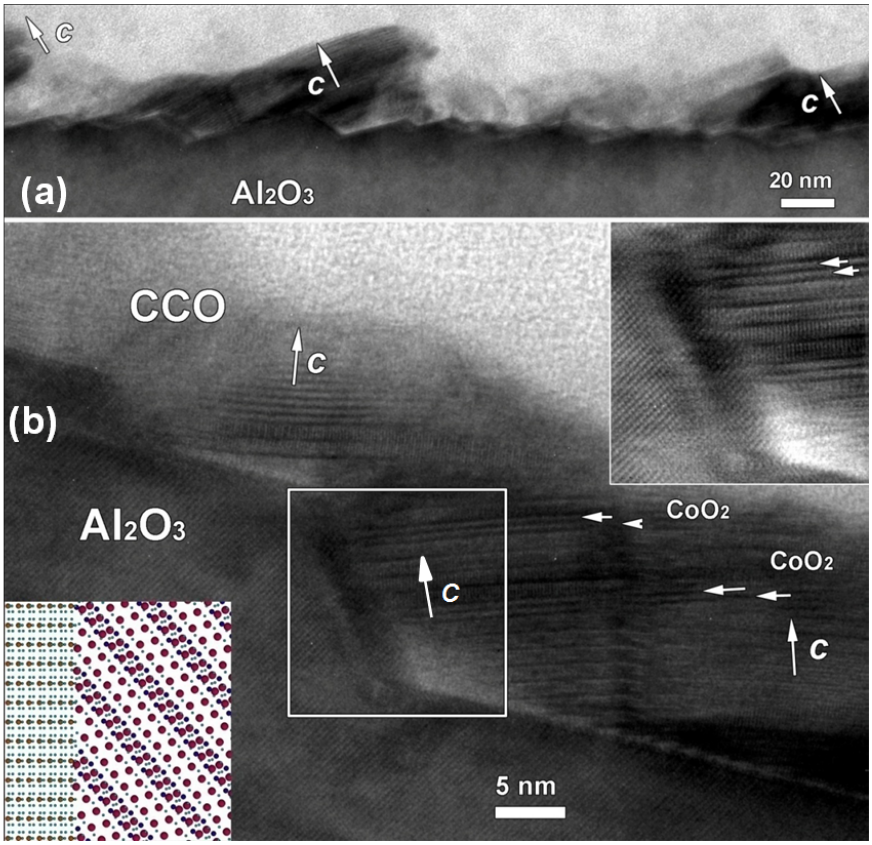


Figure 2.19: (a) Low magnification cross-section bright-field TEM micrograph of CCO film grown on $Al_2O_3$ polycrystalline substrate showing the film grown along *c*-axis on the terrace region of the substrate. (b) The magnified HRTEM micrograph of inteface region with step terrace in (a) is shown. The $CoO_2$ stacking faults are indicated by white arrows. The enlargement of selected across the step terrace with white box area (given as insert in top right) and corresponding schematic image (given as insert in bottom left). Note the absence of amorphous layer at the interface or the absence of secondary phase.

In this HRTEM study (see Figure 2.18(d) and 2.19(b)), it is important to notice that no secondary phase or amorphous layer were observed at the interface. This is very different from the previous TEM analysis of CCO thin films grown on single crystal sapphire (001)-oriented, glass or (100)-silicon where the presence of both secondary phase and low-crystallinity structures at the interface has been reported [90–92]. In our present study, the absence of amorphous layer close to the interface clearly confirmed the good texture and the epitaxial nature of the CCO thin film with respect to each grain, and will be discussed hereafter with the thermoelectric properties. The films growth is achieved without the

*classical* substrate-induced epitaxy coming from the single-crystal substrate. It further suggested that each 10 $\mu$m grain of $Al_2O_3$ acts differently on the stress and texture of CCO films comparing to a larger single crystal substrate of few mm. The combined analysis of TEM and EBSD shows indeed the collective and cooperative influence of the nature of the alumina template, being either a polycrystalline substrate (with multiple grains) or a single-crystal substrate, on the nucleation of the CCO film.

### 2.3.6 Thermoelectric Measurements

The temperature-dependence of the Seebeck coefficient and the resistivity are shown on Figure 2.20.

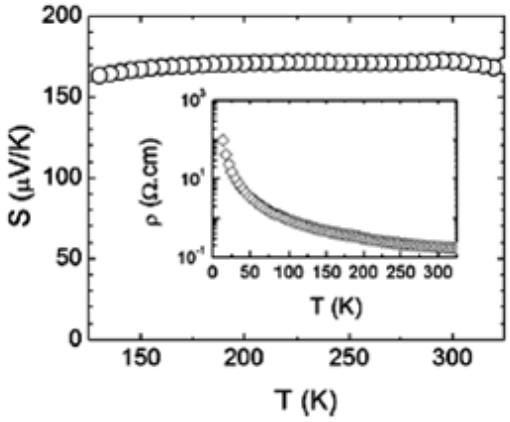


Figure 2.20: Temperature-dependence of the Seebeck coefficient and resistivity (insert).

Contrary to the single crystals or polycrystals of CCO, [55,93] the resistivity is close to 100 Ω.cm at 300 K, with a local activation energy d(ln$\rho$/d(1/T) increasing from 50 meV at low temperature to 300 meV at 300K. The film resistivity increases dramatically below 150 K (see insert of Figure 18), and the activation energy is calculated to be 25.2 meV. Note that the resitivity becomes too high at low temperature for an accurate measurement of the thermoelectric power. From 150 K to 300 K, the film presents a constant value of Seebeck close to 170 $\mu$V/K. As seen in the bulk, the positive value indicates hole-like carriers, and the shape of $S(T)$ is typical of CCO, with a plateau observed for T $>$ 100-200K, which follows a steep increase of $S$ at low temperature (which can not be observed here due to the large value of resistivity). However, the value of S (close to 170$\mu$V/K at

300 K) is surprisingly larger than for the bulk crystals (120 $\mu$V/K), [55] leading to a power factor, $S^2/\rho$, calculated to be 0.16 $mWm^{-1}K^{-2}$. In bulk misfits, an increase of Seebeck coefficient, associated to a more localized behaviour has also been observed. It can be due to a reduction of $Co^{4+}$ content, which can be in fact induced by oxygen non-stoichiometry and/or a modification of the misfit ratio $b1/b2$. The thermopower was found to vary between 125 and 160 $\mu$V/K, [93], and the resistivity becomes more and more localized as the formal $Co^{+4}$ concentration decreases.

A relatively large enhancement of the Seebeck coefficient reaching 178 $\mu$V/K at 300 K has also been observed in CCO samples when prepared using high magnetic field sintering compared with conventional sintering and SPS techniques. The authors attribute this larger enhancement to a better control of the oxygen non-stoichiometry at the grain boundaries and throughout the sample, associated to the special microstructure of their sample synthesized by a combined Spark Plasma Sintering and high magnetic field assisted grain alignment process [94].

In the case of thin films, while oxygen content is definitively crucial, substrate-induced strain can also be an important issue for the thermopower datas. Using the laser ablation technique, and very similar growth conditions, our group has already reported CCO thin films with Seebeck coefficients of 125 $\mu$V/K, a value close to the bulk [66]. A detailed investigation of the interplay between the substrate and the film which shows values larger than 125 $\mu$V/K, has also been performed using different kinds of substrates but most of the films present defects at interface and $CoO_2$ stacking faults [87] These stacking faults might indeed generate a spin state transition for $Co^{+4}$ (from low spin to intermediate spin state), which would increase the Seebeck coefficient up to 180 $\mu$V/K [95]. Here, the nanostructured thin film grown on polycrystalline $Al_2O_3$ substrate presents a large value of Seebeck of 170 $\mu$V/K. The absence of amorphous layer at the interface suggests the possibility of local strain engineering. Hall effect measurements performed at 300K on films prepared under similar conditions display a carrier density of $10^{18}cm^{-3}$ suggesting that the enhancement of Seebeck coefficient is mostly due to this small carrier concentration, in agreement with our resistivity values.

However, depending on the lattice and symmetry mismatch, defect-free growth of the hexagonal $CoO_2$ layer is stabilized only after a critical thickness and, in general, we

observe the formation of a stable $Ca_2CoO_3$ buffer layer near the substrate/film interface. Beyond this critical thickness, a large concentration of $CoO_2$ stacking faults is observed, possibly due to weak interlayer interaction in this layered material. We propose that these stacking faults have a significant impact on the Seebeck coefficient, and higher values in thinner CCO films due to additional phonon scattering sites are observed [87].

### 2.3.7 Main results

1. The dense polycrystalline alumina substrate were obtained at 1700 °C sintered by SPS.

2. From the characterization, high mechanical property, fine grained microstructure, texture of (0001) along $P_{SPS}$ and engineered grain boundary is observed.

3. The fine polished and chemically etched surface displayed good crystalline surface, which promotes good epitaxial growth. Amorphous layer of film or substrate surface were absent unlike in the case of thermally etched surfaces.

4. The effect of substrate surface structure, grain size, grain boundary and orientation and misorientation play an important role in the structure and surface morphology of the film.

5. The enhancement of Seebeck coefficient is attributed to the low carrier concentration.

6. The effect of polycrystalline substrate leads to nanostructuring and band engineering in addition to strain engineering.

## 2.4 Conclusion

In conclusion, nanostructured CCO thin films were deposited using pulsed laser deposition on textured $Al_2O_3$ polycrystalline templates prepared by spark plasma sintering.

Microstructure analysis reveals a good epitaxy of the film over chemically etched $Al_2O_3$ substrate , with a strong texture along the [001] direction. Electrical measurements show a maximum Seebeck coefficient of 170 $\mu$V/K at 300 K, higher than the bulk value. The enhancement is attributed to the nanostructured and band engineered film structure due to polycrystalline substrate. In a broad perspective, this approach can be further expanded to nanostructure the functionalized oxides for high performance thermoelectric films.

# Chapter 3

# $BiFeO_3/La_{0.7}Sr_{0.3}MnO_3$ heterostructures deposited on Spark Plasma Sintered $LaAlO_3$ Substrates

Multiferroic $BiFeO_3$ (BFO) / $La_{0.7}Sr_{0.3}MnO_3$ heterostructured thin films were grown on polished $LaAlO_3$ (LAO) polycrystalline substrates prepared by Spark Plasma Sintering (SPS). Both polycrystalline LAO substrates and BFO films were locally characterized using EBSD, which confirmed the high-quality local epitaxial growth on each substrate grain. Piezoforce microscopy was used to image and switch the piezo-domains, and the results are consistent with the relative orientation of the ferroelectric variants with the surface normal. These compounds are used to probe the local property of a material using CSE.

## 3.1 Introduction

Multiferroic - a material posses both ferroelectricity and magnetism, is a potential candidate for fundamental studies and technological applications like memories and sensors [96, 97]. In this chapter, the CSE approach was utilized to fabricate multiferroic $BiFeO_3$. $BiFeO_3$ is a perovskite structure, in which $Bi^{3+}$ ion occupies the corners of the rhombohedral lattice, $Fe^{3+}$ at the center of the lattice (see Figure 3.1).

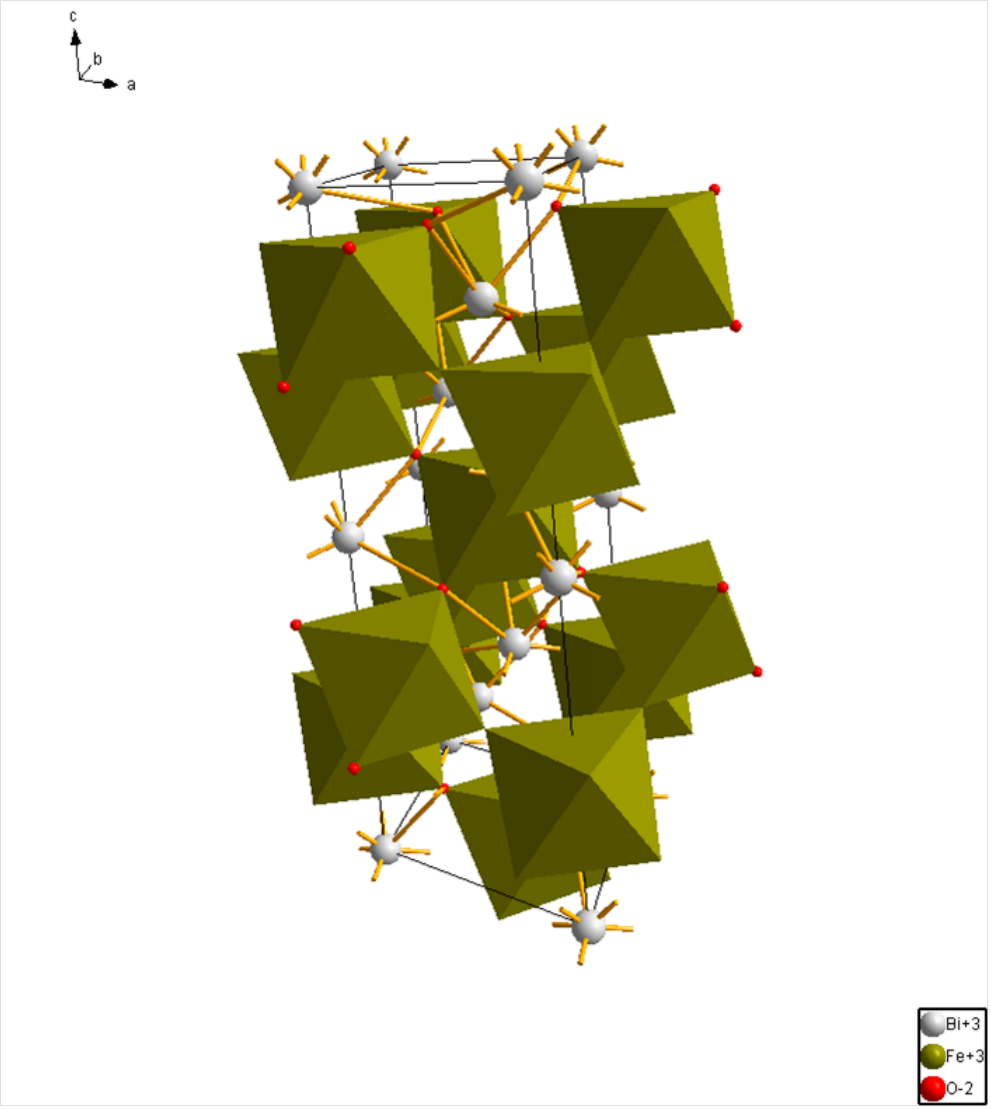


Figure 3.1: Crystal model of $BiFeO_3$.

$BiFeO_3$ has been one among the few naturally existing multiferroic materials that has been studied extensively in the past few decades, both in the form of bulk and thin films. In $BiFeO_3$, the proper ferroelectric origin arises due to the lattice instability. This is driven by covalent bonding of O-2p orbitals to the empty hybrid 6s-6p of Bi(III) ions as the primary polarization parameter and tilting of oxygen octahedra, which results in cooperative ferroic displacements through orbital ordering [3,98]. Moreover, the presence of G-Type antiferromagnetic spin order in addition to ferroelelectric nature is promising for multiferroic memory applications. Consequently, epitaxial $BiFeO_3$ films was under investigation for memory applications. The effects of the substrate-induced strains can strongly influence the mutiferroic property of an epitaxial film, because the orbital and

spin ordering of transition-metal oxides are highly sensitive to small perturbations such as lattice parameter, and pressure [99]. This is particularly true for $BiFeO_3$ compound where a R-like phase arises at moderate compressive strain whereas a T-like phase occurs at high compressive strain, with easy axis $[111]_{pc}$ and $[001]_{pc}$ (pc: pseudocubic), respectively [100, 101]. Interestingly, this strain-driven single or mixed phase of R or T-like phase in $BiFeO_3$ films tends to enhance the polarization and the magneto-electric coupling [102, 103]. The fine tuning of the out-of-plane remanent polarization for $[001]_{PC}$ $BiFeO_3$ film is possible from biaxial strain [104, 105]. Therefore, the strain-engineering can be effectively used to control the mutiferroic property of epitaxial $BiFeO_3$ films.

For practical applications, the ferroelectric domains are important, since the orientation (domain) states could be switched by the application of the electric fields. Also, certain domains (71°,109°) should be used for switching the [001]p $BiFeO_3$ films to realise a good magnetoelectric coupling [106, 107]. Thus, the nature of domain walls influences the polarization switching mechanism, and can further enhance magneto-electric coefficient [108]. Therefore, the orientation-dependence strain that induces the domains formation needs to be explored for a better understanding of switching characteristics of $BiFeO_3$ films. One of the solutions would be to synthesize the $BiFeO_3$ on a series of single-crystals with multitude of orientations. However, the commercially available oriented substrates seriously limits the scope of the study. As a result, we have utilized combinatorial substrate epitaxy that facilitate the growth of multi-oriented films.

Heterostructures of conducting $La_{0.7}Sr_{0.3}MnO_3$ (LSMO) and multiferroic $BiFeO_3$ (BFO) films were thus grown using pulsed laser deposition on polished polycrystalline $LaAlO_3$ (LAO) substrates, that were fabricated using SPS. Using similar heterostructures, the ferroelectric and magnetic properties of $BiFeO_3$ thin films have been widely studied on low-index orientations, such as (100), (110), and (111) single crystal perovskites, such as $LaAlO_3$, $NdGaO_3$, $SrTiO_3$, and $DyScO_3$. The properties of the films were dependent on both the orientation of the substrate and the strains [109–112]. Owing to the orientation dependent-properties observed on low-index single crystals, it is of great interest to observe the similar effects in $BiFeO_3$ grains deposited on polycrystals, which have both similar low-index orientations, as well as high index orientations. Here, the epitaxial relationships of BFO films on LAO are obtained using EBSD, while the local ferroelectric

properties of each grain are probed using PFM. We demonstrate that the local properties of $BiFeO_3$ films prepared using CSE are comparable to typical single crystal films.

## 3.2 Experimental

Equimolar amounts of undoped commercial $\alpha$-$Al_2O_3$ and $La_2O_3$ powders ($La_2O_3$, Aldrich and $Al_2O_3$, Cerac with 99.9 % purity) were weighted in stoichiometric ratio, mixed intimately and reacted in their solid states using different thermal treatments. The precursors were finally calcined 12h at 1200 °C to obtain the desired phase. Another step of intermediate grinding was done to obtain powders with homogeneous grain sizes. The resulting LAO powders of weight 5g, were sintered during 20 minutes at 1550°C under an uni-axial load of 50 MPa. The heating (cooling) rate is 100 °C per minute, with simultaneous increase (decrease) of the uniaxial load.

The LAO polycrystalline samples have typical dimensions of 5x2x0.5mm$^3$. The samples were first subjected to mechanical polishing to remove the scratches made by silicon carbide papers with roughness down to 10 $\mu$m for 2 hr. Then, the pellets were polished by an automatic machine using diamond liquid (DL) pastes with the grain size of 3 $\mu$m and 1 $\mu$m grain sizes, respectively, for about 2 min, in order to attain a mirror-like surface. Then, a solution of colloidal silica (CS) was used for 1 min as a final polishing step.

The heterostructures consisted of a 10 nm thick LSMO base layer and a 50 to 200 nm thick BFO top layer, where the LSMO served a metallic bottom contact for the piezoresponse force microscopy (PFM) analysis [113]. Both film layers were grown by pulsed laser deposition, using a KrF excimer laser (wavelength 248 nm) with a fluence of 1 J/cm$^2$ and a repetition rate of 2 Hz. For all depositions, the substrate temperature was kept at 700 °C under a 100 mTorr $O_2$ partial pressure.

Structural and microstructural characterization of the ceramics and films were carried out using electron backscatter diffraction (EBSD). The samples were mounted at a 70°-tilt angle from horizontal in a scanning electron microscope (FEG-SEM Carl ZEISS SUPRA 55)) operated at 20 kV. Gold was added along the edges of the samples to avoid charging effect on the surface during the experiments. Kikuchi patterns were recorded with a working distance of 10-15 mm and an aperture size of 60-120 $\mu$m, and indexed automati-

cally by the EDAX orientation imaging microscopy (OIM$^{TM}$) software (v.6). Automated EBSD scan was performed by scanning the surface of the sample with a beam step size of 0.3 $\mu$m. EBSD map was generated after several clean up methods, which attempts to clean-up the erroneous data (due to a pore, a grain boundary, an impurity at the surface that make a wrong indexation). To clean a map, several parameters must indeed be considered. Here, (i) the minimum grain size is set to 5 pixels, (ii) the minimum Confident Index to 0.1 and (iii) two neighboring points with a misorientation greater than 2° are considered to be the trace of a grain boundary. The average Confidence Index after this procedure of cleaning is larger than 0.1 for all the samples.

Ferroelectric properties using PFM under colloboration was performed by Dr M. Trassin during his Post-doc in the group of Prof. R.Ramesh at National Berkeley Laboratory(USA). Piezoelectric properties (PFM analysis) were characterized by an AFM-based setup (Veeco-DI, equipped with a Nanoscope IV controller) under ambient conditions using a commercial TiPt-coated silicon tip.

## 3.3 Results and Discussion

### 3.3.1 Pure phase of dense polycrystalline LAO

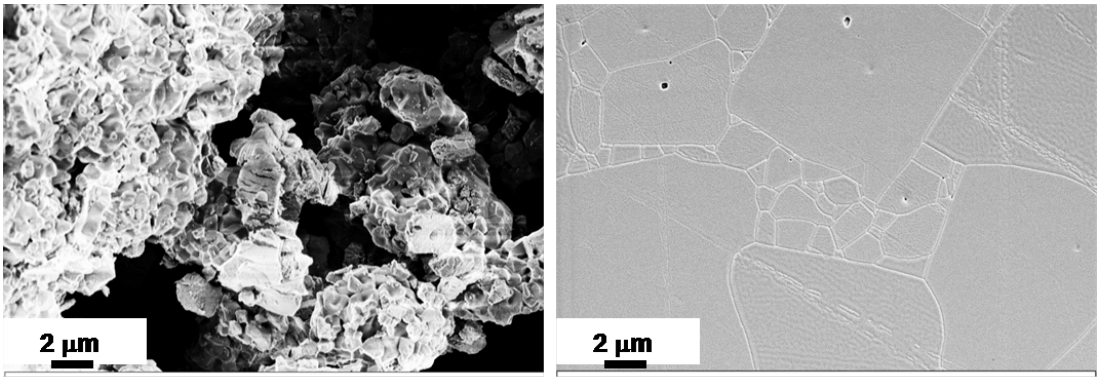


Figure 3.2: SEM image of LAO (a) as obtained powder and (b) LAO polycrystalline prepared by SPS.

LAO substrate has to be pure phase, dense and large grain size. In this regard, $LaAlO_3$ powder was synthesized by solid state route as described in experimental section. The powder comprises of agglomerated particles of average grain size 1 $\mu m$ and hexagonal shaped (see Figure 3.2(a)).

LAO powder was analysed by XRD for the phase purity (see Figure 3.3(a)). The XRD pattern do not show presence of impurity peaks. The Bragg's planes are well indexed with the standard LAO rhombohedral lattice with space group R3c. Further, Le Bail analysis was performed to confirm the rhombohedral lattice of space group R3C. From the analysis, the refined lattice parameters are ($a$=5.36012 Å , $b$=5.36412 Å , $c$=13.1047,Å and $\alpha, \beta, \gamma = 90, 90, 120°$), and are in reasonable agreement with the reported values of LAO [114]. This pure powder of LAO was consolidated by SPS as described in the experimental section to obtain high density of 99.9%. The thermally etched LAO substrate shows dense microstructure comprising of large, and small grain size (see Figure 3.2(b)).

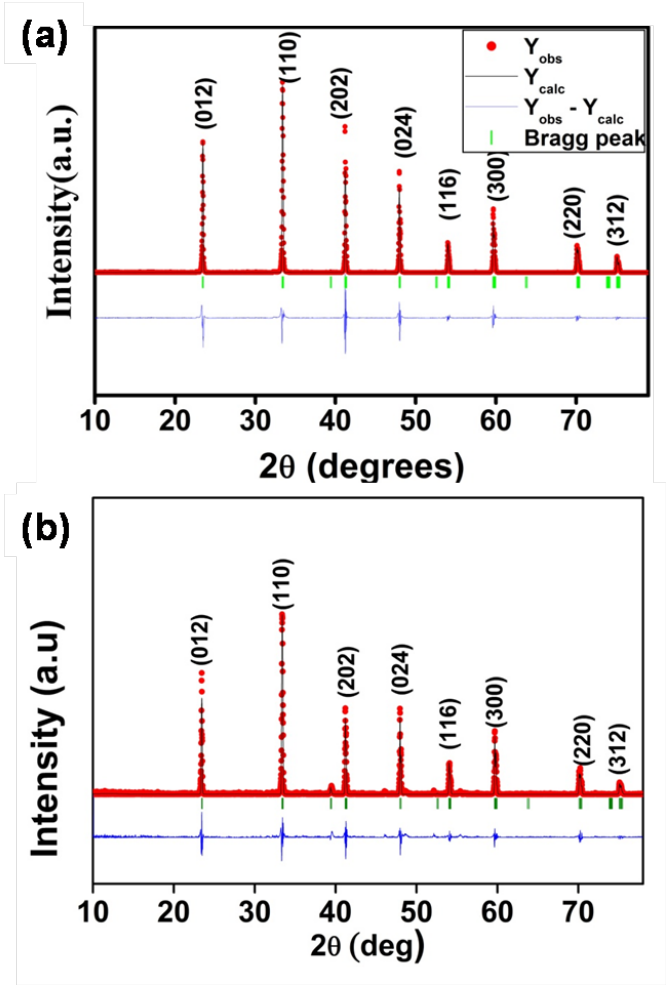


Figure 3.3: The measured and Le Bail refined XRD Bragg's pattern of (a) LAO powder and (b) LAO ceramic pellet. The legend shows observed diffraction intensity as $Y_{obs}$ and the calculated intensity from refined pattern as $Y_{cal}$. The Bragg's position are indicated in green vertical bars.

The large distributions in the grain size arises due to abnormal grain growth. This could be attributed to anisotropic grain boundary diffusion at high temperature. Further, the phase purity of dense LAO ceramic pellet was analysed by XRD (see Figure 3.3(b)). From the analysis, the calculated lattice parameters are ($a$=5.3647 Å , $b$=5.3647 Å and $c$=13.1103 Å and $\alpha, \beta, \gamma = 90, 90, 120°$) corresponding to a rhombohedral lattice with space group of R3c. This confirms that the obtained LAO polycrystalline crystallizes into a pure phase.

### 3.3.2 Fine polished and cleaned LAO polycrystalline surface

LAO polycrystalline were cut into small bars (5x2x0.5mm$^3$) with the surface plane parallel to SPS direction of uni-axial pressure. This ensures that the dense surface contains grain of random orientations for the study. The surface was fine polished and chemically etched in 5 % HF:$HNO_3$ solution for 9s, to remove the surface contaminants and release the strain generated during polishing. As a result, the surface appears to be flat and free from impurities (see SEM image in Figure 3.4).

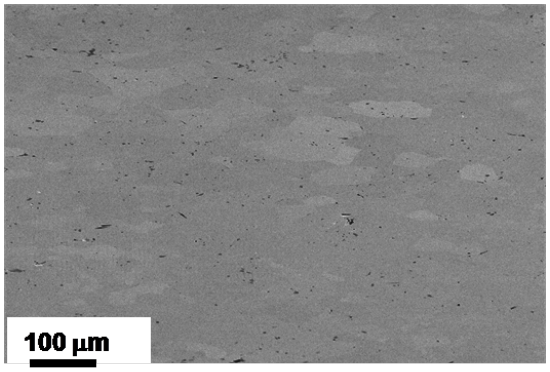


Figure 3.4: SEM image of LAO polished polycrystalline after chemical etching.

The quantitative investigation on such surface was carried out by AFM to obtain the topography image (see Figure 3.5).

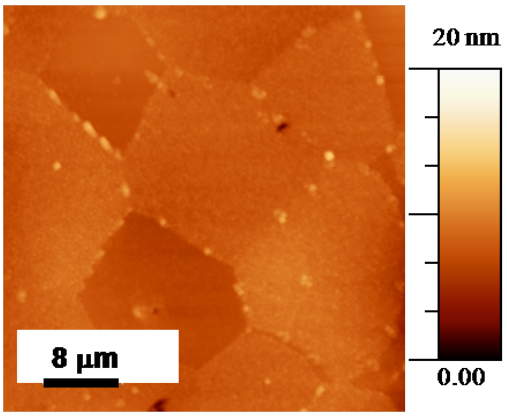


Figure 3.5: AFM image of LAO polycrystalline after chemical etching.

The surface microstructure are clearly seen with hexagonal shaped grains and free from scratches. The surface is highly uniform as it shows uniform contrast, but in specific each grain shows unique topography contrast. This could be attributed to an orientation

dependent polishing, and chemical etching rate that leads to different roughness of such grains. The average RMS roughness of grains are 5 nm. EBSD pattern was recorded over such surface to confirm its crystalline quality (see Figure 3.6).

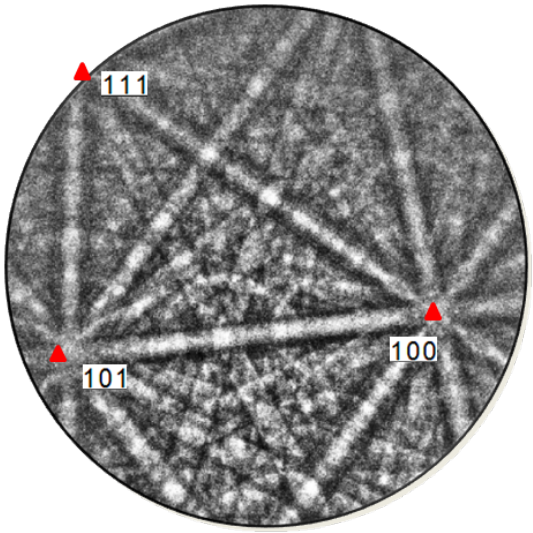


Figure 3.6: (a) Indexed EBSD pattern (CI=0.8, Fit=0.2°) of LAO substrate. The orientation with respect to the surface plane determined from the measured Euler angles in standard angle representation $(\varphi_1, \phi, \varphi_2)$ is (18,75,51).

The obtained pattern shows intense line (IQ=4590), and band edges are clear. This sharp band edges indicates that the surface are not strained [75]. The pattern shown is indexed with space group of Pm-3m, and lattice parameter of 3.8 Å for the LAO substrate [115]. Since most of the reported work assume LAO substrate as pseudo cubic lattice.

### 3.3.3 Epitaxial relationship between films and LAO substrate.

#### EBSD scan over the same region of substrate and film

LAO surface was marked in order to identify the same region before and after the film growth to determine the epitaxial relationship and to perform PFM scan in the same region, since a correlation between the orientation and the ferroelectric properties is expected. For that, the surface was marked by using cutting machine (see Figure 3.7).

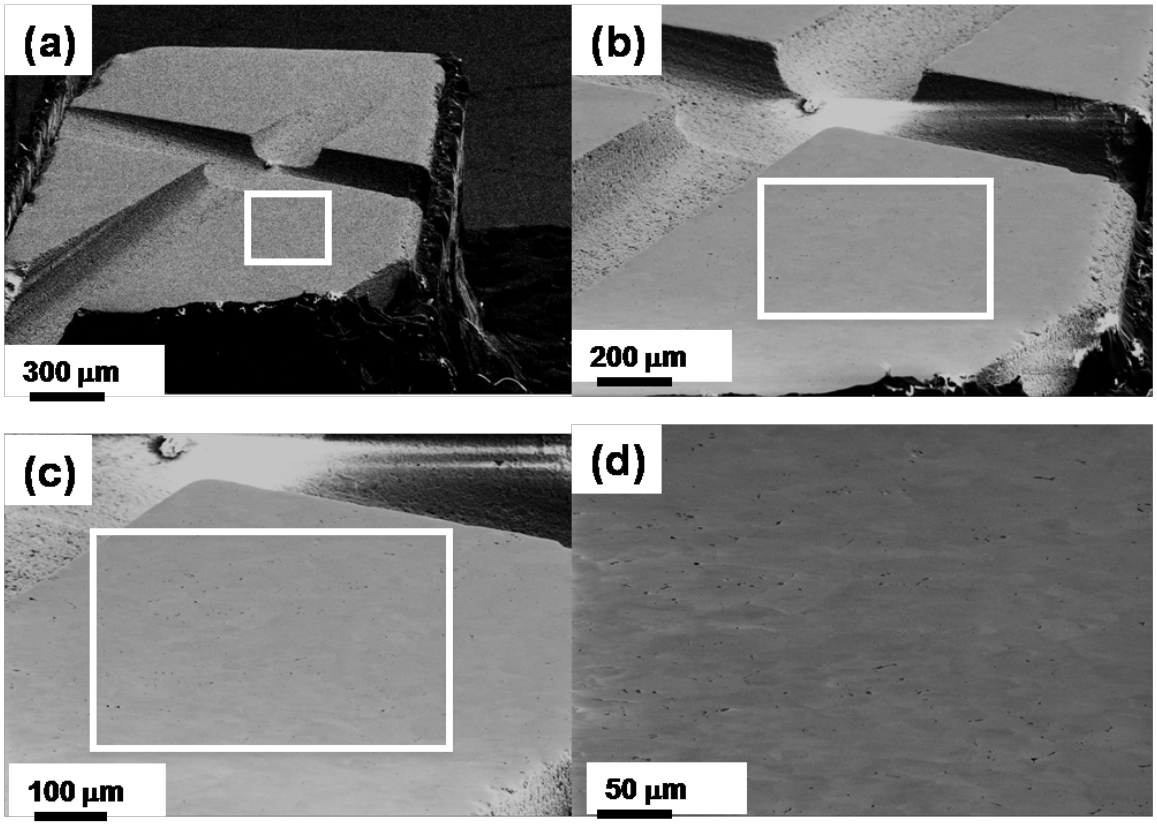


Figure 3.7: SEM image showing (a) the marked region over the LAO substrate. The marked white rectangle in (a) is magnified by SEM to record (b) and (c). (d) Finally the marked region in (c) was used to perform EBSD scan.

The SEM images were recorded under different magnifications to locate the area near the cross, before the film growth to perform. The recorded SEM images contain information regarding magnification, working distance and aperture size. Then, EBSD scan was performed on the same region after the film growth using the recorded SEM images. This informations were also used to perform PFM analysis.

Automatic EBSD scans were performed over the same region of the marked LAO substrate (see Figure 3.7(d)) before and after BFO film growth of thickness 100 nm (with an LSMO buffer layer). The inverse pole figures (IPFs) are obtained for the LAO substrate and the BFO film deposited on this substrate (see Figure 3.8(a) and (b)), respectively.

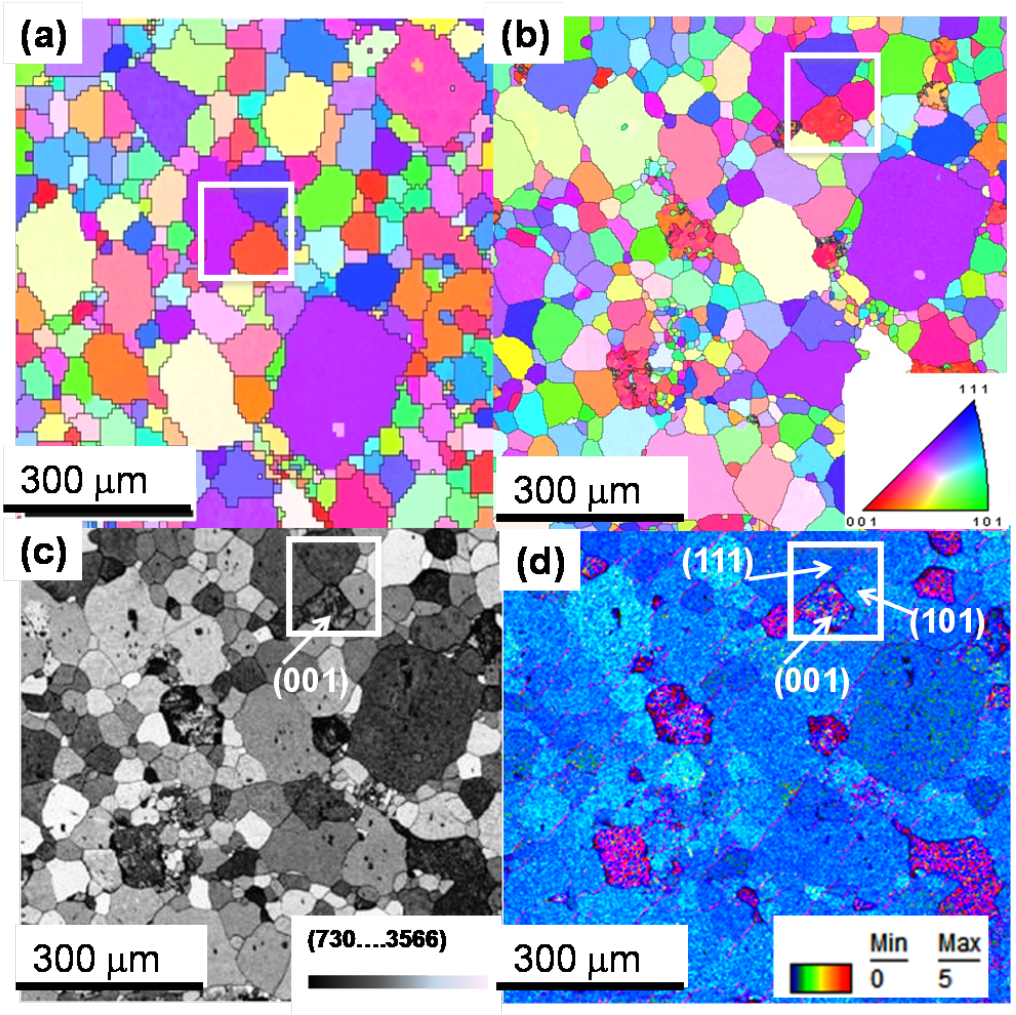


Figure 3.8: Inverse pole figure maps of (a) the LaAO substrate and (b) the BFO film and their corresponding colour code is given as insert. The white boxes indicate grains in the same region of substrate and film. The corresponding (c) map of the local misorientation angle relative to the average surface orientation of each grain and (d) grey scale image quality (IQ) map from the same film region. In (c), color legend of misorientation angle given as insert and (d) gray scale IQ given as insert.

The color coded IPF map (see Figure 3.8(b) insert) presents the crystal direction map illustrating all crystal directions that are parallel to a given viewing direction. The LAO substrate has a bimodal grain size distribution, with some very large grains $> 150\ \mu m$ and smaller grains ranging from 50-100 $\mu m$. The film grains have consistent assignments for the orientations within almost all grains of the substrate. The cleaned data exhibit grain sizes and grain boundary locations that are very similar in the two images, indicating that

both LSMO and BFO films grew in a grain-over-grain fashion on the LAO substrate. The average crystal direction (as assigned by the software) of each film grain is nearly identical to the crystal direction of the substrate grain on which it grew. Color variations between the film and substrate (see the purple/pink pair within the white boxes) are usually within a few degrees of each other in the color key shown in Figure 3.8(c), and small angular misorientations such as these have been observed previously in CSE grown films [28, 29] and are expected to relieve misfit strains in the heterostructures [116]. Further, orientation distributions (texture) of substrate and film are computed and represented in the form of IPF (see Figure 3.9).

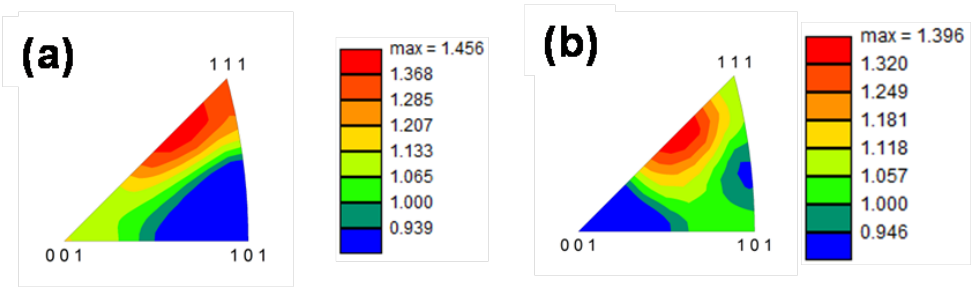


Figure 3.9: The orientations distributions of (a) LAO substrate and (b) BFO film with color code orientation densities (m.r.d) units.

The orientation density maxima obtained near the (111) and similar orientation distributions are obtained for film (see Figure 3.9(a)). Thus, the in-plane alignments between the substrate and grain exhibited identical characteristics with respect to the out-of-plane alignments. These observations indicate that the film epitaxy is dominated by local substrate-driven growth events that are consistent with each perovskite layer adopting a cube-on-cube epitaxial orientation relationship for nearly all grain orientations of the substrate.

### Misorientation and strain in BFO film

A typical EBSD pattern of BFO is presented in Figure 3.10.

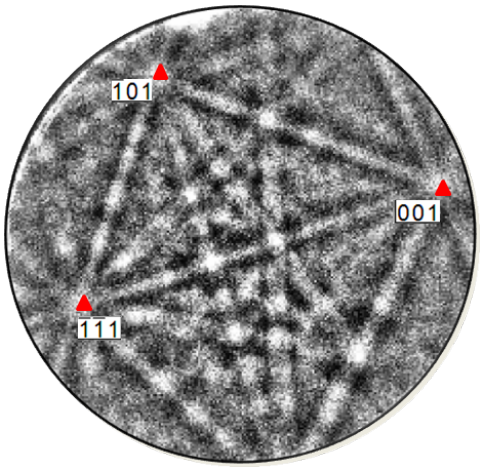


Figure 3.10: (a) The indexed EBSD pattern (CI=0.4, fit=0.4°) of BFO film. The orientation with respect to the surface plane determined from the measured Euler angles in standard angle representation $(\varphi_1, \phi, \varphi_2)$ is (146,34,284).

The bands of the $LaAlO_3$ substrate are sharp and intense (IQ=3680) (see Figure 3.6), but the $BiFeO_3$ film values are slightly more diffused than the substrate, which is attributed to local strains in the epitaxial films or the inhomogeneous strains in the film resulting from relaxation phenomena [27,28,117]. Nevertheless, all grains investigated display similar patterns with high image quality values, attesting a good crystalline quality, and confirming the epitaxial perovskite phase formation of the film. The local epitaxial quality was further confirmed by comparing the misorientation angle between the individual local orientations in a given grain to the average orientation of that grain (the average values were plotted in Figure 3.8(b)). A plot of this misorientation angle is shown in Figure 3.8(c) for the BFO film corresponding to the entire region in Figure 3.8(b). In the region , for most of the grains we found that the grain near (111) and (110) are indicated with white arrow in the highlighted white box (see Figure 3.8(c)), the misorientation angle is within 1°, in agreement with the expected values from epitaxial perovskite heterostructures. A similar analysis performed over many grains in the film indicates the majority of grains are of such quality, except for the (001) oriented film grains.

Film grown on LAO grains near (001) tends to result in the formation of small clusters that exhibit a local misorientation angle ranging from 3-5° on average (see Figure 3.8(c)). The IQ map shown in Figure 3.8(d) further highlights the multiple orientations within (001) grains (indicate in the highlighted white box). The IQ parameter is the integrated

intensity over all peaks in the Hough Transform, which reflects the quality of the local diffraction pattern and can be correlated to the phase, orientation, and strain in the diffraction volume [43]. IQ maps have high contrast between grains and where local orientation/strain variations exist, such as at grain boundaries. In Figure 3.8(d) (dark (light) regions are associated to low (high) image qualities). The IQ contrast varies in strong correlation with the regions of local misorientation observed in Figure 3.8(c) and 3.8(d). The (001) grains are non-homogeneous in colour, while (111) and (101) are homogeneous, similar to the films grown on higher index orientations. It is intriguing how uniform the vast majority of the BFO grains are in these heterostructures, and also that the BFO films on (001) grains have multiple orientations that vary in absolute orientation by about 5°, when indexed in the cubic system.

**Mixed BFO phase over (001) LAO substrate grains**

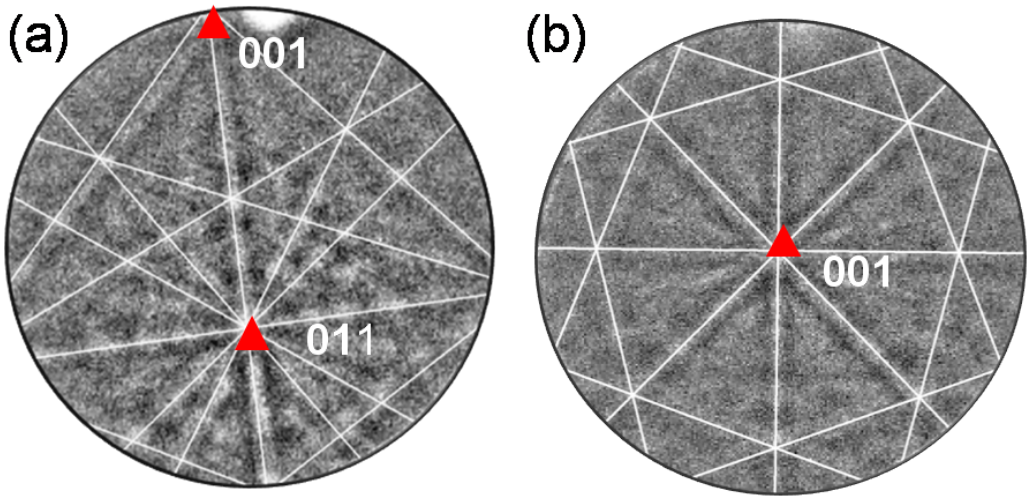


Figure 3.11: Two types of kikuchi patterns seen on (001) oriented grains of $BiFeO_3$ film with (a) : Rhombohedral symmetry and (b) : Tetragonal symmetry. The orientation with respect to the surface plane determined from the measured Euler angles in standard angle representation $(\varphi_1, \phi, \varphi_2)$ for High IQ and Low IQ regions are (40, 74, 285) and (89, 28, 315), respectively.

These observations indicate that one can investigate film growth on different orientations by exploring specific grains in a polycrystalline matrix, similar to what has been done extensively using single crystals [109]. To explore this further, EBSD patterns were

recorded from the two different kinds of regions observed in highlighted white box of Figure. 3.8(c) and 3.8(d) for the (001)-oriented grains. The EBSD pattern registered from the low misorientation (high IQ) region is shown in Figure 3.11(a). The Kikuchi pattern registered from the high misorientation (low IQ) region is shown in Figure 3.11(b), and it clearly differs from that shown in Figure 3.11(a). The C3 zone axis symmetry of (001) assigned in Figure 3.11(a) corresponds to rhombohedral phase. While C4 zone axis symmetry of (001) corresponds to tetragonal phase. Thus, we propose that this region is associated to the tetragonal (T)-like phase observed in BFO films on (001) pseudo-cubic substrates, [102] and this would explain the strong variation in assigned orientation and image quality observed in Figure 3.8. Similar patterns were always obtained for these two types of regions on grains near the (001), indicating the growth is uniform and that the mixed phase growth is a common feature in the BFO films, but only near (001).

**Orientation dependent ferroelectric contrast**

The epitaxial BFO heterostructure was investigated using Piezo Force Microscopy, in a similar fashion to BFO films grown on single crystals [109–111]. The grains highlighted in the white box in Figure 3.8(b) were first investigated. Figures 3.12(a) and 3.12(b) show the crystalline orientation from EBSD, where specific orientations and misorientation angles are marked, and the corresponding topography obtained by PFM, respectively. The topography changes from one grain to another, and the root-mean-square (RMS) roughness values range from 1 to 10 nm, depending on the grain. To further analyze the influence of the substrate grain orientation on the multiferroic thin film properties, the ferroelectric domains were imaged using PFM. Figures 3.12(c) and 3.12(d) show the out-of-plane (OP) and in-plane (IP) component of the PFM response, respectively. As the variation in PFM contrast shows, the ferroelectric architecture is clearly correlated with the underlying grain structure of the substrate, and changes dramatically exactly at the grain boundaries.

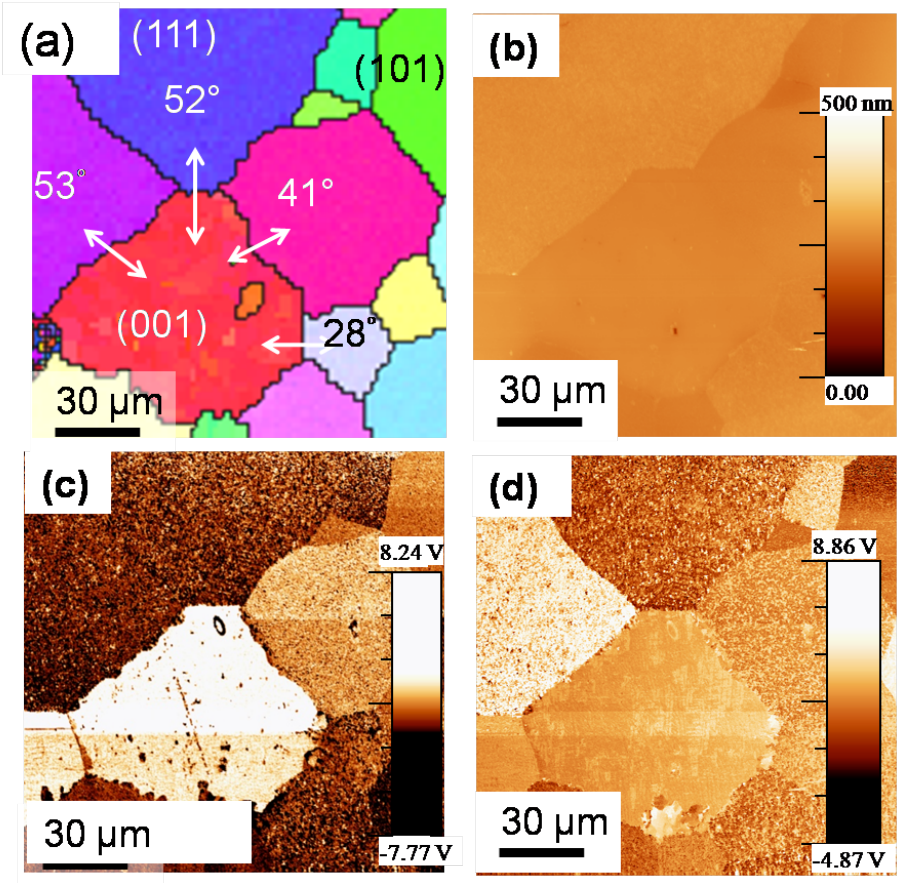


Figure 3.12: Enlarged mapping on $BiFeO_3$ (001)-oriented grain. (a) : EBSD colour code orientation map, (b) : PFM Topography, (c) : Out-of-plane PFM and (d) : In-plane PFM.

$BiFeO_3$ has been widely studied and now well established that (111) oriented films can have only two possible polarization directions, i.e. upwards or downwards [118]. For the considered grain, the out-of-plane component of the polarization is pointing upwards on the (111) oriented grains (darker contrast in Figure 3.12(c)) and downwards on the (001) oriented grain (white OP contrast in Figure 3.12(c)). The changes in the OP polarization component can be attributed to the different LSMO growth modes on the substrates, leading to different electrostatic environments for the ferroelectric layer, [119, 120]. Correspondingly, the in-plane (Figure 3.12(d)) polarization component reflects the underlying grain distribution and shows that all 4 possible BFO ferroelectric polarization variants are present (with dark, bright and no contrast for up, down and left/right polarization direction, respectively. We note that this large scanning area, showing different grains, allows for a qualitative analysis and no evidence for nanostructured domains.

### Ferroelectric Switching

To further probe the multiferroic properties of the film grown on the SPS prepared LAO substrates, we investigated the switching of ferroelectric domains. Figures 3.13(a-c) show the topography, out-of-plane PFM and in-plane PFM images, respectively, after the local application of a positive 12 V bias in the central 20x20 $\mu m^2$ region (that includes several grains and grain boundaries). A clear polarization reversal (comparing the central region to the outer regions) is observed in the OP image (see Figure 3.13(b)), as the PFM contrast is reversed.

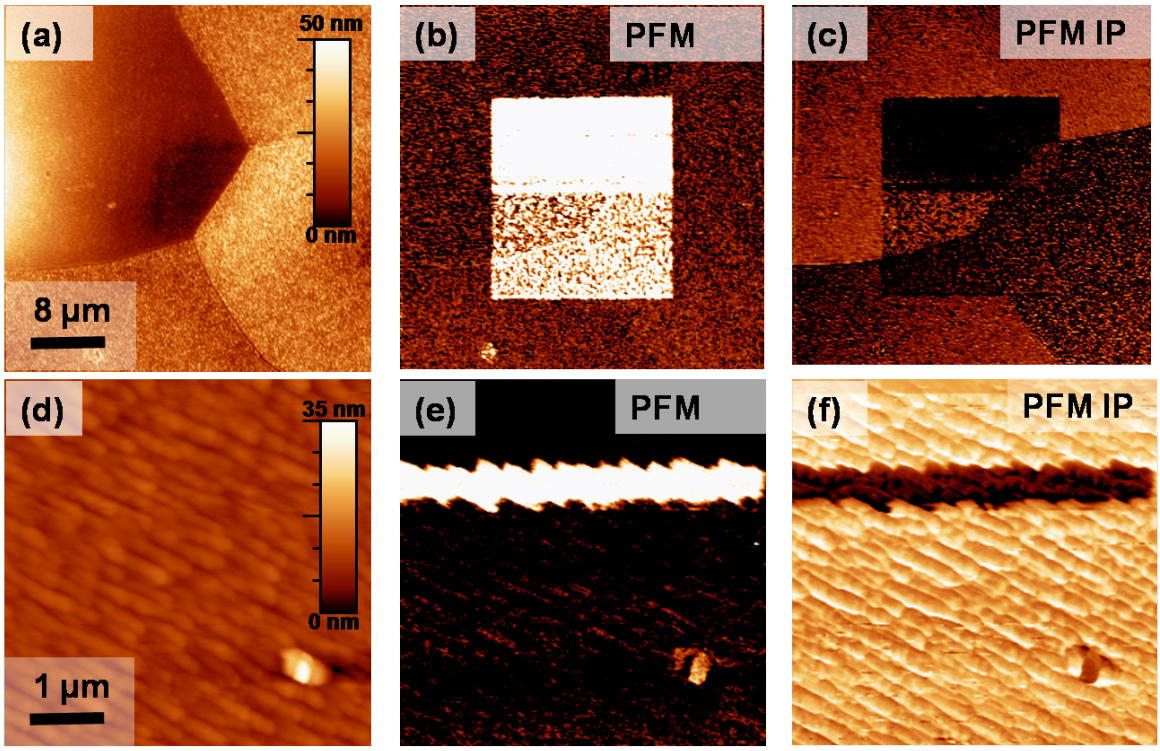


Figure 3.13: Poling measurements of $BiFeO_3$ films across triple junctions (a-c) and grain boundaries (d-f). (a) : PFM Topography, (b) : Out-of-plane ,(c) : In-plane, (d) : PFM Topography, (e) : Out-of-plane and (f) : In-plane. PFM contrasts were recorded after local application of a +12 V bias showing a 180 degree switching event.

The observed change in the out-of-plane contrast with a specific voltage polarity (inducing up to downward OP switching only in our configuration) further validate the interpretation of the direction of the OP polarization component. This demonstrates that the ferroelectric properties of BFO are maintained for many orientations in the heterostruc-

ture. The in-plane PFM contrast evidences the different local switching characteristics, as the contrast only reverses in some BFO films grown on specific grains. These different switching behaviors are due to the correlation between the allowed ferroelectric variants and the local grain orientation [118].

Further, to demonstrate the high-quality local ferroelectric properties, a (110)-oriented grain was selected and the BFO's ferroelectric polarization was switched using the PFM. The topography of this grain is shown in Figure 3.13(d), and the typical stripes expected from a (110)-oriented film are observed [118, 121]. In this configuration, only 180 degree switching events are possible using our tip bias value [122]. An horizontal 500 nm wide line was written in this grain using a + 12 V bias, and the OP and IP PFM images are shown in Figure 3.13(e) and 3.13(f), respectively. 180 degree switching was observed as both the OP and IP contrast reversed (the underlying stripe structure is attributed to the topography contribution), again demonstrating that the polycrystalline substrate grains are similar to microcrystalline single crystal surfaces, as the properties of the multiferroic heterostructures are similar to those expected from single crystals.

### 3.3.4 Effect of thickness on mixed BFO phase over (001) LAO substrate grains

The effect of thickness on BFO mixed phase growth on (001) substrate grain were investigated, and observations are presented below.

We demonstrate that the local properties of $BiFeO_3$ films prepared using CSE are comparable to typical single crystal films.

#### BFO film thickness of 50 nm

In order to study the effect of thickness on the formation of mixed BFO phase over (001) LAO substrate grains. The inverse pole figures (IPFs) are obtained for the LAO substrate and the BFO film deposited with thickness of 50 nm (see Figure 3.14(a) and (b)), respectively.

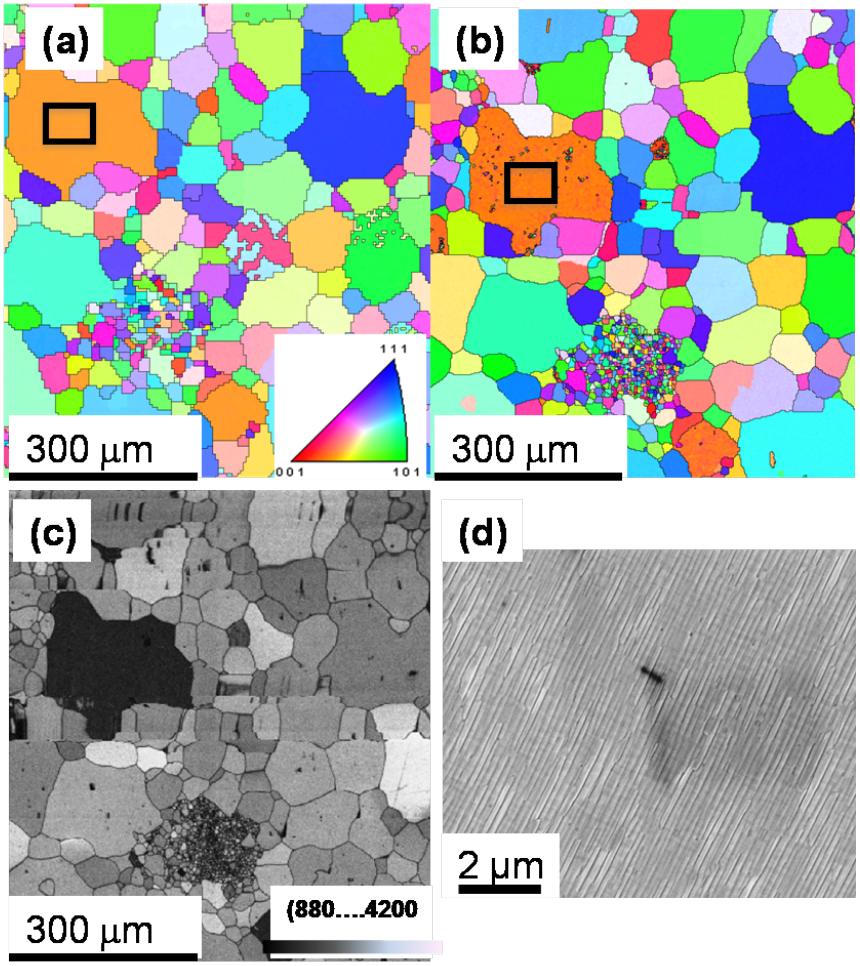


Figure 3.14: Inverse pole figure maps of (a) the LaAO substrate and (b) the BFO film and their corresponding colour code is given as insert. The white boxes indicate grains in the same region of substrate and film. The corresponding (c) grey scale image quality (IQ) map from the same film region. In (c), gray scale IQ given as insert. (d) SEM image recorded inside the black box of (b).

The film grows highly epitaxially and coherent over substrate grains, irrespective to the orientation. This is different from the BFO film with thickness of 100 nm. The substrate and the film with (001) oriented film grains are indicated by black box in Figure 3.14(a) and 3.14(b), respectively. This substrate and film grains have uniform orange color, which indicates the presence of pure phase, and not a mixed phase. Moreover, the image quality map (see Figure 3.14(c)) shows uniform contrast, but the presence of highly dark IQ color indicates that the film is highly strained. Over this region, SEM image was captured as shown in Figure 3.14(d) (recorded inside the black box of Figure 3.14(b)).

The SEM surface morphology appears like regularly arranged elongated stripes. This elongated morphology could be attributed to strained tetragonal phase since such phases are usually formed at lower thickness [102].

**BFO film thickness of 200 nm**

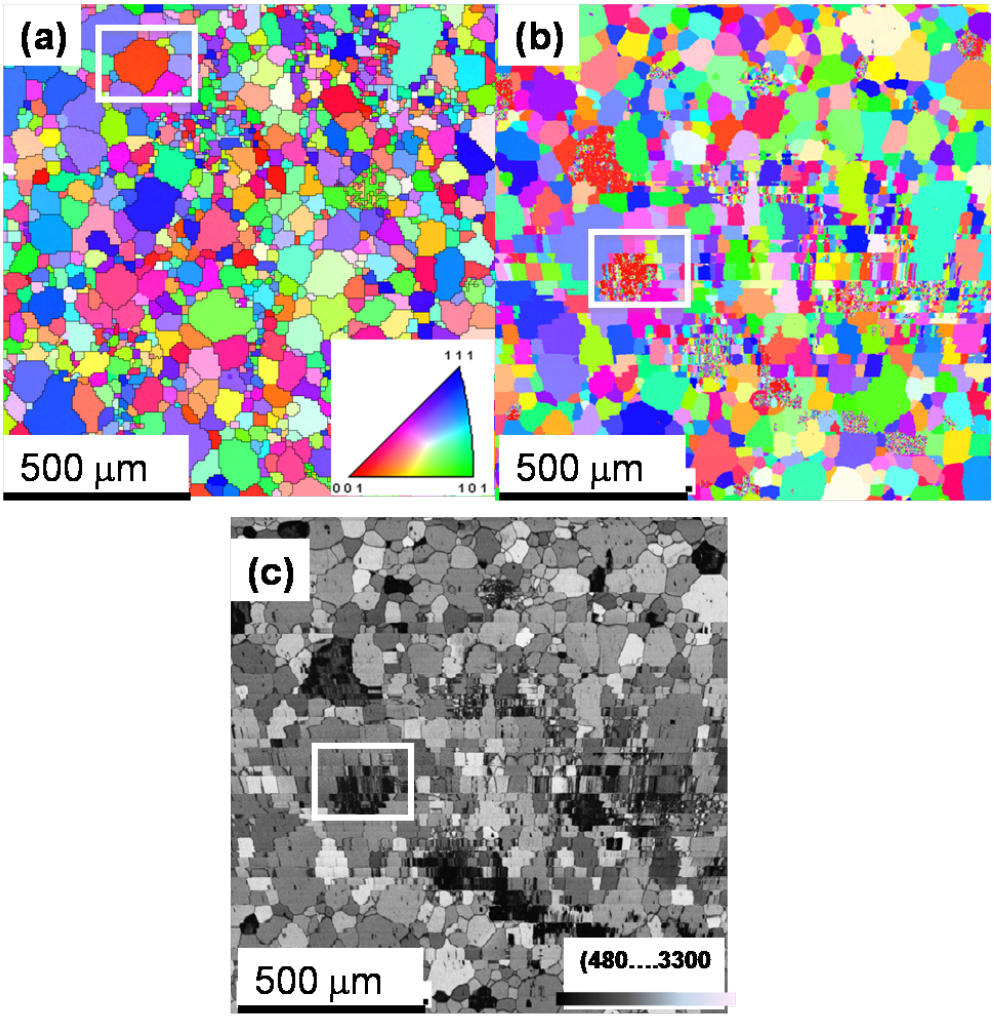


Figure 3.15: Inverse pole figure maps of (a) the LaAO substrate and (b) the BFO film and their corresponding colour code is given as insert. The white boxes indicate grains in the same region of substrate and film. The corresponding (c) grey scale image quality (IQ) map from the same film region. In (c), gray scale IQ is given as insert.

Further, the inverse pole figures (IPFs) are obtained for LAO substrate and BFO film with thickness of 200 nm (with an LSMO buffer layer) (see Figure 3.15(a) and (b)), respectively. The (001)-oriented substrate and film are highlighted by the white box in

Figures 3.15(a) and 3.15(b), respectively. The (001) film grains is extremely distorted due to charging in the EBSD scan. This charging could be attributed to the roughness of film. The (001) film grain highlighted by white box shows regions of different orientations since many colors are observed. This could be attributed to strained regions, which is further confirmed by the presence of low and high IQ corresponding to this grain (see Figure 3.15(c)).

PFM analysis were performed to study the influence of (001) film grain orientations on the ferroelectric domains. The recorded topography image changes from different regions. Figures 3.16(c) and 3.16(d) show the out-of-plane (OP) and in-plane (IP) components of the PFM response, respectively.

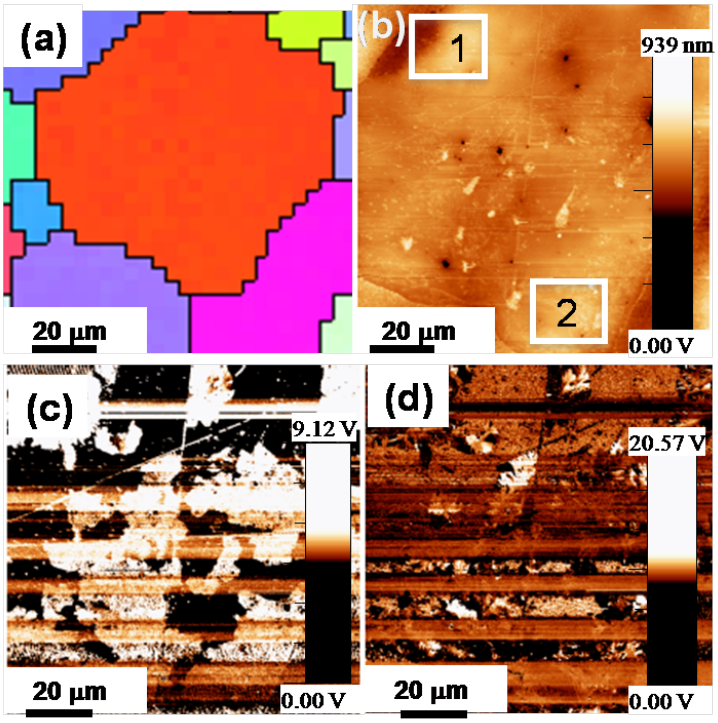


Figure 3.16: Enlarged mapping on $BiFeO_3$ (001)-oriented grain over the LAO substrate from Figure 3.14(a) indicated with white box). (a) : EBSD colour code orientation map, (b) : PFM Topography, (c) : Out-of-plane PFM and (d) : In-plane PFM.

In OP contrast, there is a mixture of bright and dark contrasts. Similar observations are made for IP contrast. In order to understand the contrasts, the well-resolved topography image in marked regions of Figure 3.17(a) was recorded.

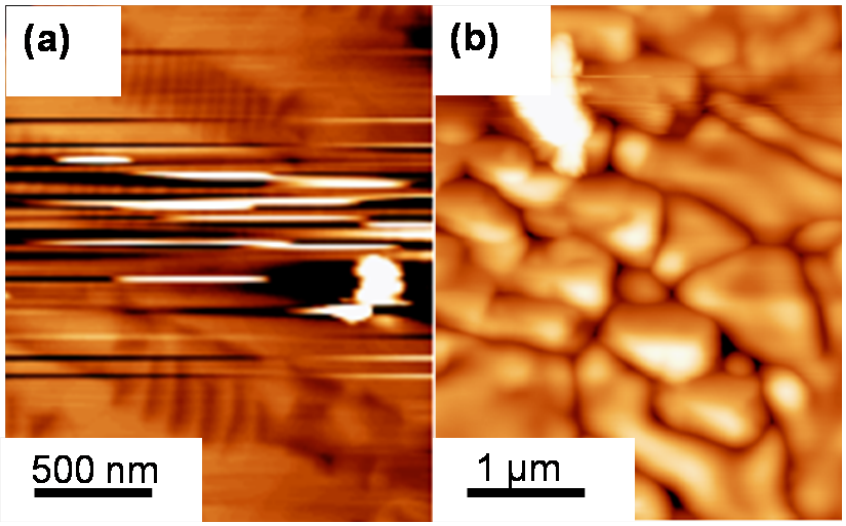


Figure 3.17: AFM topography image obtained over the marked regions of Figure 16(b) highlighted in white boxes corresponds to (a) 1 and (b) 2.

In the marked region 1, the characteristic striped region of R-like and T-like phase are seen. Note that R-like phase arises at moderate compressive strain whereas a T-like phase occurs at high compressive strain [100]. However, mixed phases are formed with increasing the thickness due to strain relaxation [102]. In marked region 2, such contrasts are not seen. Instead cluster of small grains appear (see Figure 3.17(b). This different topography arises from the post coalescence evolution of the grains leading to the morphology baptised as "inside bundling-outside grooving" [88] and reported recently in polycrystalline films. [89]. Therefore, the inhomogeneous contrast seen in the entire grain in both OP and IP contrast, is due to formation of mixed phases and regions with different topography.

### 3.3.5 Main results of chapter 3.

1. The chemically etched LAO substrate promotes highly epitaxial growth of BFO film of thickness 100 nm for all orientations of substrate grains. The presence of mixed BFO phases were observed over (001) substrate grain with misorientation angle 3-5°.

2. EBSD scan and PFM scan were performed over same region for the film, and confirmed the orientation dependence of the ferroelectric contrast.

3. Poling measurements were observed over grain boundary and junctions.

4. Effect of thickness on BFO mixed phase growth on (001) substrate grain were observed, similar to previous results on single crystals.

## 3.4 Conclusion

In summary, it was demonstrated structure-property relationships can be investigated for complex oxide ferroelectric heterostructures using the combinatorial substrate epitaxy approach, a high-throughput method for investigating the local epitaxy and properties of films deposited on polycrystalline substrates. High quality $BiFeO_3$ and $La_{0.7}Sr_{0.3}MnO_3$ thin film heterostructures were deposited by pulsed laser deposition on dense $LaAlO_3$ ceramics prepared by spark plasma sintering. The structural quality of the substrate and BFO films, as well as the epitaxial relationships of the films to the substrate, were determined locally using electron backscatter diffraction. For all but the (001) orientated substrate grains, the all perovskite heterostructure exhibited (so-called) cube-on-cube orientation relationships with misorientations between layers of less than 1°. On (001) oriented $LaAlO_3$ grains, the misorientation values were between 3-5°, and were attributed to the presence of two BFO phases. The presence and switchability of piezo-domains was evidenced using PFM, confirming that BFO films are ferroelectric when locally epitaxial on polycrystalline substrates. The effect of thickness on BFO film phase were observed over (001) LAO grain similar to film grown on single crystal. CSE approach can be useful to the epitaxial growth and structure-property relationships of multifunctional oxides with complex atomic structures, such as $GaFeO_3$ or $Gd_2Mn_2O_5$, for which isostructural substrates are not commercially available.

# Chapter 4

# Metastable monoclinic $Dy_2Ti_2O_7$ thin films

This chapter deals with the stabilization of monoclinic $Dy_2Ti_2O_7$ epitaxial films by CSE. To achieve this, we have first synthesized highly dense $La_2Ti_2O_7$(LTO) polycrystalline ceramic by conventional sintering. LTO ceramics are used after polishing and chemically etching as substrate to grow DTO films. Deposition temperatures of DTO films were optimized by analyzing the EBSD patterns. This film was found to be cubic phase as expected from the bulk. However, the formation of cubic and monoclinic DTO were observed on decreasing the thickness of DTO film. Such mixed phases are attributed to the roughness of the LTO substrate, probably a result of the chemical etching, which was confirmed by HRTEM studies. The 30 nm thick film grown on thermally etched LTO substrate was stabilized into metastable monoclinic DTO, as observed from EBSD and HRTEM analysis. Consequently, the use of CSE approach not only leads to the crystalline perfection of the epilayer but can also induce a transition from a cubic/pyrochlore in bulk to a monoclinic/layered-perovskite structure in this film, which is expected to be ferroelectric at room-temperature.

## 4.1 Introduction

This chapter deals with the fabrication of the metastable monoclinic $Dy_2Ti_2O_7$ thin films deposited on $La_2Ti_2O_7$ polycrystalline substrate. This system belongs to a layered-

perovskites having the general formula of $A_2B_2O_7$ ($A^{3+}$=lanthanide and $B^{4+}$=transition metal). Typical example is $Ln_2Ti_2O_7$ (Ln=lanthanide) structure, which belongs to a homologous series of the family of oxides with the general formula of $Ln_nTi_nO_{3n+1}$, where $n$ being the number of perovskite planes within a single layer. Their structure can be derived from the $ATiO_3$ perovskite structure by separating the layers of corner sharing $TiO_6$ octahedra along the [110] direction. They are known to have two different polymorphs in bulk, depending on the ratio between the radii (r) of $Ln^{3+}$ and $Ti^{4+}$ cations: either the pyrochlore structure or the layered perovskite phase (see Figure 4.1 and 4.2) [123–125].

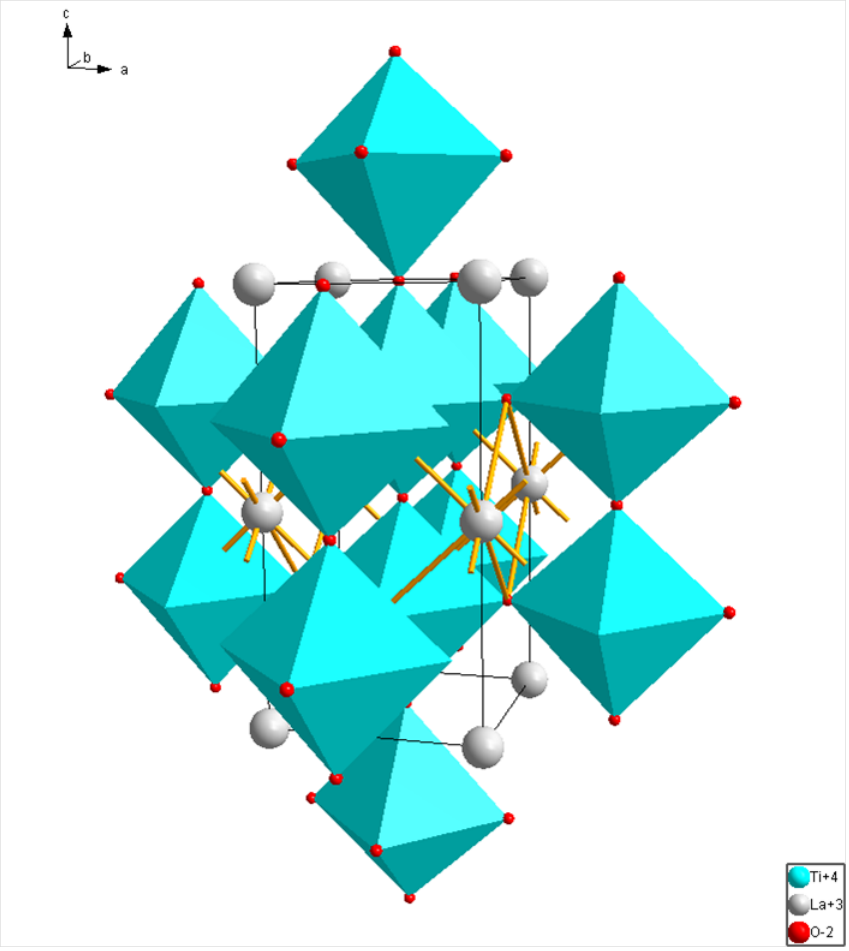


Figure 4.1: Crystal structure of $La_2Ti_2O_7$ showing monoclinic lattice.

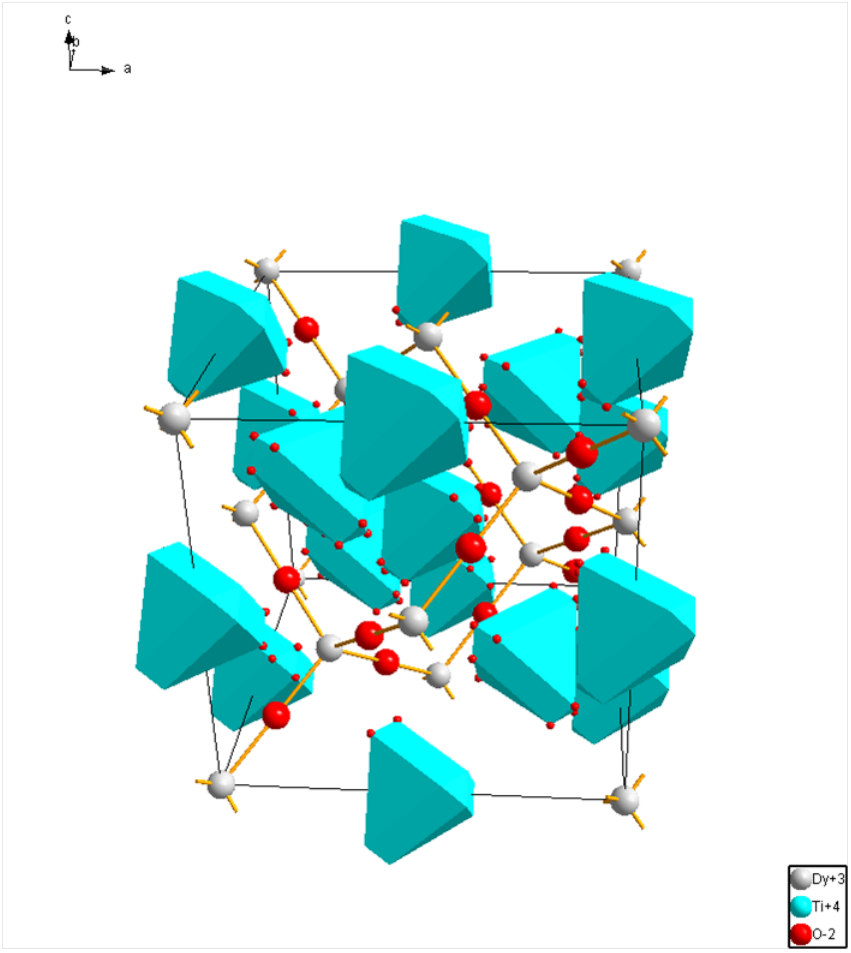


Figure 4.2: Crystal structure of $Dy_2Ti_2O_7$ showing cubic lattice.

For example, $La_2Ti_2O_7$ and $Nd_2Ti_2O_7$ are monoclinic/layered-perovskites, while $Sm_2Ti_2O_7$, $Gd_2Ti_2O_7$ or $Dy_2Ti_2O_7$ are cubic/pyrochlores. The layered-perovskite is thus the stable structure for $Ln^{3+}$=$La^{3+}$ and $Nd^{3+}$, whereas metastable for $Sm^{3+}$, $Gd^{3+}$ and $Dy^{3+}$ under ambient pressure (see Figure 4.3). To stabilize the metastable state, high-pressure syntheses have been used for $Sm_2Ti_2O_7$ and $Eu_2Ti_2O_7$ compound. However, Havelia et al. have already shown the possibility of stabilizing $Sm_2Ti_2O_7$ films with a layered-structure while growing on (110)-oriented $SrTiO_3$ single crystal substrate [127]. These metastable phases are isostructural with the monoclinic $La_2Ti_2O_7$. These compounds are interesting for many useful physical properties such as ferroelectricity, metal-insulator transitions, magnetic frustration/spin ices, magnetoresistance, superconductivity and photocatalytic activity for water splitting [128].

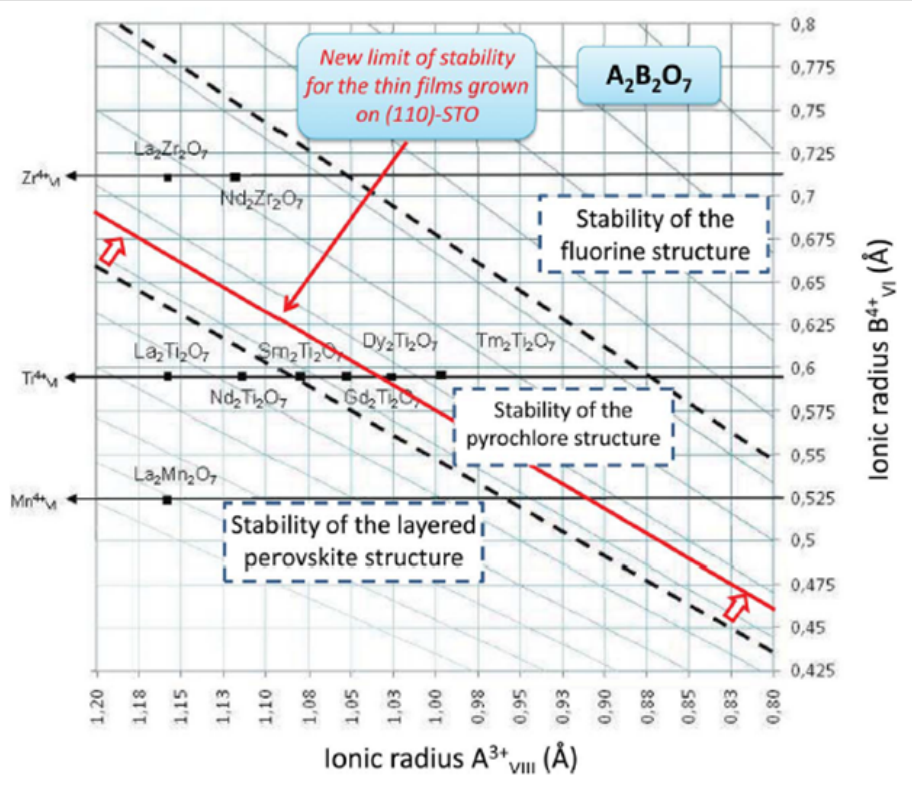


Figure 4.3: Structural stability of $A_2B_2O_7$ vs. ionic radii $A^{3+}$ and $B^{4+}$ [126].

In order to isolate the monoclinic $Dy_2Ti_2O_7$(DTO) thin films, epitaxial strain from a single-crystal can be employed. But, preparing high quality epitaxial layers with such a well-defined structures, atomically smooth surface and interfaces is a challenging task. This is because the epitaxial registry of atoms in the film over the substrate is dictated by various parameters. The main parameters are chemical stability, roughness, thermal expansion coefficient, elastic constant, crystallographic lattice mismatch between the film and the substrate. However, it could be possible to stabilize such a structure in a very peculiar orientation or by adjusting the growth parameters despite its narrow domain of stability. But, as usual the commercially available substrates, in terms of the lattice parameters or structure (most of them being pseudocubic), limits the scope of the study. In this regard, we choose the composition $La_2Ti_2O_7$(LTO) as a substrate to deposit the DTO films and used the CSE approach. The $La_2Ti_2O_7$ compound presents several advantages for growing DTO. It crystallises into monoclinic structure at an ambient pressure, which can be prepared using the classical solid state chemistry routes and offers a small lattice match with DTO (the difference in cation size r($La^{3+}$)=103.2 pm vs. r($Dy^{3+}$)=91.2pm. is

small). This polycrystalline template can not only lead to the crystalline perfection of the epilayer but might induce a transition of the crystal structure from a cubic/pyrochlore in bulk to a monoclinic/layered-perovskite structure. Moreover, such metastable phase of DTO film is expected to be ferroelectric at room temperature, unlike bulk DTO cubic, a centrosymmetric structure but not ferroelectric.

In order to illustrate the CSE approach and prepare DTO thin films, we made dense LTO polycrystalline substrates. This polycrystalline substrate was fine polished, and used to used to grow DTO thin films by PLD. Further, the effect of surface roughness on the stabilization of monoclinic DTO epitaxy film was investigated. The systematic growth of epitaxial structure, characterized by EBSD and HRTEM, is presented.

## 4.2 Experimental

LTO substrates were prepared by mixing of $La_2O_3$ and $TiO_2$ in 1:1 molar ratio ($La_2O_3$, Aldrich and $TiOl_2$, Cerac with 99.9 % purity) using dry ball milling. The ball milled powder was calcined at 1200 °C for 4h. The calcined powder of LTO weighing 5g was mixed with binder, namely poly-vinyl alcohol solution, and dried under infra red lamp in order to remove the water content. Then, it was isostatically pressed at 300 MPa with hold time of 3 minutes.

The pellets were sintered in alumina crucible at 1450 degree for 6h to get dense pellet. This LTO polycrystalline pellets were cut into typical dimensions of 5x2x0.5mm$^3$. The samples were first subjected to mechanical polishing to remove the scratches made by silicon carbide papers with roughness down to 10 $\mu$m for 30 min. Then, the pellets were polished by an automatic machine using diamond liquid (DL) pastes with the grain size of 3 $\mu$m and 1 $\mu$m grain sizes, respectively, for about 2 min, in order to attain a mirror-like surface. Then, a solution of colloidal silica (CS) was used for 1 min as a final polishing step. The surface was etched either using 5 % HF:$HNO_3$ etching solution for 9s and thermal quenching at 1200°C for 1 min to reduce the deformations caused by polishing.

The PLD technique was utilized to grow the epilayer. Briefly, the polycrystalline DTO target was irradiated by the excimer KrF laser ($\lambda$=248 nm) under an oxygen pressure of $10^{-4}$ mbar and substrate was kept at 600-700°C. The frequency used was 0.1 Hz, and the

fluency was close to 1.5 J/cm$^2$. After the deposition, the samples were cooled down to room temperature in the same pressure at a rate of 10°C/min.

Topography maps were were characterized by an AFM-based setup (Veeco-DI, equipped with a Nanoscope IV controller) under ambient conditions using a commercial TiPt-coated silicon tip.

Structural and microstructural characterization of the ceramics and films were carried out using electron backscatter diffraction (EBSD). The samples were mounted at a 70°-tilt angle from horizontal in a scanning electron microscope (FEG-SEM Carl ZEISS SUPRA 55)) operated at 20 kV. Gold was added along the edges of the samples to avoid charging effect on the surface during the experiments. Kikuchi patterns were recorded with a working distance of 15 mm and an aperture size of 60 $\mu$m, and indexed automatically by the EDAX orientation imaging microscopy (OIM$^{TM}$) software (v.6). Automated EBSD scan was performed by scanning the surface of the sample with a beam step size of 0.2 $\mu$m.

TEM investigation were carried out using a FEI Tecnai G2 30 UT microscope operated at 300 kV (point resolution 1.7 Å ). Image simulations were made with CrystalKit and MacTempas software. Cross-section samples were cut parallel to $Dy_2Ti_2O_7/La_2Ti_2O_7$ interface plane, mechanically polished to a thickness of about 15 $\mu$m followed by Ar+ ion beam milling under grazing incidence with respect to the surface. A soft regime of ion milling has been used to prevent any possible artefacts during TEM specimen preparation. The structure and epitaxial relationship with the influence of grain orientation, boundary and misorientation angle between the grains have been investigated in details. The composition of the films was checked by Energy Dispersive Analysis and found to be close to the target within the experimental error.

## 4.3 Results and Discussion

### 4.3.1 Preparation of dense substrate and purity.

LTO substrate should be obtained in monoclinic lattice of space group $P2_1$, stoichiometry composition and highly dense. In this regard, we synthesized LTO powder by conventional solid state route (described in experimental section). The obtained particle sizes are

ranging from 500 nm to 2 $\mu$m with disk shaped (see Figure 4.4(a)).

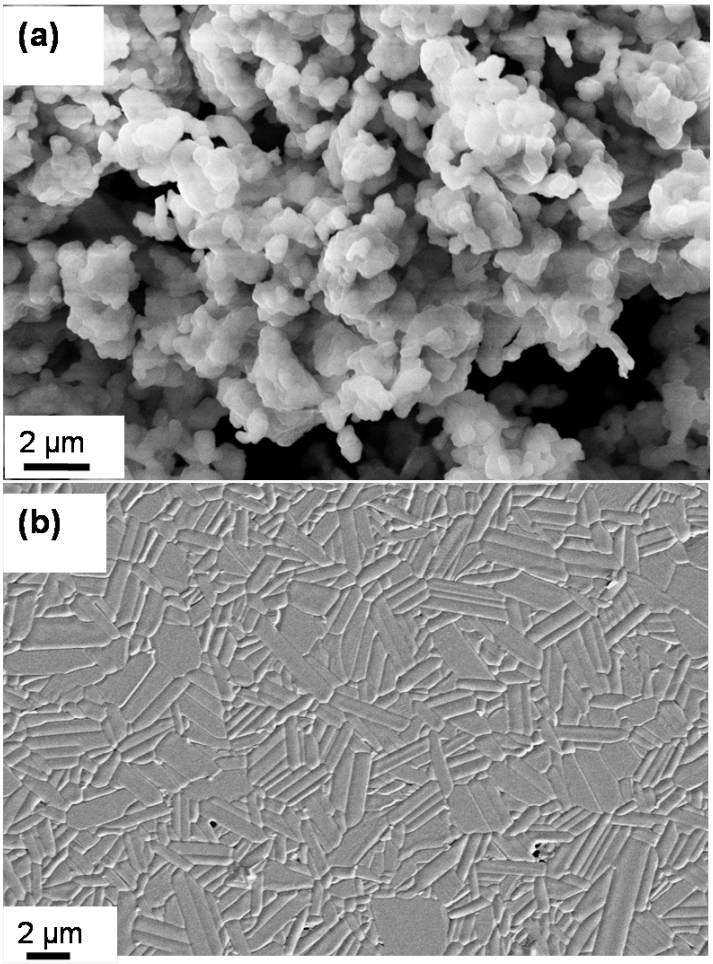


Figure 4.4: SEM image of LTO (a) as synthesized powder (b) polished polycrystalline LTO after thermal etching.

Further, the powder was analysed by XRD to check the phase purity (see Figure 4.5(a)). The detailed XRD analysis shows no impurity peak. The Bragg's planes are well indexed with standard LTO monoclinic lattice of space group $P2_1$. Moreover, XRD analysis confirms the monoclinic lattice of space group $P2_1$. From this analysis, the refined lattice parameters are found $a$=7.816 Å , $b$=5.5412 Å and $c$=13.0067 Å and $\alpha, \beta, \gamma = 90, 98.698, 90°$, in reasonable agreement with the reported bulk samples of LTO [129].

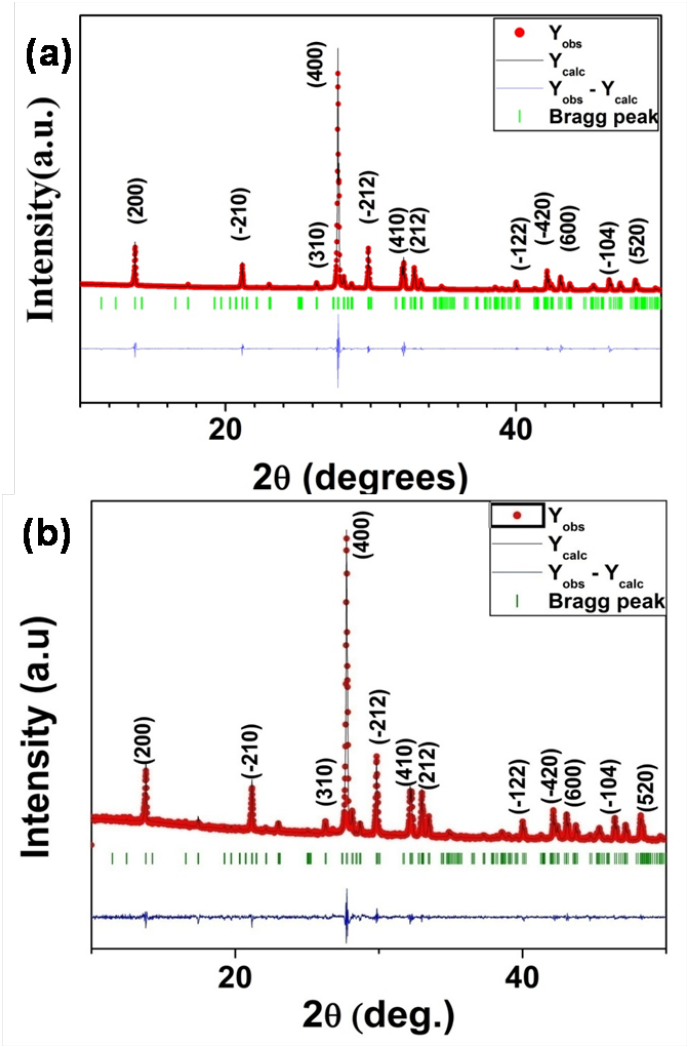


Figure 4.5: Experimental and refined XRD Bragg's pattern of (a) LTO powder and (b) LTO ceramic pellet. The legend shows observed diffraction intensity as $Y_{obs}$ and the calculated intensity from refined pattern as $Y_{cal}$. The Bragg's position are indicated in green vertical bars.

This pure powder of LTO was conventionally sintered to obtain pellet of density 99%. The grains of the LTO polycrystalline are elongated with an average grain size of 5 $\mu m$ corresponding to elongated length and 2 $\mu$m width (see Figure 4.4(b)). This grains are highly packed and randomly arranged. The elongated shape of the grains could be attributed to anisotropic grain growth, from the disk shaped particles of starting powder. Moreover, the consolidation of powder by isostatic pressing induces isotropic arrangements of the grains in the pellet. The phase purity of this LTO polycrystalline pellet was analysed by XRD (see Figure 4.5(b)). From the analysis, the calculated lattice parameters are $a$=7.817 Å ,

$b$=5.5412 Å and $c$=13.00328 Å and $\alpha, \beta, \gamma = 90, 98.668, 90°$) LTO monoclinic lattice of space group $P2_1$. This confirms that the obtained LTO polycrystalline crystallizes in pure phase.

### 4.3.2 DTO epitaxy over chemically etched LTO substrate

LTO substrates were polished, and chemically etched in order to utilize it for film growth. Surface morphology was investigated by AFM to record the topography image (see Figure 4.6).

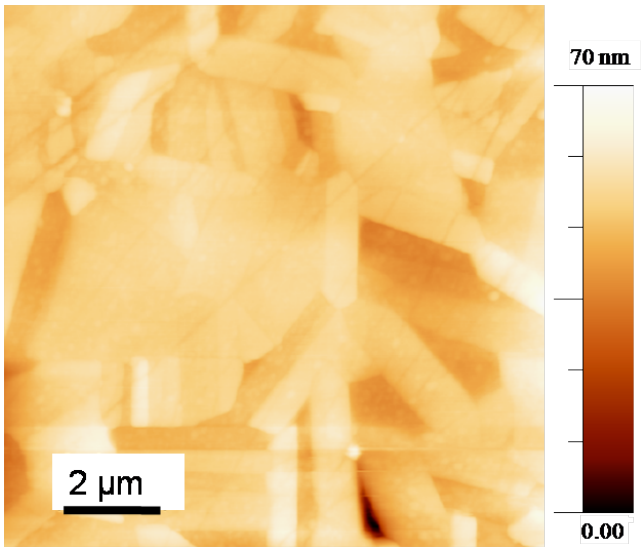


Figure 4.6: AFM image of LTO polycrystalline after chemical etching.

The grain microstructure is clearly seen with elongated shaped and clear grain boundary features. The topography changes from one grain to another. This could be attributed to orientation dependent polishing and chemical etching rate that leads to different roughness of such grains. The average RMS of entire scanned region is 5.75 nm, which confirms that the obtained surface is suitable for film growth.

Further, EBSD pattern was recorded to confirm its crystalline quality and phase nature(see Figure 4.7).

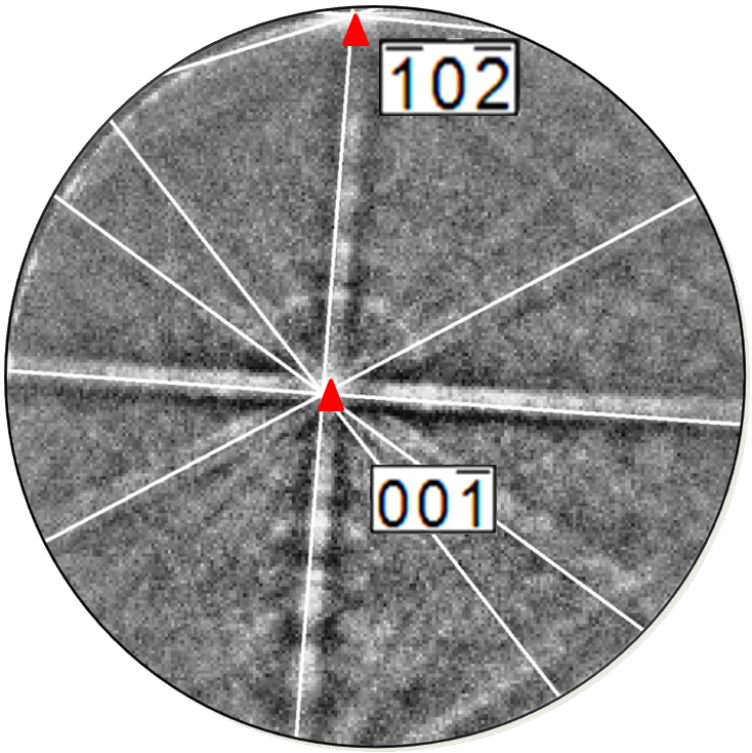


Figure 4.7: Indexed EBSD pattern of LTO ceramic. The red triangle indicates the position of zone axis. The orientation with respect to the surface plane determined from the measured Euler angles in standard angle representation $(\varphi_1, \phi, \varphi_2)$ is (263, 150, 268).

The obtained pattern shows intense intensity (IQ 3400) and sharp features of the bands indicating a strain free surface. The pattern is indexed using structure data file generated from $P2_1$ space group and lattice parameters obtained from XRD analysis of LTO pellet. In this pattern, the intense bands are crossed with 90 ° to each other along zone axis $[00\bar{1}]$, which confirms the presence of two fold (C2) symmetry axis. This symmetry axis is expected from $P2_1$ space group. Moreover, the pattern is better indexable to monoclinic LTO lattice of $P2_1$ space group with fit value of 1 ° and CI of 0.1 . This confirms that the phase obtained is monoclinic.

The automated EBSD scan was performed over the LTO substrate in order to obtain orientation information before deposition of the film and after deposition to determine the epitaxial relationship. However, the surface is highly insulating, resulting in charging effect under electron beam in SEM (see Figure 4.8(a)).

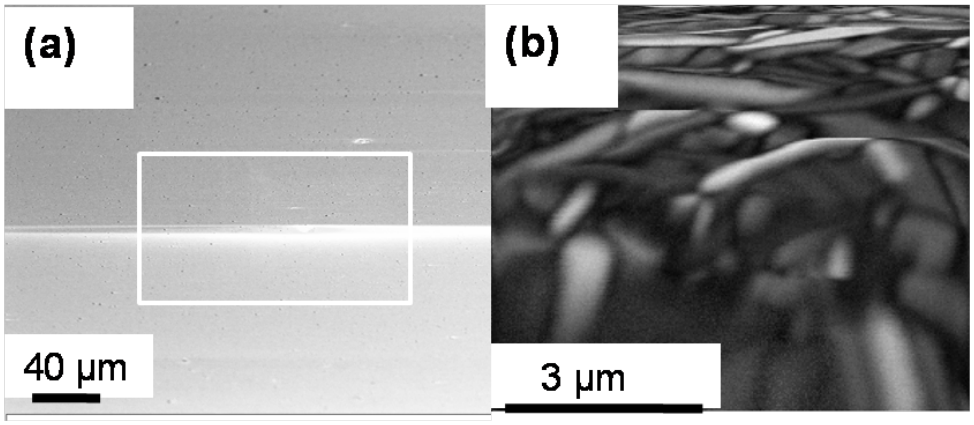


Figure 4.8: (a) SEM image of LTO substrate showing the charged region appearing bright (with white box). (b) Image quality map showing noisy and distorted map due to charging effect.

As a result, the EBSD scan leads to noisy and distorted IQ map (see Figure 4.8(b). The grains appear elongated and distorted due to charging of the electron beam. Even after multiple attempts of EBSD scan with reducing the scan voltage and working distance, we could not obtain a correct image. Moreover, we tried gold coating which resulted in absence of kikuchi pattern.

### Optimization of deposition temperature

DTO films were fabricated at temperatures range's from 600-700 °C. Films of approximate thickness of 70 nm were investigated by EBSD in order to find out the right deposition temperature. The film deposited at 600 °C does not display any bands in the captured pattern (see Figure 4.9(a)), suggesting that the obtained film is amorphous. Further increase in the temperature to 650 °C leads to weak intensity (IQ 1453) and diffused bands of EBSD pattern indicating less crystal quality (see Figure 4.9(b)). The pattern is well indexed using Fd3m space group of DTO cubic lattice of $a$=10.1206 with confidence index(CI) and fit value of 0.1 and 1°, respectively [130].

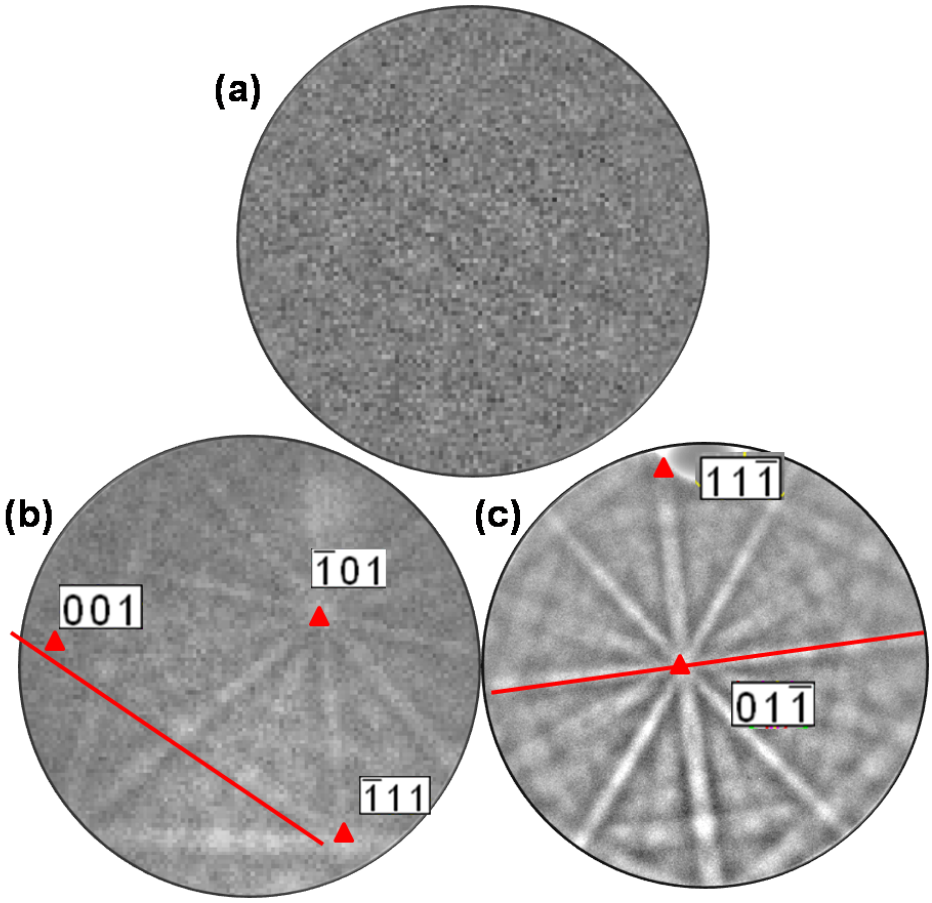


Figure 4.9: (a) EBSD pattern of DTO film grown at temperature (a) 600 °C, (b) 650 °C and (c) 700 °C on LTO substrate. The red triangle indicates the position of zone axis, red line corresponds to mirror plane. The orientation with respect to the surface plane determined from the measured Euler angles in standard angle representation $(\varphi_1, \phi, \varphi_2)$ for (b) (42, 46, 224) and (c) (209, 120, 51).

The main zone axis [001],[$\bar{1}$11], [$\bar{1}$01] are indicated with red triangle in Figure 4.9(b), which have C4, C3 and C2 fold axis, respectively. These symmetry elements are expected in the point group m3m corresponding to space group Fd3m [40]. Further increase in the temperature up to 700 °C leads to intense (IQ 3045) and sharp bands of EBSD pattern indicating good crystallinity (see Figure 4.9(c). The main zone axis [11$\bar{1}$] and [01$\bar{1}$] are indicated with red triangles in Figure 4.9(c), which have C3 and C2 fold symmetry axis, respectively. Moreover, the CI and fit values are 0.3 and 0.4°, respectively. Thus, the pattern of the film grown at 700 °C are better indexable and matched well with the simulated pattern rather than the pattern of the film at 650 °C, where low CI and high

fit value are obtained. We obtained highly crystalline cubic DTO phase at 700 °C, and we further used this optimized temperature for the deposition.

### DTO film with mixed phase

DTO film with thickness of 30 nm were grown (see Figure 4.10).

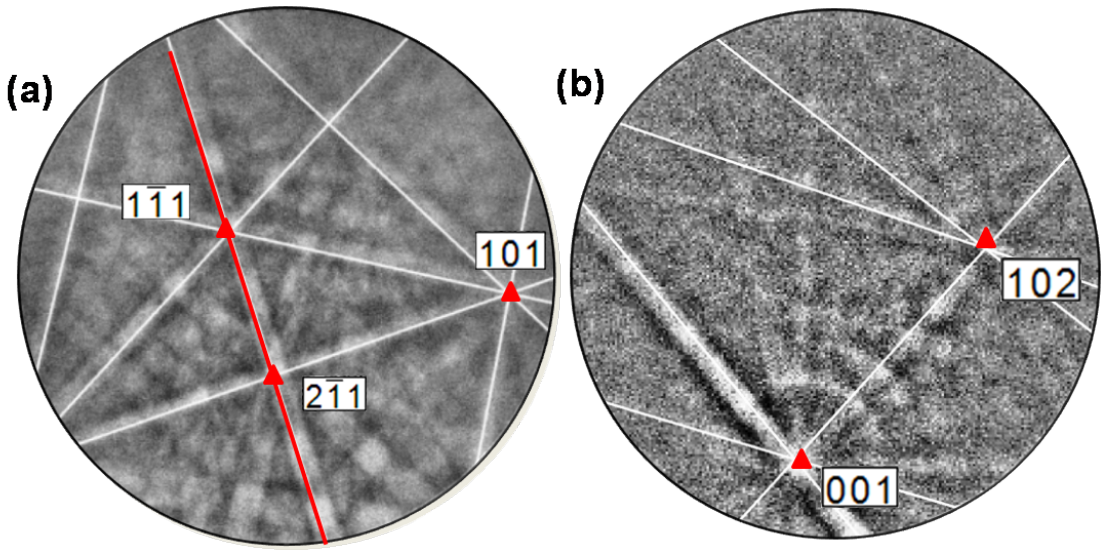


Figure 4.10: EBSD pattern of DTO film with (a) cubic lattice (CI=0.3, fit =0.5 °) and (b) monoclinic lattice (CI=0.1, fit =1 °) are shown. The orientation with respect to the surface plane is determined from the measured Euler angles in standard angle representation $(\varphi_1, \phi, \varphi_2)$ for monoclinic and cubic lattice are (87, 50, 45) and (213, 37, 153), respectively.

These EBSD patterns are sharp and exhibit clear band features, confirming the good crystalline quality of the film. However, there is a clear striking contrasts appearing between the different patterns in terms of zone axis symmetry. The pattern (see Figure 4.10(a)) has $C_3$ fold symmetry axis of $[1\bar{1}1]$ zone axis and mirror plane indicated with red line, that matches with the cubic lattice. While the pattern (see Figure 4.10(b)) has $C_2$ fold axis of [102] zone axis, and matches with the DTO monoclinic lattice with space group $P2_1$. Note that the structure data file for monoclinic DTO was generated by replacing $La^{3+}$ with $Dy^{3+}$ in the structure data file of LTO in order to index the EBSD pattern.

To understand this mixed phase formation, low magnification TEM analysis was performed on a plane section view of the film (see Figure 4.11).

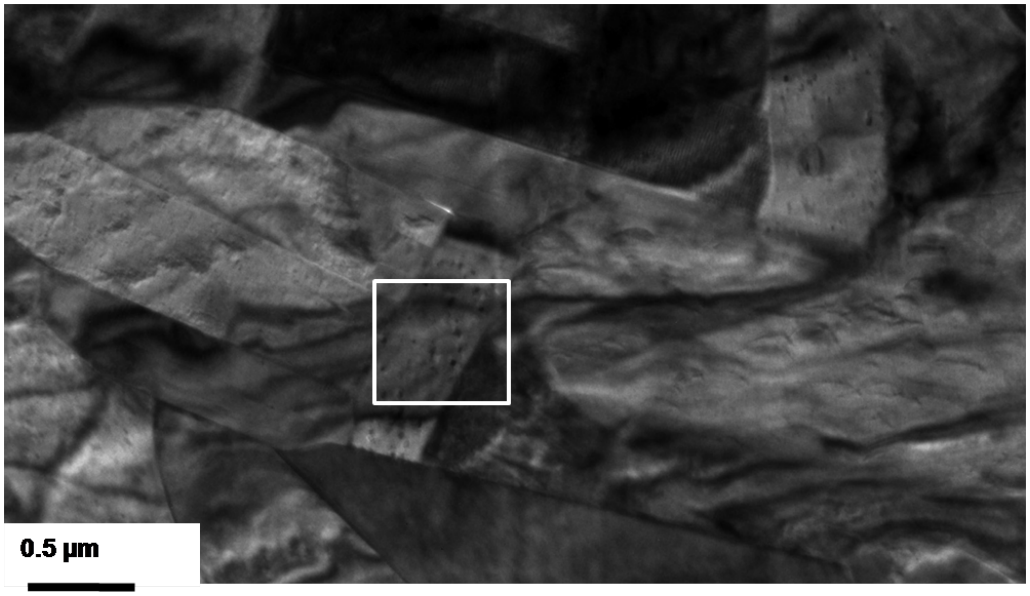


Figure 4.11: Low magnification plane section bright-field TEM micrograph of DTO film grown on chemically etched LTO substrate is shown.

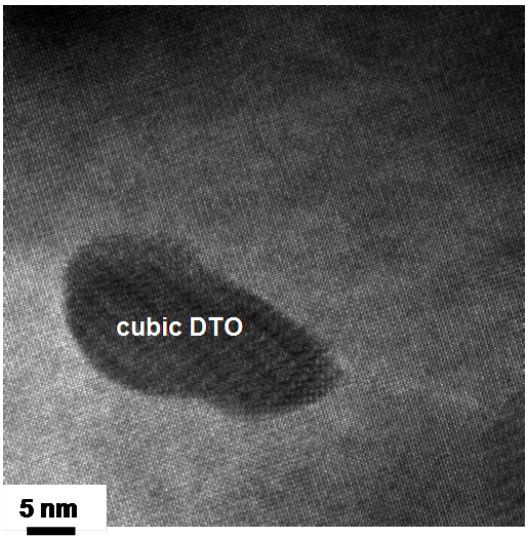


Figure 4.12: HRTEM plane section micrograph of magnified region of DTO film inside the while box indicated in the Figure 10.

The microstructure of the film shows elongated grains and grain boundaries, which are clearly visible in the plane section view. A typical feature is the varying contrast of dark and bright regions in the grain. Moreover, such features arrange in a particular fashion and terraces depending on the grain. This suggests an arrangements of mixed phases of the film depending on the orientation, grain boundary, size and roughness of the substrate.

Further, in the region of the grain highlighted with white box, periodic dark spots are observed. This region was further resolved to obtain HRTEM micrograph (see Figure 4.12). This region corresponds to the spot appearing with different lattice structure, contrary to the uniform structure surrounding it. The presence of such incoherent growth of cubic DTO phase could be attributed to strain relaxation of the epitaxial film structure. To further confirm the presence of such cubic DTO, and resolve the structure, a cross-section was recorded (see Figure 4.13(a)).

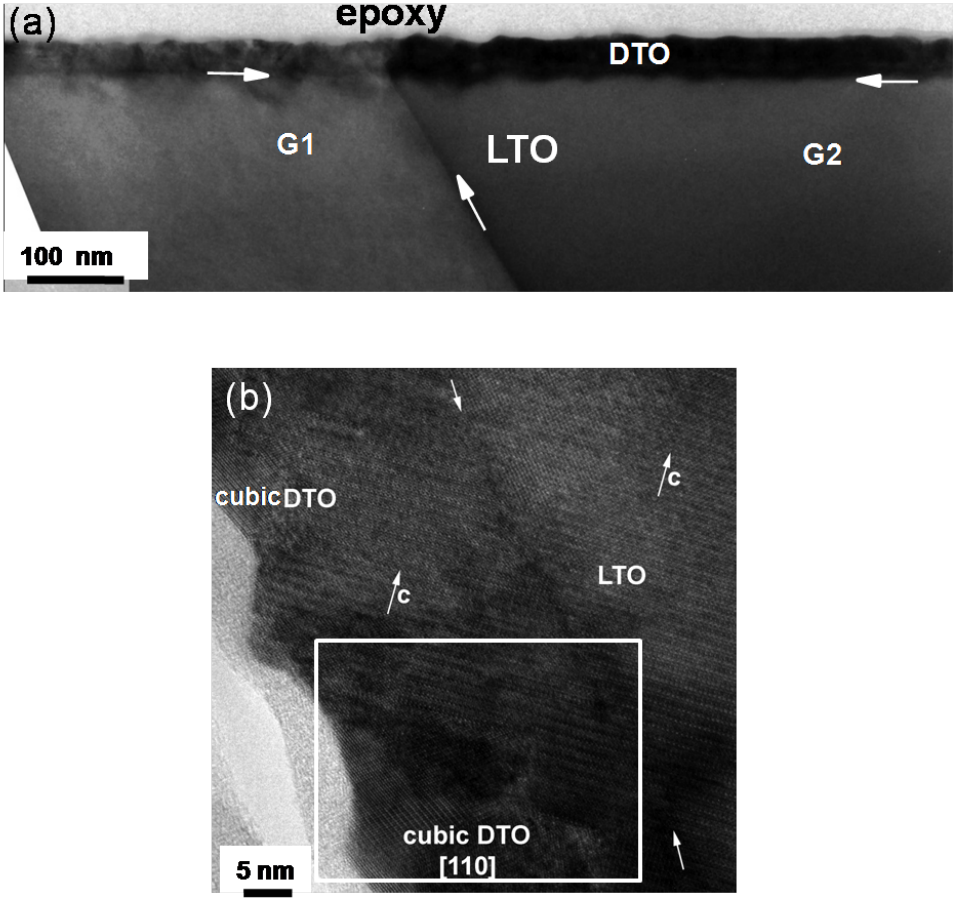


Figure 4.13: (a) Low magnification cross-section bright-field TEM micrograph of DTO film grown on chemically etched LTO substrate showing the film over the grains G1 and G2. The horizontal white arrows indicate the interface of film/substrate. The tilted white arrow indicates the grain boundary. (b) HRTEM cross section micrograph of DTO film grown on chemically etched LTO substrate.

In this micrograph, the surface of the substrate appears wavy as well as the film. This can be attributed to roughness of the substrate. It arises because of the polishing and

chemical etching process used.

The film grows epitaxially and stabilizes with the monoclinic lattice along the c-axis of the substrate grain, but also we observed the presence of cubic lattices incoherently grown over the surface (see Figure 4.13(b)). The lattice mismatch between LTO substrate and DTO film is expected to be small ( as the difference in cation size r($La^{3+}$)=103.2 pm vs. r($Dy^{3+}$)=91.2pm. is small), which leads to stabilization of the epitaxial metastable monoclinic phase by strain just above the interface. But, as the film thickness increases, the structure is unable to accommodate the strain, and this results in stabilization of cubic phase when the film relaxs. Generally epitaxial film generally tends to fully relax to the bulk phase at the specific thickness of the film (see Figure 4.14) [131].

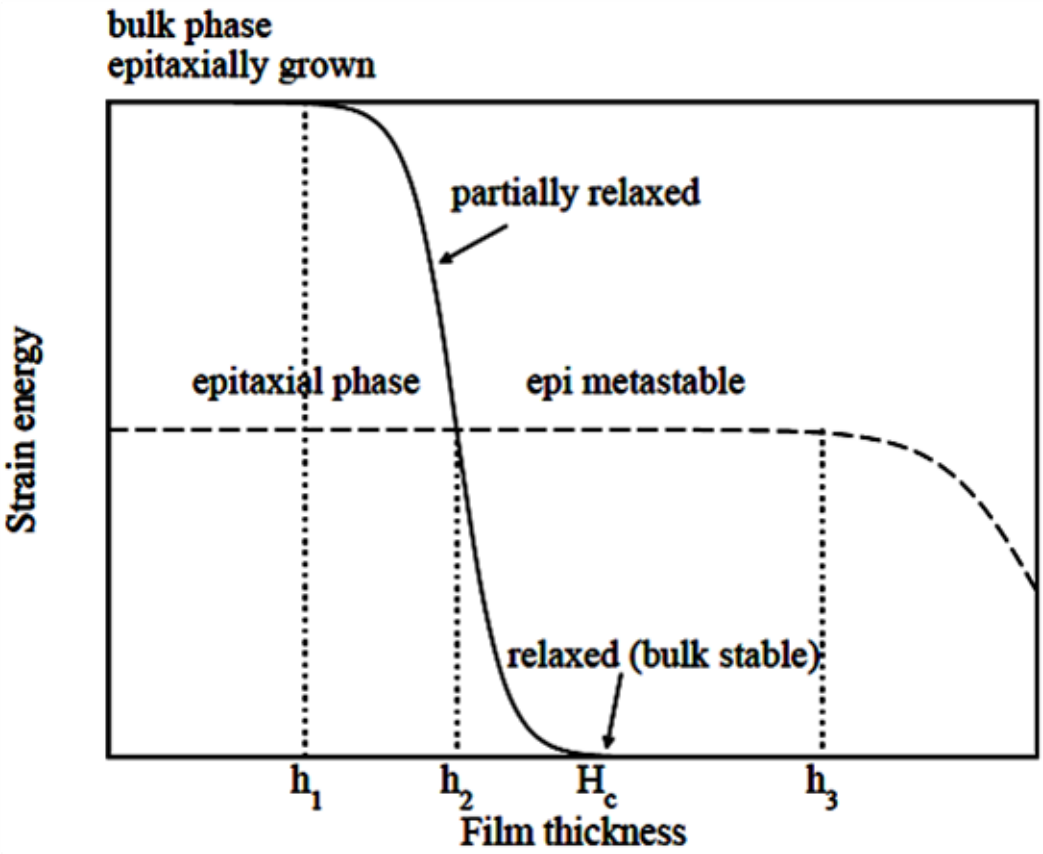


Figure 4.14: Schematic representation of structural change in the epitaxial grown film due strain energy evolution resulting from thickness of the film [133].

However, in the present case, the thickness' above which the two marked cubic lattices stabilizes are 5 nm and 22 nm for bottom and top one, respectively (see Figure 4.13(b). The local strains due to terraces and step height of the wavy substrate surface (see Figure

4.13(a)) could contribute to an additional strain in addition to the mismatch strain [132]. Thus, the critical thickness can be a function of terrace dimension, step height and mismatch strain. In this regard, the absence of specific critical thickness to the marked cubic lattices is attributed to the different roughness of the underneath substrate. Further, to shed more light on the formation of cubic phase and the effect of roughness, Geometric Phase Analysis (GPA) was performed for the cubic phase of bottom one (see Figure 4.15).

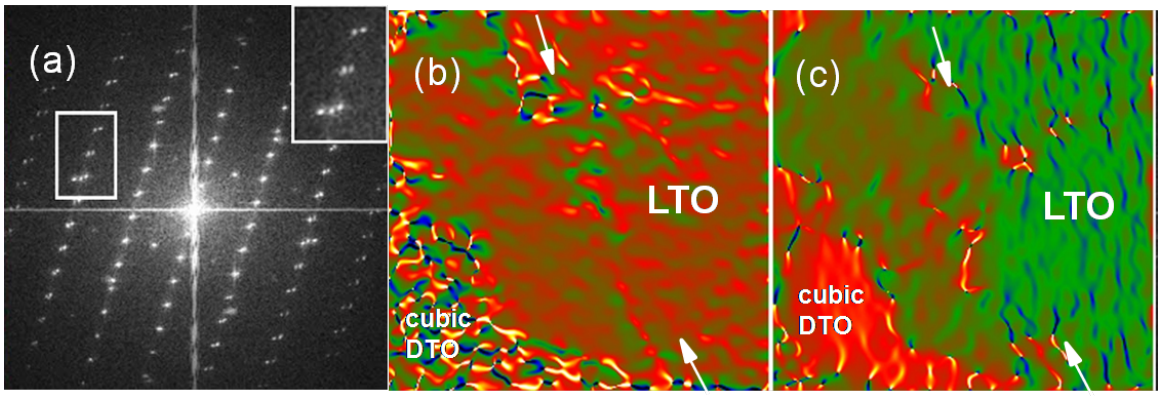


Figure 4.15: (a) Fourier transform (FT) of the HRTEM micrograph of Figure 4.12 (b) showing the diffraction spots. White rectangle shows three spots, which corresponds to substrate, monoclinic and cubic phase, respectively. The color coded GPA map shows the strain variation of (b) in-plane $\epsilon_{xx}$ and (c) out-of-plane $\epsilon_{yy}$ with reference to LTO substrate.

The method of GPA allows to locate the crystal distortions in the structure by analysing changes in the phase of the FT diffraction pattern. The FT pattern (see Figure 4.15(a)) displays diffused Bragg's intensity, which generally occurs due to presence of grain size, strain and defects in the crystal structure [134].

The obtained color coded GPA strain map (see Figure 4.15(b)) of in-plane lattice parameter shows the uniformity of color as moved from LTO substrate to the film, which confirms the epitaxial growth. The sharp variation at the interface with dark red could be observed due to the roughness of the film. The strain variation in the region of marked cubic phase is seen. In out-of-plane GPA strain map of lattice parameter, the film exhibits uniform color that indicates uniform strain (see Figure 4.15(c)), but the film is more strained compared to in-plane lattice parameter. This means that the film relax along $c$-axis.

In a coherent strained monoclinic DTO film, there could be a possibility of deformation or rotation of $TiO_6$ octahedra up to a certain thickness [135]. However, the influence of substrate over the film structure gets reduced when thickness increases [136]. As the film tends to relax by structural and microstructural changes. This structural relaxation mainly depends on growth conditions, surface roughness, thickness, thermal expansion coefficient, elastic constant and crystallographic lattice mismatch between film and substrate. These parameters ultimately decide the mechanism of relaxation and the film structure when thickness increases. The various ways by which the structure relax are misfit dislocation, formation of boundaries, domains and phase transition etc [137, 138]. In the GPA strain map recorded for both in-plane and out-of-plane, the presence of continuous lattice planes of the film indicates the absence of misfit dislocations. However, the film relaxes to cubic phase, which could be attributed to the roughness of the film. As the kinetics of the film growth are expected to be different from that of the film grown on flat substrate surface.

### 4.3.3 DTO epitaxy over thermally etched LTO substrate

To understand the effect of roughness on the formation of cubic DTO, a thermal etching process was employed to relax the LTO substrate. In thermal etching, the substrate was placed inside a pre-heated furnace kept at 1200°C, and quenched to room temperature after 1 minute. The EBSD pattern was captured on 30 nm DTO film. Bands are sharp and intense pattern, showing a low symmetry EBSD pattern, which corresponds to the monoclinic DTO lattice (see Figure 4.16(a)). Further increase of the film thickness up to 70 nm leads to diffused bands of low symmetry pattern indicating strain in the monoclinic film (see Figure 4.16(b)). This could be attributed to an epitaxial strain in the surface crystal planes that leads to diffused bands [75]. The increase in film thickness above 70 nm, leads to high symmetry EBSD pattern, which corresponds to the cubic DTO lattice (see Figure 4.16(c)). This presence of cubic DTO lattice above a certain thickness indicates that the strained monoclinic DTO is fully relaxed.

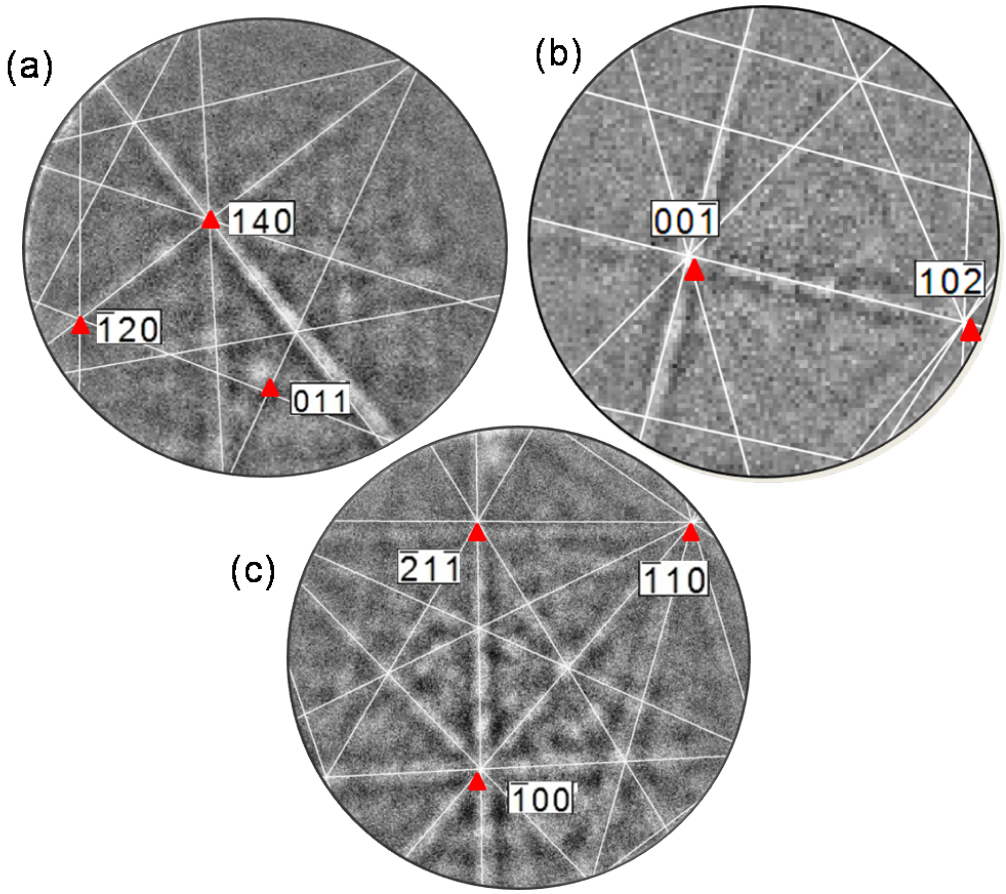


Figure 4.16: EBSD pattern of DTO film with monoclinic lattice seen over the film having thickness (a) 30 nm (CI=0.2, fit =0.3 °), (b) 70 nm (CI=0.1, fit =1 °) and (c) cubic lattice is seen over film having thickness 100 nm when grown over thermally etched LTO substrate (CI=0.5, fit =0.2 °). The orientation with respect to the surface plane determined from the measured Euler angles in standard angle representation $(\varphi_1, \phi, \varphi_2)$ for (a), (b) and (c) are (132, 116, 13), (257, 141, 182) and (145, 115, 308), respectively.

The effect of roughness upon the presence or absence of cubic phase in DTO film (thickness ranging from 30 nm and 100 nm) were investigated by AFM (see Figure 4.17). The topography image obtained from the 30 nm thick film appears to be uniform. The RMS roughness of this surface is 4.4 nm (see Figure 4.17(a)). This low roughness could be attributed to coherent growth of monoclinic DTO on flat surface of LTO due to thermal etching. However, the topography image obtained with the 100 nm thick film appears to be more rough (RMS = 7.9 nm) probably due to the presence of small clusters of film grains contained within the grain of the substrate (see Figure 4.17(b)). Such formations of small grains could be attributed to the transformation of monoclinic DTO into cubic

DTO phase.

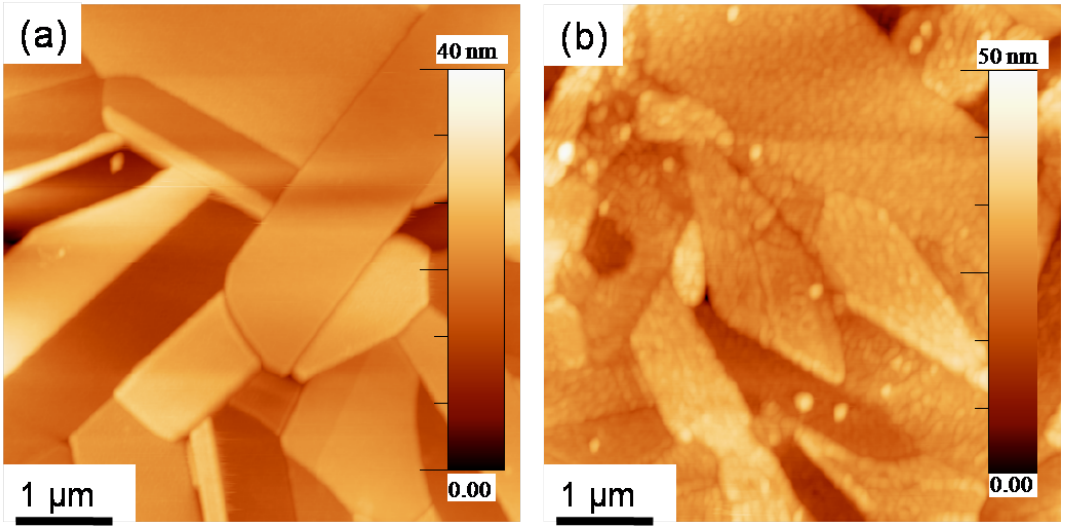


Figure 4.17: AFM topography image obtained over DTO film grown on thermally etched LTO of thickness (a) 30 and (b) 100 nm.

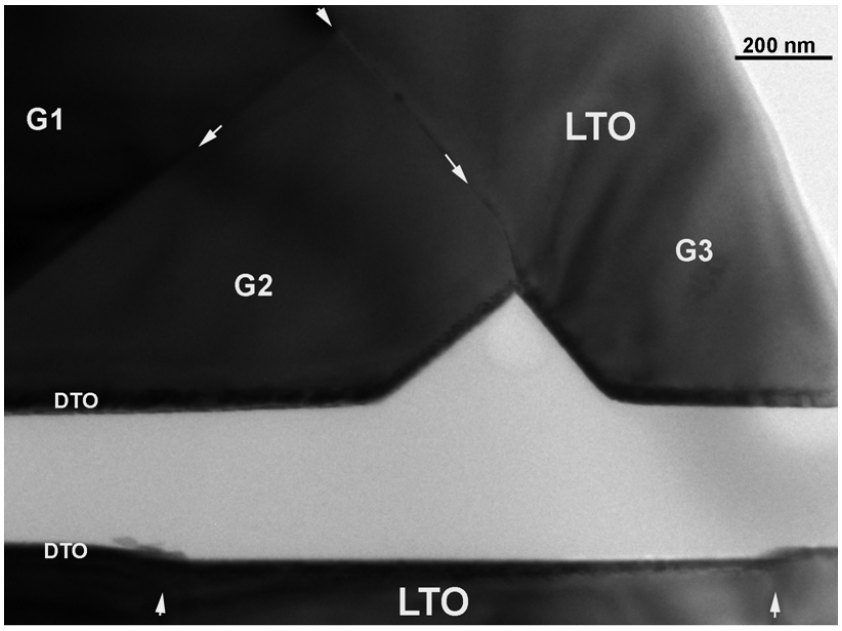


Figure 4.18: (a) Low magnification cross-section bright-field TEM micrograph of DTO film grown on thermally etched LTO substrate showing the film over the grains G2 and G3 along the V shaped from the top part and flat surface of grain in the bottom part. The white arrows indicate the grain boundaries.

Figure 4.18(a) shows a low-magnification cross-section TEM micrograph of DTO film grown on top of a thermally etched LTO surface. Clearly, the surface of the DTO film is

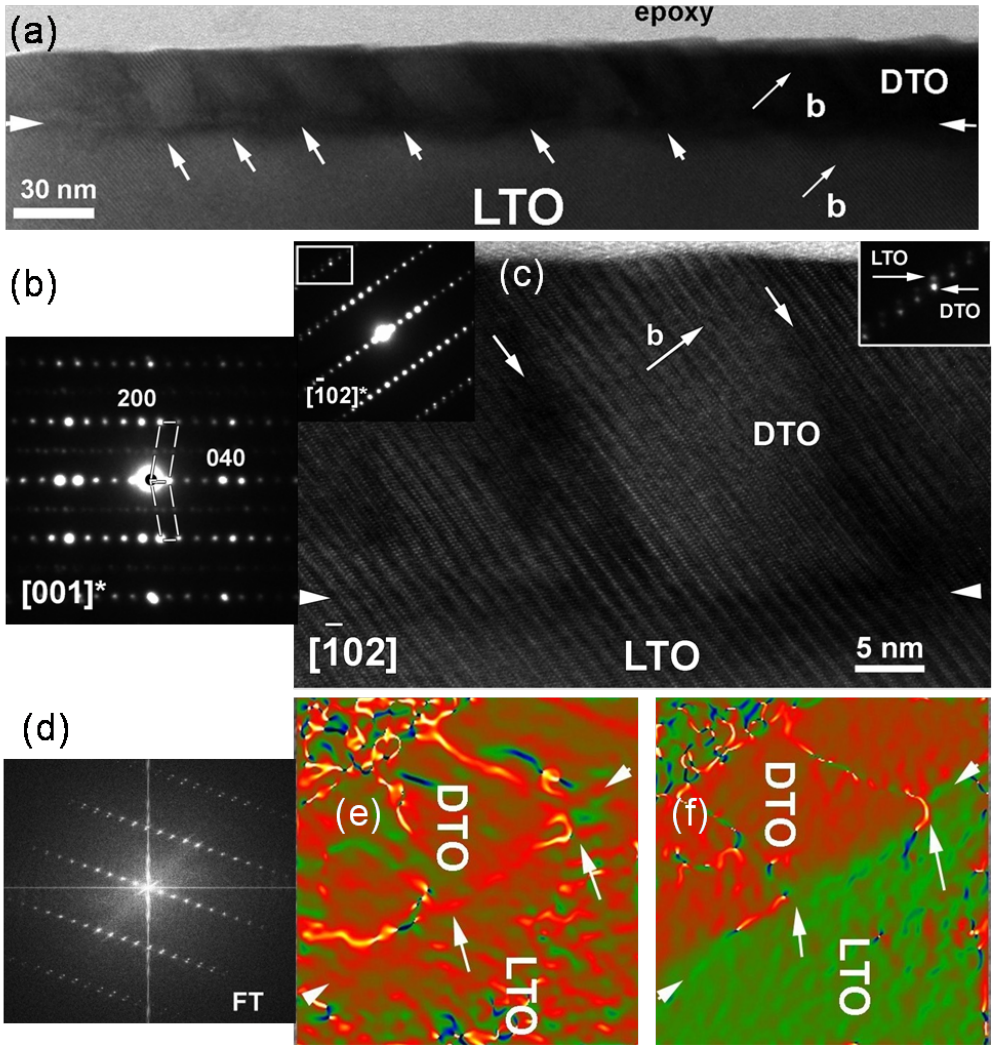


Figure 4.19: a) Low magnification cross-section bright-field TEM micrograph of DTO film grown on LTO substrate showing the epitaxial growth along b-axis. The horizontal white arrow indicates the interface of film/substrate and tilted white arrows for the low angle boundaries. (b) The corresponding [001] SAED pattern of (a) is shown. The highlighted reflections belongs to the monoclinic unit cell of space group $P2_1$. (c) HRTEM micrograph of b-axis oriented DTO film along [$\bar{1}$02] zone axis, also with the corresponding ED pattern is given as insert. Further, the magnified ED pattern is shown right insert in the marked white rectangle, which indicates the superposition of the electron diffraction pattern of substrate and the film. (d) The Fourier transform (FT) of the HRTEM micrograph of (c) shows the Bragg's spots from the structure. The color coded GPA map shows the strain variation of (e) in-plane $\epsilon_{xx}$ and (f) out-of-plane $\epsilon_{yy}$ with reference to LTO substrate.

extremely flat, which we attribute to the relaxation of the substrate's surface by ther-

mal etching contrary to the chemical etching process. The coherent growth of film can be seen over the V shaped edge confirming highly epitaxial growth of film.

In order to resolve the structure and understand the interface, the cross section HRTEM micrographs of DTO film grown on thermally etched LTO substrate was recorded (see Figure 4.19(a). There is no sharp contrast at the interface between DTO film and LTO substrate, which confirms that both DTO film and LTO substrate have a similar structure and close lattice parameters. The DTO film exhibits periodic boundary like feature, (indicated with the tilted white arrows in see Figure 4.19(a)). To understand the formation of such boundaries, GPA of HRTEM analysis (Figure 4.19(c)) were carried out. The GPA strain map (see Figure 4.19(e)) of in-plane lattice parameter shows the boundary like features, which appears in bright colors. In the GPA strain map of out-of-plane lattice parameter (see Figure 4.19(f)), the film exhibits more strained compared to the in-plane lattice parameter, but with an uniform strain ( the GPA map shows uniform red color). The boundary planes appear green, which indicates less strain in comparison with the strain of boundary plane along in-plane lattice parameter. This indicates that the boundary planes are relaxed along $c$-axis, and strained along $a$ and $b$ axis.

A low magnification plane section view of the film was recorded to further understand the structure (see Figure 4.20).

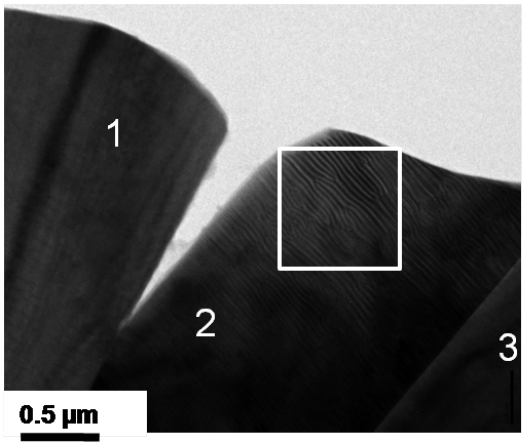


Figure 4.20: Low magnification plane section bright-field TEM micrograph DTO film grown on chemically etched LTO substrate.

The marked grains 1 and 3 do not show any feature of structural relaxation, since a uniform contrast is seen. The grain 2 shows a region of patterned boundary planes

covering the entire grain in the surface plane. The magnified HRTEM image over this grain can be better seen with resolved features of the periodic boundary planes (see Figure 4.21(a)). In this view, these boundary planes are arranged in a Moiré pattern, as the boundary planes appear rotated from a point . Moreover, the boundary planes are parallel to the (001) that can be inferred from plane view and cross section view. In the cross section, the zone axis [001] is also the viewing direction of the boundary planes (see Figure 4.19(a) and 4.19(b)). In the plane view, boundary planes are along c-axis, which confirms that boundary plane is parallel to (001). In the magnification of region ( see Figure 4.21(a)), the boundary planes are not sharp, but curled and connected with the neighbour planes (see Figure 4.21(b)). Such a formation of boundary plane morphology could be attributed to the effect of grain boundary and orientation of the grain substrate. The atomic resolved structure of boundary planes are better seen in magnified HRTEM micrograph of Figure 4.21(b) (see Figure 4.21(c)). The presence of internal references from LTO substrate in the ED pattern (see Figure 4.21(b) insert) enabled to measure the lattice parameters of DTO film with a high accuracy of $a$=7.53 Å , $b$=5.31 Å and $c$=13.03 Å and $\alpha, \beta, \gamma = 90, 98.65, 90°$). In comparison with LTO substrate, the calculated $a$ and $b$ lattice parameters of DTO film decrease by 3.6 % and 4.1 % . But, the monoclinic angle $\beta$ and the calculated $c$ lattice parameters are less perturbed because of strain relaxation by boundary formation. The simulated DTO structure ( inset of Figure 4.21(c), based on the monoclinic DTO shows a good agreement with the experimentally observed structure.

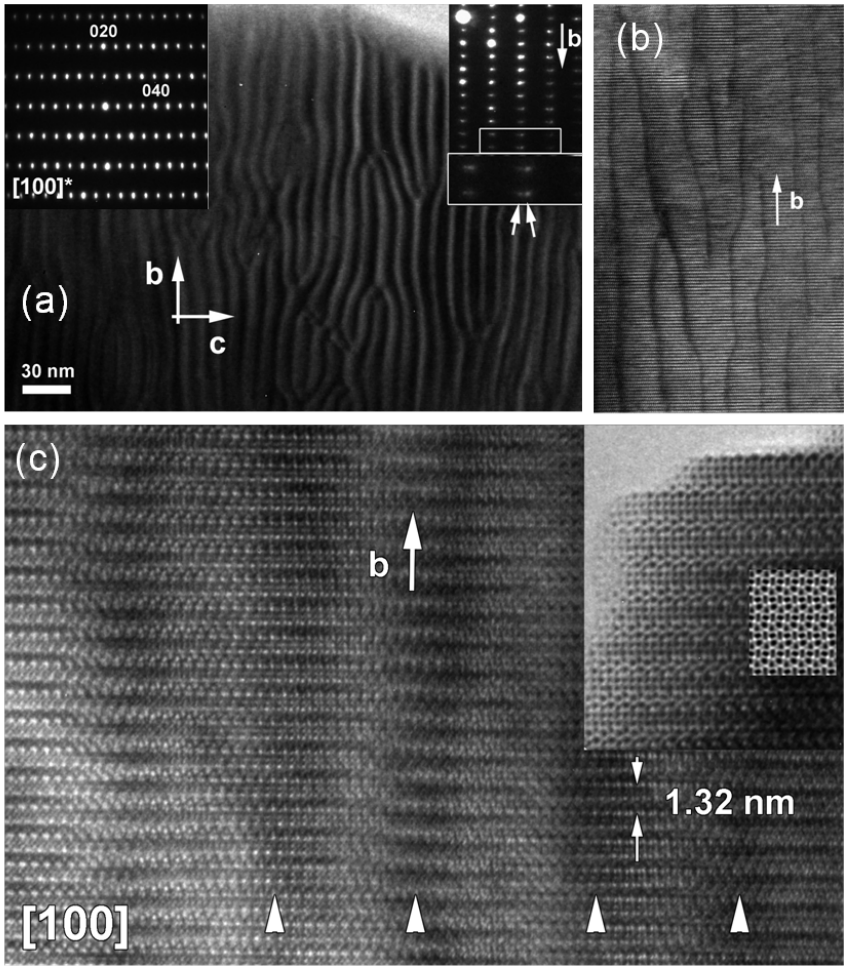


Figure 4.21: HRTEM (a) plane section micrograph of DTO film grown on thermally etched LTO substrate is shown. The corresponding ED pattern is given as insert. Further, the marked small white rectangle ED pattern is magnified to indicate the superposition of the electron diffraction pattern of substrate and of the film in big white rectangle. (b) The magnified HRTEM micrograph of region in (a) is shown. The corresponding [100] SAED pattern of (a) is shown. The highlighted reflections belongs to the monoclinic unit cell of space group $P2_1$. The enlarged ED pattern given as insert to the right showing the resolved diffractions spots from film and substrate. Further, the marked white rectangle ED pattern is magnified to indicate the superposition of the electron diffraction pattern of LTO substrate and DTO film. (c) The magnified HRTEM micrograph (b) is shown, the white arrow cap indicates the boundary region. Also, the enlarged portion of strain free portion of DTO film indicated with arrows, together with a computer simulated image given as insert.

In summary, the structural study of DTO film grown on chemically etched and thermally etched LTO substrates are represented by a schematic model for 30 nm thick film (see Figure 4.22).

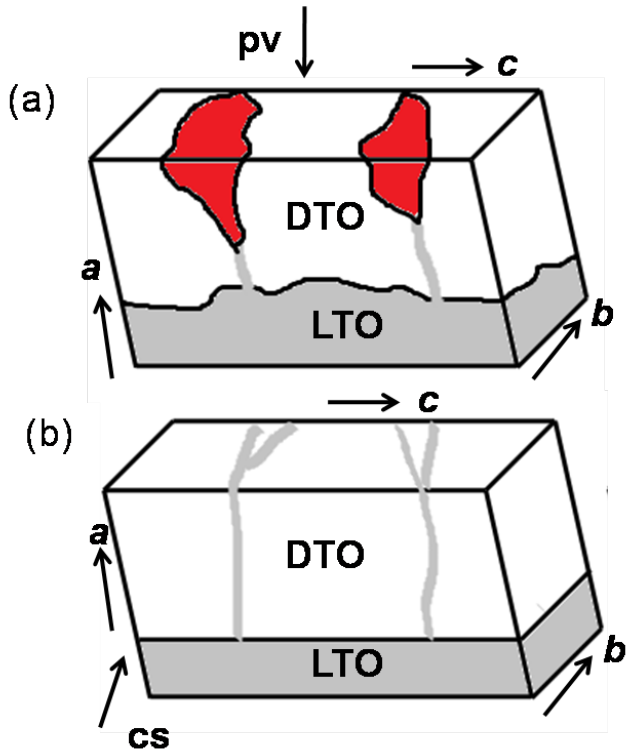


Figure 4.22: The schematic representation of epitaxial growth of DTO film on (a) chemically etched and (b) thermally etched LTO surface is shown. The notation of pv denotes plane view and cs for cross-section view. The light gray indicates the boundaries.

The rough surface of chemical etched LTO substrate leads to incoherent growth of cubic DTO , which is indicated in red in color (see Figure 4.22(a)). The films tends to relax at different thickness to cubic DTO depending on film roughness. The DTO film grows coherently in a monoclinic structure over thermally etched LTO substrate with periodic boundaries parallel to (001) plane (see Figure 4.22(b)), confirming the importance of the surface of substrate.

We further investigated the effect of this strained monoclinic DTO layer on its ferroelectric properties. In order to probe the ferroelectric nature of the DTO film, PFM measurements were carried out. However, this work is still in progress and will not be discussed in this chapter.

### 4.3.4 Main results of chapter 4

1. The chemically etched LTO substrate leads to the formation of cubic and monoclinic DTO at thickness around 30 nm.

2. The thermally etched LTO substrate leads to the stabilization of metastable monoclinic DTO at thickness 30 nm. The strain relaxation in such a film occurs by the formation of boundary planes along the (001).

## 4.4 Conclusion

In summary, we have found that the DTO can be stabilized in the monoclinic metastable structure in thin film using CSE approach. The structural characterizations using EBSD and HRTEM confirm that the thermally etched LTO substrate surface is better for stabilizing the monoclinic DTO film. The chemically etched LTO surface leads to a mixed phase of DTO film. The strain relaxation in such a film occurs by the formation of boundary planes along the (001). Thus, combinatorial substrate epitaxy based on polycrystalline ceramic with appropriate composition can be promising to stabilize the metastable phases of the film. It represent a promising approach to develop novel phases of strongly correlated system with properties different from bulk form

# Chapter 5

# Conclusion and Perspectives

From a practical point of view, epitaxial layers are usually grown on single-crystals with a similar structure and a small mismatch. However, earlier research's have been restricted because of the limited range of compositions and low-index of commercially available single crystal substrates [25]. Also, unusual composition and/or high-index ($hkl$) single crystal substrates are either very costly or unavailable. Thus, novel epitaxy synthetic methods need to be developed in order to go beyond this limitation on availability of single crystal substrates in terms of phase, composition, size, orientation and symmetry. One such approach is a high-throughput synthesis process called combinatorial substrate epitaxy(CSE), where a metal oxide film is grown epitaxially on a polycrystalline substrate [26–30]. CSE relies on polycrystalline substrates in which each grain can be viewed as a single crystal substrate with a specific crystallographic orientation. A multitude of different orientations of the metal oxide film can be obtained in a single deposition over the polycrystalline substrate. Thanks to the integration of high-resolution structural analysis at the grain scale, this approach generates a whole library of film data as a function of the orientation of substrate grain in a single experiment. Furthermore, the dependence on commercial availability of substrates is no longer an issue since -the synthesis of polycrystalline substrates with some tunability of the grain size becomes possible.

In the present thesis work, the prospect of CSE was investigated in details and summarized on the following chapters :

In chapter 1, we briefly describe the synthesis and characterization techniques used in the current thesis work. The objective of this work is to obtain functional films by com-

binatorial substrate epitaxy (CSE), i.e, with epitaxial relationship of the film to the crystallites of the polycrystalline substrate. The chapter provides an overview of the Spark Plasma Sintering (SPS) of polycrystalline substrates and the Pulsed Laser Deposition (PLD) of thin films. Electron Backscatter Diffraction (EBSD) is then described in details since it is a crucial tool for the characterization of the local crystallographic orientation of the substrates and films. The structural characterization also relies on X-ray Diffraction (XRD) and High Resolution Transmission Microscopy (HRTEM). The techniques used to characterize the specific physical properties of the films, i.e. thermoelectricity (by measurement of electrical resistance and Seebeck coeficient) and ferroelectricity (by Piezoelectric Force Microscopy).

Chapter 2 presents the enhancement of Seebeck coefficient in the $Ca_3Co_4O_9$ epitaxial films. In this regard, we have first synthesized textured alumina ceramic obtained by SPS of undoped commercial $Al_2O_3$ powders. These alumina ceramics were fine polished, chemically etched and used for growing the nanostructured epitaxial $Ca_3Co_4O_9$ thermoelectric films using PLD with a controlled microstructural defects. The structural quality of the thin films were secondly investigated by Transmission Electron Microscopy, while the crystallographic orientation of the grains and the epitaxial relationships were determined by EBSD. Utilization of the polycrystalline ceramic template leads to the nanostructured films with good local epitaxial registry, and finally results in the enhancement of the Seebeck coefficient to 170 $\mu$V/K at 300 K. The enhancement of Seebeck coefficient is attributed to the low carrier concentration. Moreover, the effect of polycrystalline substrate leads to nanostructuring and band engineering in addition to strain engineering.

Chapter 3 develops a strategy to collect library of orientation dependent ferroelectric properties in $BiFeO_3/La_{0.7}Sr_{0.3}MnO_3$ at a small scale. In order to address this, $BiFeO_3$ (BFO) / $La_{0.7}Sr_{0.3}MnO_3$ heterostructured thin films were grown by pulsed laser deposition on $LaAlO_3$ (LAO) polycrystalline substrates. Both polycrystalline LAO substrates and BFO films were locally characterized using EBSD, which confirmed the high-quality local epitaxial growth on each grain of the substrate. Piezoforce microscopy was used to image and switch the piezo-domains, and the results are consistent with the relative orientation of the ferroelectric variants with the surface normal. Moreover, the effects of thickness on the phase formation over of (001) planes were investigated.

Chapter 4 investigates the stabilization of metastable monoclinic $Dy_2Ti_2O_7$ epitaxial films. In the $Ln_2Ti_2O_7$ (Ln=lanthanide) series, $La_2Ti_2O_7$ is for example a monoclinic layered-perovskites, non-centrosymmetric, and exhibit ferroelectric properties, while $Dy_2Ti_2O_7$ is a cubic/pyrochlore, a centrosymmetric structure (and not ferroelectric). To isolate a metastable phase, epitaxial strain degenerated from a single-crystal is often employed. However, the commercial availability of the substrates, in terms of lattice parameters or structure (most of them being pseudocubic), seriously limits the scope of the study. Here, we synthesized highly dense $La_2Ti_2O_7$ (LTO) polycrystalline ceramic by conventional sintering. This substrate was fine polished and chemically etched for the growth of DTO films. The deposition temperatures of DTO films were optimized by analyzing the EBSD patterns. This film was found to be cubic phase. Further, the formation of cubic and monoclinic DTO was observed on decrease in the film thickness. Such mixed phases are closely attributed to the roughness of LTO substrate due to chemical etching, which is confirmed by HRTEM studies. Further, 30 nm thick film grown over thermally etched LTO substrate was stabilized into metastable monoclinic DTO, which is confirmed by EBSD and HRTEM analysis. Thus, the use of CSE approach, not only leads to the crystallinity perfection of the epilayer but also induces the structural transition from a cubic/pyrochlore in bulk to a monoclinic/layered-perovskite structure, which is expected to be ferroelectric at room-temperature.

Future Perspectives :

(a) Nanostructured metals and alloys have shown a variety of chemical and physical properties that can be further fine tuned by engineering the microstructure at the nanoscale. The use of the textured substrates provides the promising of control of the structure and orientation of the film growth through a novel oriented-grain strain engineering. Search of the complex thermoelectric oxides to realize the high figure-of-merit, is generally limited by the high temperature solid state diffusion reactions, that can now be realized by choosing proper polycrystalline substrates. The high concentration of defects in the grain contact area resulting from their crystallographic misalignment is also expected to increase the phonon scattering at the grain boundaries of the films, and thus enhance the thermoelectric properties of the films. In a broad perspective, this approach can be further expanded to nanostructure the functionalized oxides for high performance

thermoelectric films.

(b) The wide range of crystal orientations available in the polycrystalline substrate that opens a high throughput route for establishing the libraries of specific properties as a function of orientation in the oxide films. Moreover, CSE approach can be useful to the epitaxial growth and structure-property relationships of multifunctional oxides with complex atomic structures, such as $GaFeO_3$ or $Gd_2Mn_2O_5$, for which isostructural substrates are not commercially available.

(c) Combinatorial substrate epitaxy based on polycrystalline ceramic with appropriate composition can also be promising to stabilize metastable phases of the film and is promising in coming future to develop novel phases of strongly correlated system with electric properties different from the bulk form

(d) The established synthesis of ceramic in different compositions and tunable grain sizes unlike commercial single crystal substrates with limited orientations and compositions, that provides an advantage in obtaining combinatorial film property as a function of composition, phase, size, orientation and symmetry. In this regard, tailoring quantum structure of chosen parent oxide structure in epitaxial form with desired properties can be achievable. Thus, such a study can be promising for novel electronic oxide structure that can be obtained using CSE approach, opening the way towards unexpected electronic properties in oxide films.

# Bibliography


[1] McPherron, S. P., Z. Alemseged, C. W. Marean, J. G. Wynn, D. Reed, D. Geraads, R. Bobe, and H. A. Bearat. Nature Materials 6, 466:857-860 (2010).

[2] S.-W. Cheong, Nature Materials 6, 927 (2007).

[3] John B. Goodenough Chem. Mater., 26 (1), 820-829 (2014).

[4] Y. Tokura and N. Nagaosa Science 288, 462-468 (2000).

[5] Guus Rijnders and Dave H. A. Blank Nature Materials 7, 270-271 (2008).

[6] Philippe Ghosez and Jean-Marc Triscone Nature Materials 10, 269-270 (2011).

[7] C. H. Ahn, J.M. Triscone and J. Mannhart Nature Materials 424, 1015-1018 (2003).

[8] Darrell G. Schlom, Long-Qing Chen, Xiaoqing Pan, Andreas Schmehl and Mark A. Zurbuchen J. Am. Ceram. Soc., 91; [8] 2429-2454 (2008).

[9] H. Y. Hwang, Y. Iwasa, M. Kawasaki, B. Keimer, N. Nagaosa and Y. Tokura Nature Materials 11, 103-113, (2012)

[10] A. Ohtomo and H. Y. Hwang Nature 427, 423-426 (2004).

[11] N. Reyren, S. Thiel, A. D. Caviglia, L. Fitting Kourkoutis, G. Hammer C. Richter, C. W. Schneider, T. Kopp, A.S. Rüetschi, D. Jaccard, M. Gabay, D. A. Muller, J.-M. Triscone, J. Mannhart Science 317, 1196-1199 (2007).

[12] J.-S. Lee, Y.W. Xie, H. K. Sato, C. Bell, Y. Hikita, H. Y. Hwang and C.C. Kao Nature Materials, 12, 703-706 (2013).

[13] Antonello Tebano, Emiliana Fabbri, Daniele Pergolesi, Giuseppe Balestrino, and Enrico Traversa ACS Nano 6,[2] 1278-1283 (2012).

[14] Hiroyuki Yamada, Yoshihiro Ogawa, Yuji Ishii, Hiroshi Sato, Masashi Kawasaki, Hiroshi Akoh, Yoshinori Tokura, Science 305, 646-648 (2004).

[15] P. Yu, W. Luo, D. Yi, J. X. Zhang, M. D. Rossell, C.-H. Yang, L. You, G. Singh-Bhalla, S. Y. Yang, Q. He, Q. M. Ramasse, R. Erni, L. W. Martin, Y. H. Chu, S. T. Pantelide, S. J. Pennycook, and R. Ramesh PNAS 109, [25] 9710-9715 (2012).

[16] A. Gozar, G. Logvenov, L. Fitting Kourkoutis, A. T. Bollinger, L. A. Giannuzzi, D. A. Muller and I. Bozovic Nature 455, 782-785 (2008).

[17] Eric J. Monkman, Carolina Adamo, Julia A. Mundy, Daniel E. Shai, JohnW. Harter, Dawei Shen, Bulat Burganov, David A. Muller, Darrell G. Schlom and Kyle M. Shen Nature Materials 11, 855-859 (2012).

[18] German Hammer and Nicola Spaldin Science 332, 922-923 (2011).

[19] A. V. Boris, Y. Matiks, E. Benckiser, A. Frano, P. Popovich, V. Hinkov, P. Wochner, M. Castro-Colin, E. Detemple, V. K. Malik, C. Bernhard, T. Prokscha, A. Suter, Z. Salman, E. Morenzoni, G. Cristiani, H.-U. Habermeier, B. Keimer Science 332, 937-940 (2011).

[20] Hiromichi Ohta, Sungwng Kim, Yorikomune, Teruyasu Mizoguchi, Kenji Nomura, Shingo Ohta, Takashi Nomura, Yuki Nakanishi, Yuichi Ikuhara, Masahiro Hirano, Hideo Hosono, and Kunihito Koumoto, Nature Materials 6, 129-134 (2007).

[21] J. Narayan Acta Materialia 61, 2703-2724, (2013).

[22] K. J. Choi, M. Biegalski, Y. L. Li, A. Sharan, J. Schubert, R. Uecker, P. Reiche, Y. B. Chen, X. Q. Pan, V. Gopalan, L.Q. Chen, D. G. Schlom, C. B. Eom Science 306, 1005-1009 (2004).

[23] J. H. Haeni, P. Irvin, W. Chang, R. Uecker, P. Reiche, Y. L. Li, S. Choudhury, W. Tian, M. E. Hawley, B. Craigo, A. K. Tagantsev, X. Q. Pan, S. K. Streiffer, L. Q. Chen, S. W. Kirchoefer, J. Levy and D. G. Schlom Nature 430, 758-761 (2004).

[24] J. S. White, M. Bator, Y. Hu, H. Luetkens, J. Stahn, S. Capelli, S. Das, M. Dӧbeli, Th. Lippert, V. K. Malik, J. Martynczuk, A. Wokaun, M. Kenzelmann, Ch. Niedermayer, and C.W. Schneider PRL 111, 037201 (2013).

[25] Lane W. Martin, Darrell G. Schlom Current Opinion in Solid State and Materials Science 16 (2012) 199-215

[26] Nina V. Burbure, P.A. Salvador, and Gregory S. Rohrer J. Am. Ceram. Soc., 93 2530 (2010).

[27] Y. Zhang, A. M. Schultz, L. Li, H. Chien, P.A. Salvador, and G.S. Rohrer, Acta Mater., 60, 6486 (2012).

[28] S. Havelia, S. Wang, K. R. Balasubramaniam, A. M. Schultz, G. S. Rohrer, and P. A. Salvador, CrystEngComm, 15, 5434 (2013).

[29] A. M. Schultz, Y. Zhu, S. A. Bojarski, G. S. Rohrer, and P. A. Salvador, Thin Solid Films, 548, 220-224 (2013).

[30] N. V. Burbure, P. A. Salvador, and G. S. Rohrer, Chem. Mater., 22, 5831 (2010).

[31] Zuhair A. Munirw and Dat V. Quach,Manshi Ohyanagi J. Am. Ceram. Soc., 94 [1] 1-19 (2011).

[32] Rishi Raj, Marco Cologna, and John S. C. Francis J. Am. Ceram. Soc., 94 [7] 1941-1965 (2011).

[33] M. N. Rahaman, Ceramic Processing and Sintering (Taylor and Francis, 2003).

[34] David J. Prior, Alan P. Boyle, Frank Brenker, Michael C. Cheadle, Austing Day, Gloria Lopex, Luca Peruzzo, Graham J. Potts, Steve Reddy, Richard Spiess, Nick E. Timms, Pat Trimby, John Wheeler, and Lena Zetterstrӧm American Mineralogist, 84, 1741-1759 (1999).

[35] Pulsed Laser Deposition of Thin Films, edited by Douglas B. Chrisey and Graham K. Hubler, John Wiley and Sons, ISBN 0-471-59218-8, (1994).

[36] Goldstein, J.; et al.; Scanning Electron Microscope and X-ray Microanalysis, 2nd printing, (2007).

[37] Electron Backscatter Diffraction in Materials Science, 2nd ed., edited by A. J. Schwartz, M. Kumar, B. L. Adams, and D. P. Field Springer, New York, 403, (2009).

[38] A. Winkelmann and G. Nolze, Ultramicrospy. 110, 190-194, (2010).

[39] Angus J. Wilkinson and T. Ben. Britton Materials Today 15,9 366-376 (2012).

[40] K.Z. Baba-Kishi, Scanning 20, 117 (1998).

[41] OIM manual version 6.2 http://www.edax.com/Products/EBSD/OIM-Data-Analysis-Microstructure-Analysis.aspx

[42] S. Matthies and G. Vinel and K. Helming, Helming (Eds). Akademie-Verlag. 1, 449 (1987).

[43] S. Wright and M. Nowell Microsc. Microanal., 12, 72-84 (2006).

[44] Noriyuki Kuwano, Kayo Horibuchi, Koji Kagawa, Shigefumi Nishimoto, Manabu Sueyoshib Journal of Crystal Growth 237-239, 1047-1054 (2002).

[45] J.F. Luo, Y. Ji, T.X. Zhong, Y.Q. Zhang, J.Z. Wang, J.P. Liu, N.H. Niu, J. Han, X. Guo, G.D. Shen Microelectronics Reliability 46, 178-182 (2006).

[46] C. Trager Cowan and F. Sweeney, P. W. Trimby, A. P. Day, A. Gholini, and N.H. Schmidt,P. J. Parbrook, A. J. Wilkinson, I. M. Watson Phys. Rev. B 75, 085301 (2007).

[47] K. De Keyser, C. Detavernier, and R. L. Van Meirhaeghe Appl. Phys. Lett. 90, 121920 (2007).

[48] X. Zhao, L. Phillips, C. E. Reece, Kang Seo, M. Krishnan, and E. Valderrama J. Appl. Phys. 110, 033523 (2011).

[49] N.Brodusch, H.Demers and R. Gauvin Journal of Microscopy, 250, 1-14 (2013).

[50] Elements of Modern X-Ray Physics, J. Als-Nielsen, D. McMorrow, John Wiley and Sons, (2000).

[51] Underneath the Bragg Peaks, T. Egami, S. Billinge, Pergamon, (2003).

[52] David A. Muller Nature Materials 8, 263-270 (2009).

[53] Franz J. Giessibl, Rev. of Modern. Phys. 75,(3) 949, (2003).

[54] Sergei V. Kalinin, Andrei Rar, and Stephen Jesse Ultrasonics, Ferroelectrics and Frequency Control, IEEE Transactions ISSN :0885-3010 53,[12] 2226 - 2252 (2006).

[55] A.C. Masset, C. Michel, A. Maignan, M. Hervieu, O. Toulemonde, F.Studer, B. Raveau, and J. Hejtmanek, Phys. Rev. B 62, 166 (2000).

[56] M.Tritt and M.A. Subramanian, MRS Bull. 31 188 (2006) and references therein.

[57] M. S. Dresselhaus Phy Rev B 68, 075304, (2003).

[58] Joseph P. Heremans, Vladimir Jovovic, Eric S. Toberer, Ali Saramat, Ken Kurosaki, Anek Charoenphakdee, Shinsuke Yamanaka, G. Jeffrey Snyder, Science 321, 554, (2008).

[59] Kanishka Biswas, Jiaqing He, Ivan D. Blum, Chun-Iwu, Timothy P. Hogan, David N. Seidman, Vinayak P. Dravid and Mercouri G. Kanatzidis, Nature. 489, 414-418, (2012).

[60] A.I. Hochbaum, R. Chen, R. Diaz Delgado, W. Liang, E.C. Garnett, M. Najarian, A. Majumdar and P. Yang, Nature **451**, 163 (2007), J. Heremans and C.M. Thrush, Phys. Rev. 59 12583 (1999).

[61] H. Ohta, S. Kim, Y. Mune, T. Mizoguchi, K. Nomura, S. Ohta, T. Nomura, Y. Nakanishi, Y. Ikuhara, M. Hirano, H. Hosono and K. Koumoto, Nature Mater. 6 129 (2007).

[62] P.-H. Xiang, Y. Kinemuchi, H. Kaga and K. Watari, J. Alloys. Compds, 454, 364, (2008).

[63] A.J. Zhou, T.J. Zhu, H.L. Ni, Q. Zhang, X.B. Zhao, J. Alloys. Compds, 455, 255, (2008).

[64] T. Yin, D. Liu Y. ou, F. Ma, S. Xie, J.-F. Li and J. Li, J. Phys. Chem. 114 10061 (2010).

[65] A. Sakai, T. Kanno, S. Yotsuhashi, A. Odagawa and H. Adachi, Jpn. J. Appl. Phys. 44, L966 (2005).

[66] Hank W. Eng, W. Prellier, S. Hélbert, D. Grebille, L. Méchin, and B. Mercey, J. Appl. Phys. 97, 013706 (2005).

[67] Min-Gyu Kang, Kwang-Hwan Cho, Seung-Min Oh, Jin-Sang Kim, Chong-Yun Kang, Sahn Nahm, and Seok-Jin Yoon, Appl. Phys. Lett. 98, 142102 (2011).

[68] S. Wang, M. Chen, L. He, J. Zheng, W. Yu and G. Fu, J. Phys. D 42 045410 (2009).

[69] S. Matthies, G. Vinel, and K. Helming, Standard Distributions in Texture Analysis (Akademie-Verlag, 1987), Vol. 1, p. 449.14

[70] M. N. Rahaman, Ceramic Processing and Sintering (Taylor and Francis, 2003)

[71] T. H. Courtney, Mechanical Behaviour of Materials (McGraw-Hill, New York, 1990).

[72] Y. Yoshizawa, K. Hirao, and S. Kanzaki, J. Am. Ceram. Soc. 87, 2147 (2004).

[73] F. Gao, J. Appl. Phys. 112, 023506 (2012).

[74] D.J. Prior, A.P. Boyle, F. Brenker, M.C. Cheadle, A. Day, G. Lopez, L. Peruzzo, G.J. Potts, S. Reddy, R. Spiess, N.E. Timms, P. Trimby, J. Wheeler, and L. Zetterström, Amer. Miner. 84 1741 (1999).

[75] K.Z. Baba-Kishi, J. Mater. Science 37 1715 (2002).

[76] S. T. Wardle, L. S. Lin, A. Cetel, and B. L. Adams, in Proc. 52nd Annual Meeting of the Microscopy Society of America, edited by G. W. Bailey and A. J. Garratt-Reed (San Francisco Press, San Francisco, 1994), p. 680.

[77] T. H. Courtney, Mechanical Behaviour of Materials (McGraw-Hill, New York, 1990).

[78] E. Guilmeau, C. Henrist, T. S. Suzuki, Y. Sakka, D. Chateigner, D.Grossin, and B. Ouladdiaf, Mater. Sci. Forum 495-497, 1395 (2005).

[79] H. P. Pinto, R. M. Nieminen, and S. D. Elliott, Phys. Rev. B 70, 125402 (2004).

[80] A. Marmier, A. Lozovoi, and M. W. Finnis, J. Eur. Ceram. Soc. 23, 2729 (2003).

[81] S. Blonski and S. H. Garofalini, Surf. Sci. 295, 263 (1993).

[82] Y. Zhang, A. M. Schultz, L. Li, H. Chien, P. A. Salvador, and G. Rohrer, Acta Mater. 60, 6486 (2012).

[83] L.X. Fan, D.L. Guo, F. Ren, X.H. Xiao, G.X. Cai, Q. Fu and C.Z. Jiang, J. Phys. D: Appl. Phys. 40 7302 (2007).

[84] A direction in the four-index notation is represented by (uvtw), and becomes, in the three-index notation, (u'v'w') where u=(2u'-v')/3, v=(2v'-u')/3, t=-(u+v) and w=w' See, for example: C. Giacavazzo, Fundamentals of Crystallography Oxford University Press, New York, (2002).

[85] T. Tani, H. Itahara, H. Kadoura, and R. Asahi, Int. J. Appl. Ceram. Technol. 4, 318 (2007).

[86] T. Sun, H.H. Gng, Q.Y. Yan and J. Ma, J. Appl. Phys. Lett. 108 083709 (2010).

[87] Q. Qiao, A. Gulec, T. Paulauskas, S. Kolensnik, D. Dabrowski, M. Ozdemir, C. Boyraz, D. Mazumdar, A. Gupta and R.F. Klie, J. Phys.:Condens. Matter 23 305005 (2011).

[88] A. Gonsalez-Gonsalez, G.M. Alonzo-Medina, A..I. Oliva, C. Polop, J.L. Saceon and E. Vasco, Phys. Rev. B 84 155450 (2011).

[89] A. Gonsalez-Gonsalez, C. Polop and E. Vasco, Phys. Rev. Lett. 110 056101 (2013).

[90] T. Sun, H.H. Hng, Q. Yan and J.N. Ma, J. Elec. Mater. 39, 1611 (2010).

[91] Y.F. Hu, W.D. Si, E. Sutter, and Q. Li, Appl. Phys. Lett. 86, 082103 (2005).

[92] Y.F. Hu, E. Sutter, W.D. Si, and Q. Li, Appl. Phys. Lett. 87, 171912 (2005).

[93] M. Karppinen, H. Fjellvég, T. Konno, Y. Morita, T. Motohashi, H. Yamauchi, Chem. Mater. 16 2790 (2004), Y. Morita, J. Poulsen, K. Sakai, T. Motohashi, T. Fujii, I. Terasaki, H. Yamauchi, M. Karppinen, J. Solid State Chem. 177 3149 (2004).

[94] Y. Huang, B. Zhao, J. Fang, R. Ang, and Y. Sun, J. Appl. Phys. 110, 123713 (2011).

[95] R.F. Klie, Q. Qiao, T. Paulauskas, A. Gulec, A. Rebola, S. *Ögüt*, M.P. Prange, J.C. Idrobo, S.T. Pantelides, S. Kolesnik, B. Dabrowski, M. Ozdemir, C. Boyraz, D. Mazumdar and A. Gupta, Phys. Rev. Lett. 108 19661 (2012).

[96] M.Ye. Zhuravlev, R. F. Sabirianov, S. S. Jaswal and E.Y. Tsymbal Phys. Rev. Lett. 94, 246802 (2005).

[97] R. Ramesh and Nicola.A. Spaldin Nature Materials 6, (2007).

[98] Kornev, I. A. and Bellaiche, L. Phys. Rev. B 79, 100105(R) (2009).

[99] Jinbo Caoa, Junqiao Wua Materials Science and Engineering R 71, 35-52, (2011).

[100] J.H. Nam, H.S. Kim, A. J. Hatt, N. A. Spaldin, and H.M. Christen Phys. Rev. B 83, 144107 (2011).

[101] P. Ravindran, R. Vidya, A. Kjekshus, and H. FjellvÃěg Phys. Rev. B 74, 224412 (2006).

[102] R. J. Zeches, M. D. Rossell, J. X. Zhang, A. J. Hatt, Q. He, C.H. Yang, A. Kumar, C. H. Wang, A. Melville, C. Adamo, G. Sheng, Y.H. Chu, J. F. Ihlefeld, R. Erni, C. Ederer, V. Gopalan, L. Q. Chen, D. G. Schlom, N. A. Spaldin, L. W. Martin and R. Ramesh Science 326, 977 (2009).

[103] Q. He, Y. H. Chu, J. T. Heron, S. Y. Yang, W. I. Liang, C.Y. Kuo, H. J. Lin, P. Yu, C. W. Liang, R. J. Zeches, W. C. Kuo, J. Y. Juang, C. T. Chen, E. Arenholz, A. Scholl and R. Ramesh Nature communications 2, 225 (2011).

[104] H.W. Jang, S. H. Baek, D. Ortiz, C. M. Folkman, R. R. Das, Y. H. Chu, P. Shafer, J. X. Zhang, S. Choudhury,V. Vaithyanathan, Y. B. Chen, D. A. Felker, M. D. Biegalski, M. S. Rzchowski, X. Q. Pan, D. G. Schlom, L. Q. Chen, R. Ramesh, and C. B. Eom Phys. Rev. Lett. 101, 107602 (2008).

[105] J. X. Zhang, D. G. Schlom, L. Q. Chen, and C. B. Eom Appl. Rev. Lett. 95, 122904 (2009).

[106] C. W. Huang, Z. H. Chen, Junling Wang, T. Sritharan, and Lang Chen J. Appl. Phys. 110, 014110 (2011).

[107] S. H. Baek, H. W. Jang, C. M. Folkman, Y. L. Li, B. Winchester, J. X. Zhang, Q. He, Y. H. Chu, C. T. Nelson, M. S. Rzchowski, X. Q. Pan, R. Ramesh, L. Q. Chen and C. B. Eom Nature Materials 9, (2010).

[108] Y.P. Shi, A.K. Soh, and G.J. Weng J. Appl. Phys. 109, 024102 (2011).

[109] J. Wang, J.B. Neaton, H. Zheng, V. Nagarajan, S.B. Ogale, B. Liu, D. Viehland, V. Vaithyanathan, D.G. Schlom, U.V. Waghmare, N.A. Spaldin, K.M. Rabe, M. Wuttig, and R. Ramesh, Science 299, 1719 (2003).

[110] Jiefang Li, Junling Wang, M. Wuttig, R. Ramesh, Naigang Wang, B. Ruette, A.P. Pyatakov, A.K. Zvezdin, and D. Viehland, Appl. Phys. lett. 84, 5261 (2004).

[111] Jiagang Wu and John Wang, J. Appl. Phys. 106, 104111 (2009).

[112] Manoj K. Singh, Ram S. Katiyar, W. Prellier and J.F. Scott, J. Phys. Cond. Matter 21, 04220 (2009).

[113] Z. Trajanovic, C. Kwon, M.C. Robson, K.C Kim, M. Rajeswari, R. Ramesh, T. Venkatesan, S.E. Lofland, S.M. Bhagat and D. Fork, Appl. Phys. Lett. 69, 1005 (1996).

[114] Yu, Y.-D., Xie, S.-H., Boysen, H., Wuli Xuebao; Acta Phys. Sinica, 42, 605, (1993).

[115] Hayward, S.A. Morrison, F.D. Redfern, S.A.T. Salje, E.K.H. Scott, J.F. Knight, K.S.Tarantino, S.Glazer, A.M. Shuvaeva, V. Daniel, P. Zhang, M.Carpenter, M.A., Phys. Rev. B 72, 054110 (2005).

[116] M. Aindow and R.C. Pond, Phil. Mag. A 63, 667 (1991).

[117] L.X. Fan, D.L. Guo, F. Ren, X.H. Xiao, G.X. Cai, Q. Fu and C.Z. Jiang, J. Phys. D: Appl. Phys. 40, 7302 (2007).

[118] Y.-H. Chu, M.P. Cruz, C.-H. Yang, L.W. Martin, P.-L. Yang, J.-X. Zhang, K. Lee, P. Yu, L.-Q. Chen and R. Ramesh, Adv. Mater. 19, 2662 (2007).

[119] P. Yu, W. Luo, D. Yi, J.X. Zhang, M.D. Rossell, C.-H. Yang, L. You, G. Singh-Bhalla, S.Y. Yang, Q. He, Q.M. Ramasse, R. Erni, L.W. Martin, Y.H. Chu, S.T.

Pantelides, S.J. Pennycook, and R. Ramesh, Proc. Nat. Acad. Science 109, 9710 (2012).

[120] J.X. Zhang, Q. He, M. Trassin, W. Luo, D. Yi, M. D. Rossell, P. Yu, L. You, C.H. Wang, C.Y. Kuo, J.T. Heron, Z. Hu, R.J. Zeches, H.J. Lin, A. Tanaka, C.T. Chen, L.H. Tjeng, Y.-H. Chu, and R. Ramesh, Phys. Rev. Lett. 107, 147602 (2011).

[121] H. Zheng, F. Straub, Q. Zhan, P.-L. Yang, W.-K. Hsieh, F. Zavaliche, Y.-H. Chu, U. Dahmen and R. Ramesh, Adv. Mat. 18, 2747 (2006), N. Balke, M. Gajek, A.K. Tagantsev, L.W. Martin, Y.-H. Chu, R. Ramesh and S.V. Kalinin, Adv. Func Mat. 20, 3466 (2010), Nature Mater. 8, 229 (2009).

[122] S.H. Baek, H.W. Jang, C.M. Folkman, Y.L. Li, B. Winchester, J.X. Zhang, Q. He, Y.H. Chu, C.T. Nelson, M.S. Rzchowski, X.Q. Pan, R. Ramesh, L.Q. Chen and C.B. Eom, Nature Materials 9, 309 (2010), M.P. Cruz, Y. H. Chu, J.X. Zhang, P.L. Yang, F. Zavaliche, Q. He, P. Shafer, L.Q. Chen, and R. Ramesh, Phys. Rev. Lett. 99, 217601 (2007).

[123] M. A. Subramanian, G. Aravamundan and G. V. Subba Rao, Prog. Solid State Chem., 15, 55, (1983).

[124] P. Dasgupta, Y. M. Jana, A. Nag Chattopadhyay, R. Higashinaka, Y. Maeno and D. Ghosh, J. Phys. Chem. Solids, 68, 347 (2007).

[125] A. V. Shlyakhtina, A. V. Knotko, M. V. Boguslavskii, S. Yu. Stefanovich, D. V. Peryshkov, I. V. Kolbanev and L. G. Shcherbakova, Solid State Ionics, 176, 2297, (2005).

[126] Zhenmian Shao, Sébastien Saitzek, Pascal Roussel and Rachel Desfeux J. Mater. Chem., 22, 24894, (2012).

[127] S. Havelia, S.Wang, K.R. Balasubramaniam and P.A.Salvador, J. Solid State Chem. 182, 1603 (2009).

[128] Mark T. Weller, Robert W. Hughes, Joanna Rooke, Christopher S. Knee and Jon Reading Dalton Trans. 3032-3041, (2004).

[129] Gasperin, M. Acta Crystallographica B (24,1968-38,1982)(1975), 31, 2129-2130 Golden Book of Phase Transitions, Wroclaw 1, 1-123 (2002).

[130] Garbout, A.;Ben Taazayet-Belgacem, I.;Ferid, M. J. of Alloys. and Compods. 573, 43-52 (2013).

[131] K. A. Mäder, H. von Känel, and A. Baldereschi, Phys. Rev. B 48, 4364 (1993).

[132] Chunrui Ma1, Ming Liu, Chonglin Chen, Yuan Lin, Yanrong Li, J. S. Horwitz, Jiechao Jiang, E. I. Meletis and Qingyu Zhang Scientific Reports“ 3, 3092, (2014).

[133] Philippe Ghosez and Javier Junquera Handbook of Theoretical and Computational Nanotechnology Chapter 134 : First-Principles Modeling of Ferroelectric Oxides Nanostructures American Scientific Publisher(Stevenson Ranch, CA, USA) (2006).

[134] M.J. Hÿtch Scanning Microscopy 11, 53-66, (1997).

[135] James M. Rondinelli and Nicola A. Spaldin Adv. Mater. 23, 3363-3381 (2011).

[136] O. I. Lebedev, G. Van Tendeloo, S. Amelinck, B. Leibold and H.U. Habermeier Phys. Rev. B 58,12 8065-8074 (1998).

[137] Frank F C and van der Merwe J H Proc. R. Soc. A 198, 205 (1949).

[138] G. Van. Tendeloo, O. I. Lebedev, M. Hervieu and B. Raveau Rep. Prog. Phys. 67 1315-1365 (2004).

# Publications

1. D. Pravarthana, D. Chateigner, M. Lacotte, S. Marinel, P.A. Dubos, I. Hervas, E. Hug, L. Lutterotti, P. Salvador and W. Prellier, "Growth and texture of Spark Plasma Sintered $Al_2O_3$ ceramics: a combined analysis of X-rays and Electron Back Scatter Diffraction", Joural of Applied Physics 113, 153510 (2013).

2. D.Pravarthana, O.I.Lebedev, S.Hebert, D. Chateigner, P.Salvador and W.Prellier, "High-throughput synthesis of thermoelectric $Ca_3Co_4O_9$ films", Applied Physics Letters 103, 143123 (2013).

3. Shekhar D. Bhame, Dhanapal Pravarthana, Wilfrid Prellier, and Jacques G. Noudem, "Enhanced thermoelectric performance in spark plasma textured bulk n-type $Bi_2Te_{2.7}Se0.3$ and p-type $Bi_{0.5}Sb_{1.5}Te_3$", Applied Physics Letters 102, 211901 (2013).

4. D.Pravarthana, M.Trassin, J.H Chu, M.Lacotte, A.David, R. Ramesh, P.A Salvador, W.Prellier, "$BiFeO_3/La_{0.7}Sr_{0.3}MnO_3$ heterostructures deposited on spark plasma sintered $LaAlO_3$ substrates", Applied Physics Letters 104, 082914 (2014).

5. M.Lacotte, A.David, D.Pravarthana, G.Rohrer, P.Salvador, M.Velazquez, Matias, C.Grygiel, W.Prellier, " Growth of $Ca_2MnO_4$ Ruddlesden-Popper structured thin films using Combinatorial Substrate Epitaxy",(Submitted to Acta materialia(2014))

# Contributions at conferences

1. D. Pravarthana, B.Vertruyen, M.Lacotte, D. Chateigner, and W.Prellier "EBSD mapping of oxide substrates prepared by Spark Plasma Sintering.", Programme de la journée de l'école Doctorale Thématique CHIM 16 novembre 2012 Université Catholique de Louvain, UCL Batiment Sciences(SC11)- AuditoireSCES01 Salle d'étude de la faculté des Sciences (Poster)

2. "Thermoelectric Materials from bulk to thin films", IDS-FunMat Training School Anglet, March 25-31, 2012 . (Oral)

3. D. Pravarthana and W.Prellier "Probing the heteroepitaxy of nanostructured $BiFeO_3$ on spark plasma sintered $LaAlO_3$ substrates", IDS-Funmat Training School Annecy, March 17-21, 2013 . (Poster)

4. D. Pravarthana and W.Prellier "Probing the heteroepitaxy of nanostructured $BiFeO_3$ on spark plasma sintered $LaAlO_3$ substrates", IDS-Funmat Training School Annecy, March 17-21, 2013. (Oral)

5. "Oxide films for renewable energy applications : from single crystals to polycrystalline substrates", International Congress on Materials and Renewable Energy (MRE 2013) 1-3 July 2013 : Athens, Greece. (Oral)

## Synthèse combinatoire de films minces d'oxydes fonctionnels

Les films minces d'oxydes présentent un intérêt car il est possible d'obtenir de nouvelles propriétés pour des applications comme l'électronique ou l'énergie/. Cependant, les recherches sont limitées par la composition et le faible indice des substrats monocristaux commercialisés. En conséquence, il faut trouver de nouvelles méthodes. Dans ce travail, nous avons développés une méthode combinatoire, appelé l'épitaxie combinatoire, où un film est déposé sur un substrat polycristallin. Afin de confirmer la faisabilité, nous avons d'abord fabriqué des films de $Ca_3Co_4O_9$ sur des céramiques de $Al_2O_3$. Les films sont épiatxiés et présentent un coefficient Seebeck de 170 $\mu$V/K à 300 K. Ensuite, des hétéorstructures de $BiFeO_3/La_{0.7}Sr_{0.3}MnO_3$ ont été préparées sur des substrats de $LaAlO_3$ obtenus par frittage flash. Les propriétés locales ont été vérifiées par PFM. Enfin, nous avons étudiés la croissance de phase métastable monoclinique de $Dy_2Ti_2O_7$ sur des polycristaux de $La_2Ti_2O_7$. Nous concluons que la CSE ouvre la voie à de nouvelles électroniques.

## High-Throughput Synthesis of Functional Oxide Films

Epitaxy of metal oxides is of great interest since it provides a way to obtain desired novel properties for the applications such as electronics and energy. However, earlier epitaxy research's have been restricted because of the limited range of compositions and low-index of commercially available single crystal substrates. Consequently, novel epitaxy synthesis methods need to be developed in order to go beyond the present demands of of single crystal substrates in terms of phase, composition, size, orientation and symmetry. In this research work, we have developed a high-throughput synthesis process, called combinatorial substrate epitaxy (CSE), where an oxide film is grown epitaxially on a polycrystalline substrate. As a proof-of-concept, we firstly fabricated $Ca_3Co_4O_9$ films on $Al_2O_3$ ceramics. Films have a good local epitaxial registry, and the Seebeck coefficient is about 170 $\mu$V/K at 300 K. High quality $BiFeO_3/La_{0.7}Sr_{0.3}MnO_3$ thin film heterostructures were secondly deposited on dense $LaAlO_3$ ceramics prepared by spark plasma sintering. Piezoforce microscopy was used to confirm the local ferroelectric properties. Thirdly, we investigate the growth of of metastable monoclinic $Dy_2Ti_2O_7$ epitaxial films on polycrystalline $La_2Ti_2O_7$ substrates. We conclude that CSE approach opens the way towards unexpected electronic properties in oxide films.

**Mots clés** : Couches minces, Oxydes des métaux de transition, Ceramics, Electron Back Scattering Diffraction

## Chimie des matériaux

Laboratoire CRISMAT, UMR6508, ENSICAEN

6, Boulevard MarÃľchal Juin, 14050 CAEN Cedex 4